Chemistry in aerosol particles

Ultrahigh-pressure liquid chromatography – ultrahigh-resolution mass spectrometry studies on particle size-dependent chemical reactions in aerosol particles

Dissertation

zur Erlangung des akademischen Grades
Doktor der Naturwissenschaften (Dr. rer. nat.)
im Promotionsfach Chemie

am Fachbereich Chemie, Pharmazie, Geographie und Geowissenschaften
der Johannes Gutenberg-Universität Mainz

vorgelegt von
Maximilian Böckmann
geboren in Mainz

JOHANNES GUTENBERG UNIVERSITÄT MAINZ

JG|U

November 2021

Dekanin:
1. Gutachter:
2. Gutachter:

Tag der mündlichen Prüfung: 10. Dezember 2021

D77 Dissertation der Johannes Gutenberg-Universität Mainz

I hereby declare that I wrote the dissertation submitted without any unauthorised external assistance and used only sources acknowledged in the work. All textual passages which are appropriated verbatim or paraphrased from published and unpublished texts as well as all information obtained from oral sources are duly indicated and listed in accordance with bibliographical rules. In carrying out this research, I complied with the rules of standard scientific practice as formulated in the statutes of Johannes Gutenberg University Mainz to insure standard scientific practice.

Mainz, 5th November 2021

Reality is one of the possibilities I cannot afford to ignore.

Leonard Cohen

Danksagung

Zusammenfassung

Aerosole haben einen großen Einfluss auf die menschliche Gesundheit. Insbesondere sehr kleine Partikel können bis tief in die Lunge eindringen und verursachen allergische Reaktionen sowie Atemwegs- und Herz-Kreislauf-Erkrankungen. Darüber hinaus spielen Aerosole eine große Rolle für das Klima der Erde. Abgesehen von einem wärmenden Effekt durch Kohlenstoffaerosole (*black carbon*) haben Aerosole sowohl durch die direkte Interaktion mit elektromagnetischer Strahlung als auch durch die Funktion als Wolkenkondensationskeime einen kühlenden Effekt.

Ein großer Teil der atmosphärischen Aerosole besteht aus organischen Verbindungen. Von diesen organischen Aerosolen ist wiederum ein großer Teil sekundärer Natur, also durch die Transformation flüchtiger organischer Verbindungen zu schwer- oder nichtflüchtigen Verbindungen entstanden. Durch die Kondensation dieser neu gebildeten Verbindungen kommt es zum Wachstum bereits bestehender Partikel, oder – in Abwesenheit von Kondensationskeimen – auch zur Neubildung von Aerosolpartikeln. Damit Partikel als Wolkenkondensationskeime dienen und dadurch einen Einfluss auf das Klima nehmen können, müssen sie eine Größe von mindestens 30 nm bis 100 nm erreichen. Das Wachstum steht dabei in ständiger Konkurrenz zur Koagulation mit größeren Partikeln. Eine Bevorzugung der Bildung schwerflüchtiger Verbindungen in kleinen Partikeln oder an deren Oberfläche im Vergleich zu größeren Partikeln würde zu größeren Wachstumsraten und dadurch einer erhöhten Wahrscheinlichkeit für das Erreichen der notwendigen Größe führen.

Das Ziel dieser Arbeit war es, den Einfluss der Partikelgröße auf chemische Reaktionen in Aerosolpartikeln zu untersuchen. Dazu wurden Aerosole aus den Lösungen der Reagenzien erzeugt, nach einer Reaktionszeit entsprechend ihrer Größe klassifiziert und auf Filtern gesammelt. Im Anschluss wurden die Filterproben extrahiert und mittels Ultrahochleistungs-Flüssigchromatographie in Kopplung mit ultrahochaufgelöster Massenspektrometrie untersucht.

Der erste Teil dieser Arbeit beschäftigt sich mit dem Versuchsaufbau und beschreibt die Optimierung der Messmethode. Im zweiten Teil der vorliegenden Arbeit geht es um

die Untersuchung der Größenabhängigkeit der heterogenen Oxidation von 1,3-Diphenylisobenzofuran. Die Oxidation wurde unter verschiedenen experimentellen Bedingungen untersucht, um Rückschlüsse über die Eigenschaften der Aerosolpartikel zu ziehen, die ausschlaggebend für die Bevorzugung der Oxidation in kleineren Partikeln sind.

Der dritte Teil dieser Arbeit beschäftigt sich mit Untersuchungen zur Diels-Alder-Reaktion von Maleinsäure und 1,3-Diphenylisobenzofuran in Aerosolpartikeln. Die Diels-Alder-Reaktion wurde als Modellreaktion für bindungsknüpfende Reaktionen herangezogen, die bereits in Aerosolpartikeln beobachtet wurden. Auch hier wurden die experimentellen Bedingungen variiert, um Faktoren auszumachen, welche in Abhängigkeit von der Partikelgröße Einfluss auf die Bildung des Diels-Alder-Produkts nehmen. Im Gegensatz zur Oxidationsreaktion deuten hier die Ergebnisse darauf hin, dass die Reaktion in größeren Partikeln begünstigt wird.

Schließlich wurde im vierten Teil ein numerisches Modell angewandt, welches den Umsatz der Diels-Alder-Reaktion in Abhängigkeit von der Partikelgröße berechnete. Mithilfe des Modells wurden die Einflüsse einiger Eigenschaften des Modellsystems untersucht. Darüber hinaus wurde versucht, die experimentellen Ergebnisse durch das Modell abzubilden.

Abstract

Aerosols have an important impact on human health and welfare. Especially ultrafine particles are able to migrate deeply into the lungs and are known to cause allergic reactions as well as respiratory and cardiovascular diseases. Furthermore, aerosols are of high importance for the Earth's climate. Besides a warming effect of black carbon, aerosols have a net cooling effect. The interaction of aerosols with electromagnetic radiation as well as their ability to serve as cloud condensation nuclei leads to a decrease of irradiation on the Earth's surface and therefore to the cooling effect.

A large part of atmospheric aerosols consists of organic compounds. Out of these organic aerosols, a large fraction is formed in the atmosphere by transformation of volatile organic compounds into low-volatile or essentially non-volatile organic compounds. These newly formed compounds condense onto pre-existing particles or – in absence of such condensation nuclei – form new particles through nucleation. For aerosol particles to serve as cloud condensation nuclei and therefore to exert an effect on climate, particles must grow to sizes of at least 30 nm to 100 nm in diameter. The growth of particles is always in competition with coagulation with larger particles. A preference for the formation of low-volatile organic compounds in smaller aerosol particles or at their surface would lead to increased growth rates of smaller particles and subsequently to higher chances of reaching climatic relevant sizes.

The objective of this study was the examination of the influence of particle size on chemical reactions in aerosol particles. Aerosols were nebulised from reagent solutions, after a certain reaction time aerosols were size-classified and collected on filters. Subsequently, the filter samples were extracted and analysed with ultrahigh-pressure liquid chromatography coupled to an ultrahigh-resolution mass spectrometer.

The first part of this study deals with the experimental setup and describes the optimisation of the LC method and mass spectrometric parameters. In the second part of this study, the particle size-dependence of the heterogeneous oxidation of 1,3-diphenylisobenzofuran was investigated. Experiments were conducted under different experimental

conditions to narrow down properties of aerosol particles responsible for the preference of the oxidation reaction in smaller particles.

The third part of this study deals with examinations of the Diels-Alder reaction of maleic acid and 1,3-diphenylisobenzofuran in aerosol particles. The Diels-Alder reaction was used as a model system for bond-forming reactions in aerosol particles. Again, experimental conditions were varied to evaluate which aspects have a particle size-dependent influence on the formation of the Diels-Alder product. In contrast to the oxidation reaction, results suggest a preference of the reaction in larger particles.

In the fourth part of this study, a numerical model was employed which calculates the conversion ratio of the Diels-Alder reaction dependent on the particle size. By means of the model, the influence of several properties of aerosol particles on the model system were examined. Furthermore, experimental results were compared to calculations and changes were made to the model in an attempt to represent experimental results with numerical calculations.

Contents

1 Introduction

According to the Intergovernmental Panel on Climate Change (2014), the three decades from 1983 to 2012 have likely been the warmest in the northern hemisphere in the last 1400 years. The major part of the additional energy is stored in the oceans, which upper 75 m have warmed by around 0.11 °C. Additionally, carbon dioxide (CO_2) uptake has led to an acidification of the oceans with an average decrease in pH of 0.1 at the ocean's surface. Greenland's and Antarctica's ice sheets have lost mass in the period from 1992 to 2011 and glaciers have shrunk almost worldwide (Intergovernmental Panel on Climate Change 2014).

In the face of rising temperatures and sea levels, climate change has received increasing attention from both the scientific community and the public. Whilst greenhouse gas emissions (carbon dioxide, methane (CH_4) and nitrous oxide (N_2O)) have been identified as the main driver of climate change, it is of high importance to understand the climate system as a whole (Intergovernmental Panel on Climate Change 2014).

The physical drivers of climate change are emissions that alter the radiative budget of the Earth. To quantify the influence of these drivers, the radiative forcing (RF) is calculated from observations, properties of greenhouse gases and aerosols as well as numerical model calculations (Intergovernmental Panel on Climate Change 2014; Seinfeld and Pandis 2006; Pöschl 2005). Positive values for RF indicate an increase in temperature, whereas emissions with a negative RF have a cooling effect on the atmosphere (Pöschl 2005; Intergovernmental Panel on Climate Change 2014).

An important part of Earth's climate system are aerosols. Though the number of scientists working on topics related to aerosol particles has increased over the last two to three decades (Kolb and Worsnop 2012), the knowledge about the influence of aerosol particles on Earth's climate and on climate change remains limited: The largest uncertainty to the total radiative forcing estimates originates from aerosols (Intergovernmental Panel on Climate Change 2014).

Atmospheric aerosols are known to influence the Earth's climate both by reflecting and absorbing incoming sunlight and through their ability to act as cloud condensation

nuclei (CCN) (Kulmala et al. 2004; Seinfeld and Pandis 2006; Intergovernmental Panel on Climate Change 2013, 2014; Hoffmann, Zetzsch and Rossi 2007). Whilst black carbon emissions due to the absorption of sunlight lead to a slightly positive radiative forcing of $0.04\,\mathrm{W\,m^{-2}}$, the overall radiative forcing caused by aerosols is considered to be negative ($-0.9\,\mathrm{W\,m^{-2}}$), therefore cooling the atmosphere and at least partially counteracting increased greenhouse gas emissions (Intergovernmental Panel on Climate Change 2013, 2014). Figure 1.1 sums up different emissions and their corresponding radiative forcings.

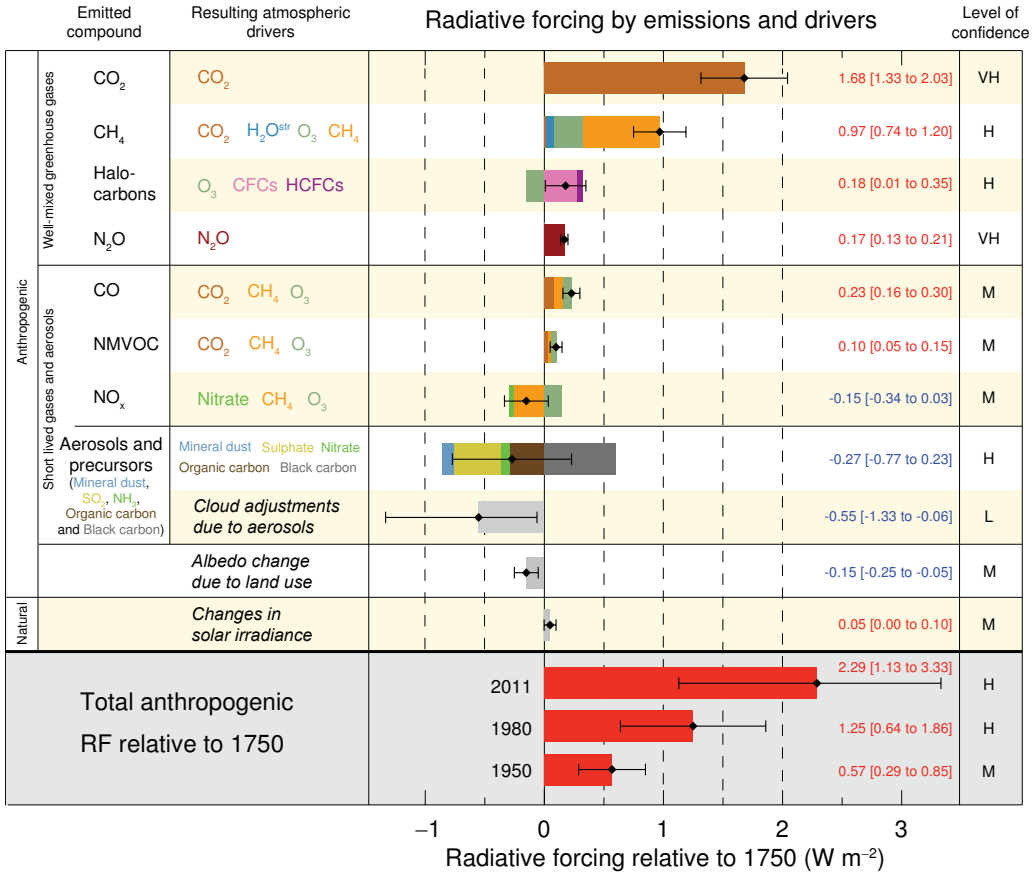

Figure 1.1: Estimated radiative forcing in 2011 relative to 1750. Black diamonds indicate the best estimates for net radiative forcings with the corresponding uncertainties. Figure adapted from Intergovernmental Panel on Climate Change (2013).

Especially aerosol-cloud interactions and the corresponding radiative forcing remain poorly understood, mostly due to insufficient knowledge and limited representation of processes in atmospheric models (Pöschl 2005; Intergovernmental Panel on Climate Change 2014). There is general agreement though that the number of CCNs influences the number and size of cloud droplets and therefore controls precipitation and the amount of reflected sunlight (Adams 2002; Riipinen et al. 2012; Hoffmann, Zetzsch and Rossi 2007). In order for particles to become CCNs, they need to have a size of at least 30 nm to 100 nm (Riipinen et al. 2011; Riipinen et al. 2012). Furthermore, the condensational behaviour of semivolatile organic compounds (SVOCs) remains largely unknown: If the major part of organic mass condenses on ultrafine particles, their growth to sizes at which they have an impact on the climate is enhanced. If in contrast most of the organic mass condenses on particles with diameters larger than 100 nm, the coagulation of ultrafine particles is increased and the total number of CCNs reduced (Riipinen et al. 2011). Therefore, better understanding of processes which lead to the formation and growth of atmospheric aerosol particles is of high importance.

The following sections will go into more detail on aerosol properties (see section 1.1.1) and how aerosol particles are formed in the atmosphere (see section 1.1.3). Additionally, fundamental physicochemical aspects of aerosols (see section 1.2) and physicochemical basics of the investigated reaction systems (see section 1.3) will be discussed. Sections 1.4 and 1.5 will go into some details on important analytical techniques.

1.1 Atmospheric aerosols

The term aerosol describes a suspension of solid or liquid particles in a gas, though often one refers to the particulate component only when aerosols are mentioned (Kulkarni, Baron and Willeke 2011; Pöschl 2005; Seinfeld and Pandis 2006; Kolb and Worsnop 2012; Hinds 1999). Aerosols are quite ubiquitous in the atmosphere with largely varying particle number concentrations between $1 \times 10^1\,\mathrm{cm}^{-3}$ in the stratosphere and $1 \times 10^5\,\mathrm{cm}^{-3}$ particles in urban areas (Curtius 2006; Seinfeld and Pandis 2006; Kulkarni, Baron and Willeke 2011).

Depending on their origin, aerosols are distinguished as being anthropogenic or natural (Pöschl 2005; Seinfeld and Pandis 2006). Typical sources of anthropogenic aerosols include fossil fuel combustion, waste and biomass burning as well as industrial emissions of sulphates and nitrates (Tomasi and Lupi 2016; Kulkarni, Baron and Willeke 2011; Hoffmann, Zetzsch and Rossi 2007). Sources of natural aerosols are e.g. volcanoes, sea spray and pollen (Kulkarni, Baron and Willeke 2011; Tomasi and Lupi 2016; Pöschl 2005; Curtius 2006; Hoffmann, Zetzsch and Rossi 2007).

Furthermore, aerosols are classified as primary or secondary depending on their formation (Pöschl 2005; Seinfeld and Pandis 2006; Curtius 2006; Hinds 1999; Hoffmann, Zetzsch and Rossi 2007). Primary aerosols are emitted directly into the atmosphere, whereas secondary aerosols are formed in the atmosphere through gas-to-particle conversion, i.e. the formation of sufficiently low volatile compounds to either form new particles (new particle formation (NPF)) through homogeneous condensation or to condensate on pre-existing particles (Curtius 2006; Seinfeld and Pandis 2006; Pöschl 2005; Shrivastava et al. 2017; George and Abbatt 2010; Tomasi and Lupi 2016; Hinds 1999; Hoffmann, Zetzsch and Rossi 2007).

1.1.1 Aerosol particle size and shape

The size of aerosol particles is the most important property that describes their behaviour (Kulkarni, Baron and Willeke 2011; John 2011; Ramachandran and Cooper 2011; Hinds 1999). As aerosols are defined as a suspension of particulate matter in a gas, particles need to stay suspended sufficiently long. Therefore, the upper size limit for aerosol particles usually is defined to be around 100 µm (1×10^{-4} m). The lower size limit is set somewhat arbitrarily to 1 nm (1×10^{-9} m) (John 2011; Kulkarni, Baron and Willeke 2011; Curtius 2006; Seinfeld and Pandis 2006; Riipinen et al. 2012; Pöschl 2005;

Tomasi and Lupi 2016; Ramachandran and Cooper 2011). However, the lower size limit is not well defined as there usually is no clear transition between molecular clusters and ultrafine aerosol particles (Kulkarni, Baron and Willeke 2011).

The size range spanned by aerosol particles amounts to five orders of magnitude (Kulkarni, Baron and Willeke 2011; Ramachandran and Cooper 2011; Seinfeld and Pandis 2006; John 2011; Hinds 1999). Generally, the size range is divided in fine and coarse particles, with the dividing line between the two regimes at about 2 µm (Whitby 1978; John 2011) to 2.5 µm (Tomasi and Lupi 2016; Seinfeld and Pandis 2006; Hinds 1999). Over the entire size range, their behaviour varies largely. Particles originate from different sources, are transported and deposited differently, they scatter light differently and have different effects on human health. Also, different physical laws govern their behaviour: As smaller particles up to about 500 nm are mainly influenced by Brownian motion, the movements of larger particles are governed by inertia and gravitation (Whitby 1978; Kulkarni, Baron and Willeke 2011; Ramachandran and Cooper 2011; Seinfeld and Pandis 2006; John 2011; Hinds 1999).

For spherical particles, the particle size can unambiguously be given as the particle's geometric diameter (Kulkarni, Baron and Willeke 2011; John 2011; Hinds 1999). Liquid particles usually occur as spheres, as well as many particles which have grown through the condensation of liquids from the gas phase (Hinds 1999; Kulkarni, Baron and Willeke 2011). Also secondary organic aerosol (SOA) particles have been observed both spherical (Virtanen et al. 2010) and non-spherical (Hallquist et al. 2009). On the other hand, dry particles as well as bioaerosols such as bacteria, pollen or fungal spores, often come in irregular shapes (Tomasi and Lupi 2016; Hinds 1999). Since most theories describing the behaviour of aerosol particles only take spherical particles into account, equivalent diameters are used to apply those theories to non-spherical particles as well (Kulkarni, Baron and Willeke 2011; Hinds 1999; John 2011; Ramachandran and Cooper 2011). Particles are assigned the size of a spherical particle with the same properties or behaviour (Kulkarni, Baron and Willeke 2011; Hinds 1999; John 2011; Ramachandran and Cooper 2011). Several different equivalent diameters are used such as the aerodynamic equivalent diameter, the diffusive equivalent diameter, or the electrical mobility equivalent diameter (John 2011; Kulkarni, Baron and Willeke 2011; Hinds 1999; Ramachandran and Cooper 2011). The assigned equivalent diameter depends on the type of measurement conducted, Scanning Mobility Particle Sizer (SMPS) measurements (see section 1.4.2 on page 29) would therefore yield the electrical mobility equivalent diameter (John 2011).

1.1.2 Aerosol particle size distribution

Aerosols in which all particles have the same size would be termed monodisperse (John 2011; Hinds 1999). A monodisperse aerosol is completely described by the particle diameter (Hinds 1999) and its geometric standard deviation equals 1.0 (Ramachandran and Cooper 2011). In reality, aerosols which consist of particles with a single diameter hardly ever exist and aerosols with a relatively small standard deviation of 1.1 to 1.2 are considered to be monodisperse (John 2011). However, as a result of several processes such as the accumulation of small particles and the breakup of larger ones, most aerosols consist of particles with a rather large range of different sizes and are accordingly called polydisperse (Hinds 1999; John 2011; Ramachandran and Cooper 2011). To describe such a distribution of particle sizes, statistical means are necessary (Hinds 1999; John 2011).

Whilst normal distributions are often used to describe the particle size distribution of monodisperse aerosols with small standard deviations, lognormal distributions are more appropriate to describe the particle size distribution of polydisperse aerosols originating from a single source (Ramachandran and Cooper 2011; Hinds 1999). The frequency distribution of particle sizes within an aerosol is often skewed, tailing towards larger particle sizes, whilst the same distribution often gets symmetrical when plotting against the logarithm of the particle size (Ramachandran and Cooper 2011; Hinds 1999; John 2011). Therefore, lognormal distributions are usually a good way to describe an aerosol population (Ramachandran and Cooper 2011; Hinds 1999; John 2011). The lognormal distribution is characterized – just as the normal or Gaussian distribution – by the geometric mean and the geometric standard deviation, which are calculated according to equations 1.1 and 1.2,

$$\log(d_g) = \frac{\sum_{i=1}^{N} n_i \log(d_i)}{\sum_{i=1}^{N} n_i} \tag{1.1}$$

$$\log(\sigma_g) = \sqrt{\frac{\sum_{i=1}^{N} n_i \left(\log(d_i) - \log(d_g)\right)^2}{\sum_{i=1}^{N} n_i - 1}} = \sqrt{\frac{\sum_{i=1}^{N} n_i \left(\log\left(\frac{d_i}{d_g}\right)\right)^2}{\sum_{i=1}^{N} n_i - 1}} \tag{1.2}$$

where d_g is the geometric mean, N is the total number of particles, n_i is the number of particles with a diameter of d_i and σ_g is the geometric standard deviation (Ramachandran and Cooper 2011; Hinds 1999).

Frequently, size distributions are given as count or number distributions, which give the fraction of the total number of particles which is to be found at a certain particle size (Hinds 1999; John 2011). Similarly, particle size distributions can be weighted by mass, volume or surface area instead of particle numbers (Hinds 1999; John 2011; Ramachandran and Cooper 2011). Some distributions as e.g. the mass distribution can be obtained directly with appropriate instruments (Hinds 1999; John 2011). Alternatively, such distributions may be calculated from the number size distribution (John 2011; Hinds 1999).

Transferring a lognormal number size distribution into another, differently weighted distribution will yield a lognormal distribution as well. This is a unique property of lognormal distributions. The new distribution will exhibit the same standard deviation as the original number size distribution, only the geometric mean of the distribution will shift (Hinds 1999).

When transforming aerosol number distributions to volume distributions, Whitby discovered that atmospheric aerosols usually show a trimodal distribution (Whitby 1978; John 2011). The three modes were labelled transient nuclei, accumulation and coarse mode (Whitby 1978; John 2011). Whilst the coarse mode mainly contains primary aerosols, secondary aerosols make up the transient nuclei and accumulation mode (Seinfeld and Pandis 2006; John 2011; Whitby 1978). Though being the smallest mode in terms of particle size and mass concentration, the transient nuclei mode usually contains the largest number of particles (John 2011; Whitby 1978; Hinds 1999). In more recent publications, the transient nuclei mode is further divided in the nuclei or nucleation mode and the Aitken mode (Seinfeld and Pandis 2006; Curtius 2006; Tomasi and Lupi 2016). The limits of these size ranges are not consistent throughout the literature, as the boundaries of the Aitken mode are ranging from 10 nm to 100 nm (Seinfeld and Pandis 2006), 5 nm to 50 nm (Tomasi and Lupi 2016), 5 nm to 100 nm (John 2011) and 20 nm to 90 nm (Curtius 2006). Particles in the nucleation and Aitken mode are formed through condensation of hot vapours and homogeneous nucleation of gaseous species (Seinfeld and Pandis 2006; Tomasi and Lupi 2016; Whitby 1978; John 2011). Figure 1.2 shows the typical trimodal size distribution.

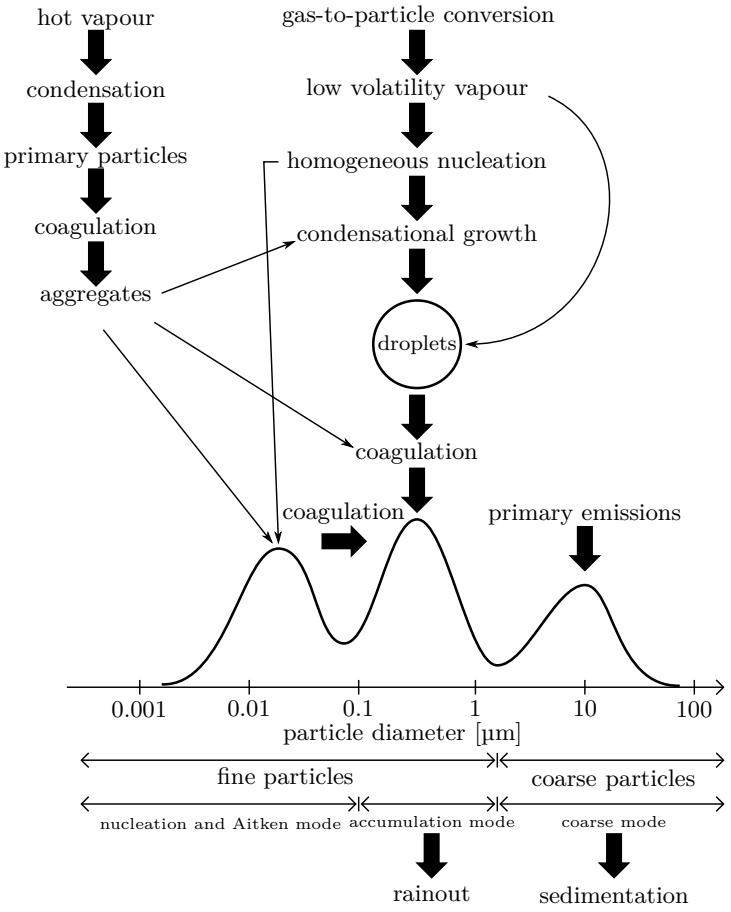

Figure 1.2: Schematic representation of the trimodal distribution of the particle surface area of an atmospheric aerosol. Shown are the modes as well as some aerosol formation and removal mechanisms. Figure adapted from Seinfeld and Pandis (2006).

The limits of the accumulation mode described in literature vary as well, as Curtius (2006) assumes a range from 90 nm to 1000 nm, Seinfeld and Pandis (2006) suppose 100 nm to 2500 nm, Tomasi and Lupi (2016) 50 nm to 2000 nm, Willeke and Whitby (1975) 100 nm to 1000 nm and John (2011) 100 nm to 2000 nm. Particles in accumulation mode are formed through the coagulation and the condensational growth of smaller particles (Tomasi and Lupi 2016; Seinfeld and Pandis 2006; Willeke and Whitby 1975; John 2011; Hinds 1999). The atmospheric lifetimes of particles in this mode are higher than those of particles from the other modes due to less efficient removal mechanisms (Tomasi and Lupi 2016; Seinfeld and Pandis 2006; Hinds 1999). Particles in the accumu-

lation mode account for a significant part of the total particle mass and for the major fraction of the aerosol surface area (Seinfeld and Pandis 2006; Hinds 1999). Particles in accumulation mode play an important role in visibility reduction, as their geometric mean is close to the peak of the light scattering curve for sunlight (John 2011; Hinds 1999).

Less research has gone into the investigation of coarse mode particles due to less health concerns (John 2011). Nonetheless, for this mode also different lower limits are discussed in literature: Curtius (2006) and Willeke and Whitby (1975) suppose 1 µm to be the lower limit, John (2011) assumes a lower limit of 2 µm, and Seinfeld and Pandis (2006) as well as Tomasi and Lupi (2016) imagine a lower boundary of 2.5 µm. Typical sources of coarse mode aerosol particles are sea spray, wind blown dust, biological particles and – in urban areas – road dust generated by vehicles (John 2011; Seinfeld and Pandis 2006; Hinds 1999).

As many other aerosol properties, the removal of aerosol particles from the atmosphere depends on the size of the aerosol particles, as does the atmospheric lifetime (Seinfeld and Pandis 2006). Due to their relatively high mass and considerable sedimentation velocities, coarse particles are mainly removed from the atmosphere through sedimentation and have comparably low atmospheric lifetimes (Seinfeld and Pandis 2006; Hoffmann, Zetzsch and Rossi 2007). Nucleation and Aitken mode particles are mainly lost through coagulation with particles from either the nuclei or accumulation mode (Seinfeld and Pandis 2006; Hinds 1999). Furthermore, they may act as CCNs and be subsequently lost in the form of rain droplets (rainout) (Hinds 1999). As the removal mechanisms are much less efficient for particles in the accumulation mode, their atmospheric lifetimes are usually considerably higher. Accumulation mode particles are mainly lost from rainout or washout, but they do not usually coagulate to form coarse mode particles (Hinds 1999; Seinfeld and Pandis 2006).

1.1.3 Secondary aerosol formation

The formation of secondary organic aerosols has long been observed as blue haze, especially over forested areas, and often has been eponymous for mountain ranges such as the Great Smoky Mountains and the Blue Ridge Mountains on the border between North Carolina and Tennessee. Written records of blue haze date back to Leonardo da Vinci, though little has been known about its origin (Went 1960; Hoffmann, Zetzsch and Rossi

2007). As late as 1960, Went (1960) suggested the formation of sub-micrometre particles from organic compounds as the source for the blue haze (Went 1960).

Nowadays, it is widely accepted that organic aerosols make up a large fraction of 20 % to 90 % of the sub-micrometre particulate mass and that a large fraction of the total organic aerosol is considered to be of secondary nature (Jimenez et al. 2009; Kroll and Seinfeld 2008; Gordon et al. 2017). According to Goldstein and Galbally (2007), the total organic aerosol burden is dominated by SOA. However, the knowledge about the composition, sources and chemistry of organic aerosols is still quite limited (Goldstein and Galbally 2007; Kroll and Seinfeld 2008).

1.1.3.1 Nucleation and condensation of SOA compounds

As has been mentioned before, secondary organic aerosols are formed in the atmosphere through the mass transfer of organic substances with low vapour pressures from the gas phase to the particle phase (Seinfeld and Pandis 2006; Pöschl 2005; Curtius 2006).

Nucleation is defined as the clustering of molecules to reach a certain size, at which the newly formed particle is thermodynamically stable (Sellegri and Boulon 2016; Andreae 2013). The main barrier for the formation of new particles is the surface energy, which must be overcome (Sellegri and Boulon 2016; Curtius 2006). Once this energy barrier is surmounted, the newly formed particle will grow through the condensation of molecules to the particle and through coagulation, i.e. the collision of particles (Sellegri and Boulon 2016).

Aerosol nucleation has been described by classical nucleation theory (CNT) in the late 1920's by Volmer and Weber (1926) and Farkas (1927). Although additions have been made, CNT still is the basis for the rendition of aerosol nucleation (Curtius 2006).

The simplest model for the representation of the nucleation process is the unary system model (USM), which assumes a single species leading to the formation of new particles (Sellegri and Boulon 2016). As nucleation in the atmosphere is almost always a process involving multiple different species (as e.g. the binary mixture of sulphuric acid and water or the ternary system sulphuric acid – ammonia – water), the USM has no practical relevance in atmospheric science (Curtius 2006; Sellegri and Boulon 2016). Nonetheless, a quick overview over the thermodynamics of the unary system will be given here.

Supersaturation, a prerequisite for nucleation in the unary system, is given when the partial pressure of a species A (p_A) exceeds the saturation vapour pressure (p_S) over a flat surface of liquid A. The saturation ratio S, as defined in equation 1.3,

$$S = \frac{p_A}{p_S} \tag{1.3}$$

is $S < 1$ for unsaturated vapours, $S = 1$ for saturated vapours and $S > 1$ for supersaturated vapours (Curtius 2006; Sellegri and Boulon 2016). In the presence of a surface, e.g. aerosol particles, on which the vapour could condense, condensation would occur until the gas phase is no longer supersaturated (Curtius 2006; Seinfeld and Pandis 2006; Sellegri and Boulon 2016). In the absence of a surface, the system is metastable, as its Gibbs free energy ΔG could be reduced through the formation of a condensed phase, as equation 1.4 demonstrates (Curtius 2006; Sellegri and Boulon 2016):

$$\Delta G = -\frac{4}{3}\pi r_p^3 \frac{\mathrm{k_B} T}{V_l} \ln(S) + 4\pi r_p^2 \gamma \tag{1.4}$$

Here, r_p is the radius of the nucleating particle, $\mathrm{k_B}$ is the Boltzmann constant, T the temperature, V_l is the volume each molecule occupies, and γ is the surface tension (Curtius 2006; Sellegri and Boulon 2016). In a supersaturated system, S will be larger than one and hence the first term on the right hand side will be negative, which is the driving force for the condensation of gas-phase molecules. For small particles, the second term representing the surface energy comes into play, as initially the surface energy is larger than the energy gained from the phase transfer, thus representing an energy barrier for the nucleation of new particles (Curtius 2006; Sellegri and Boulon 2016).

The critical radius or Kelvin radius r_p^* for a cluster is at the location of the maximum of the energy barrier. Clusters below the critical size are more likely to evaporate and larger clusters are formed only statistically. Upon reaching this size, the nucleus will most probably grow further by condensation of molecules from the gas phase (Curtius 2006; Sellegri and Boulon 2016). The height of the barrier and the location of the maximum can be obtained from differentiating equation 1.4.

The rate at which new particles are formed is called the nucleation rate J, which is linked to the height of the nucleation barrier, as can be seen in equation 1.5, where C is a pre-exponential factor (Curtius 2006; Sellegri and Boulon 2016):

$$J = C \exp\left(-\frac{\Delta G'}{\mathrm{k_B} T}\right) \tag{1.5}$$

As the saturation vapour pressure of mixtures of multiple components usually decreases, nucleation events in which more than one species participate are much more common in the atmosphere (Curtius 2006; Sellegri and Boulon 2016). The most prominent examples are the binary nucleation of sulphuric acid in the presence of water and the ternary nucleation of sulphuric acid, ammonia and water (Curtius 2006; Sellegri and Boulon 2016). However, also some organic species such as products from the oxidation of sesquiterpenes can participate in nucleation (Curtius 2006).

Whilst nucleation often is dominated by sulphuric acid, ambient sulphuric acid concentrations are generally considered to be too low to explain the growth rates of freshly nucleated particles (Riipinen et al. 2011; Curtius 2006). Therefore, other presumably organic species are thought to be the major driver of particle growth (Riipinen et al. 2011; Donahue et al. 2011; Kulmala et al. 2004) or are even considered to be of similar importance for nucleation as sulphuric acid (Kirkby et al. 2016).

Supersaturated organic species can condense on freshly nucleated particles and initiate particle growth. However, once particles contain an organic fraction, organic species can partition into the particle phase driven by dissolution without the need for a threshold concentration (Seinfeld and Pandis 2006; Hallquist et al. 2009). The theory of phase partitioning has been developed in the 1990's by Pankow and was extended by Odum to describe SOA formation (Hallquist et al. 2009). The equilibrium partitioning coefficient $K_{p,\,i}$ or its inverse, the saturation vapour concentration C_i^*, is used to describe the partitioning of each species i:

$$\frac{C_i^p}{C_i^g} = K_{p,\,i} C_{OA} = \frac{C_{OA}}{C_i^*} \tag{1.6}$$

Here, C_i^p and C_i^g are the mass concentrations of i per unit volume of air in the particle and gas phase, respectively. C_{OA} is the mass concentration per unit volume of air of the total absorbing condensed phase (Hallquist et al. 2009). From equation 1.6, the fraction F_i of a semivolatile compound in the particle phase can be estimated (Hallquist et al. 2009):

$$F_i = \frac{C_i^p}{C_i^p + C_i^g} = \frac{C_{OA} K_{p,\,i}}{1 + C_{OA} K_{p,\,i}} = \frac{1}{1 + \frac{C_i^*}{C_{OA}}} \tag{1.7}$$

With increasing amounts of absorbing particle phase, the partitioning of compounds of higher volatility into the particle phase will increase. These compounds may evaporate back into the gas phase, e.g. in case of dilution of the aerosol, and form species of lower volatility in gas-phase oxidation reactions, or remain in the condensed phase and react in multiphase or heterogeneous reactions to form products of lower volatility.

1.1.3.2 Formation of SOA compounds

According to Riipinen et al. (2012), the most important mechanism for the formation of secondary organic aerosols is the formation of condensable vapours from the oxidation of volatile organic compounds (VOCs). On a global scale, biogenic VOC (BVOC) emissions exceed anthropogenic emissions, though on a regional scale, anthropogenic emissions might be dominant (Goldstein and Galbally 2007; Riipinen et al. 2012; Pöschl 2005). The most prominent BVOCs are isoprene (2-methylbuta-1,3-diene, C_5H_8) and monoterpenes, amongst which α-pinen is the most emitted one (Kesselmeier and Staudt 1999; Hoffmann, Zetzsch and Rossi 2007). Typical atmospheric oxidants for the VOC oxidation are the OH radical ($OH^\bullet$), ozone (O_3) and nitrate radicals ($NO_3^\bullet$) (Hoffmann, Zetzsch and Rossi 2007; Kulmala et al. 2004; Kroll and Seinfeld 2008; Seinfeld and Pandis 2006).

The oxidation of VOCs yields multifunctional oxidation products such as ketoaldehydes, ketocarboxylic acids and dicarboxylic acids, which have – due to their chemical functionalities – lower vapour pressures than the initial VOCs (Hoffmann, Zetzsch and Rossi 2007; Kulmala et al. 2004; Seinfeld and Pandis 2006). Their lower volatility will cause these products to partition to the particle phase, either by condensing onto pre-existing particles or by forming new particles (Hoffmann, Zetzsch and Rossi 2007; Shrivastava et al. 2017; George and Abbatt 2010; Kulmala et al. 2004). However, often more than one oxidation step is required to form compounds of sufficiently low volatility (Goldstein and Galbally 2007; Seinfeld and Pandis 2006). Figure 1.3 shows a simplified pathway for the oxidation of VOCs.

The attacking oxidant as well as the reactions of the peroxy radical ($RO_2^\bullet$) and the oxy radical ($RO^\bullet$) govern the product distribution (Hallquist et al. 2009; Kroll and Seinfeld 2008). Oxidation reactions by radicals such as $OH^\bullet$, $NO_3^\bullet$ or halogen atoms are usually initiated by the abstraction of a hydrogen atom or the addition to a C=C double bond. If the oxidant is added to the double bond, the volatility is decreased according to the

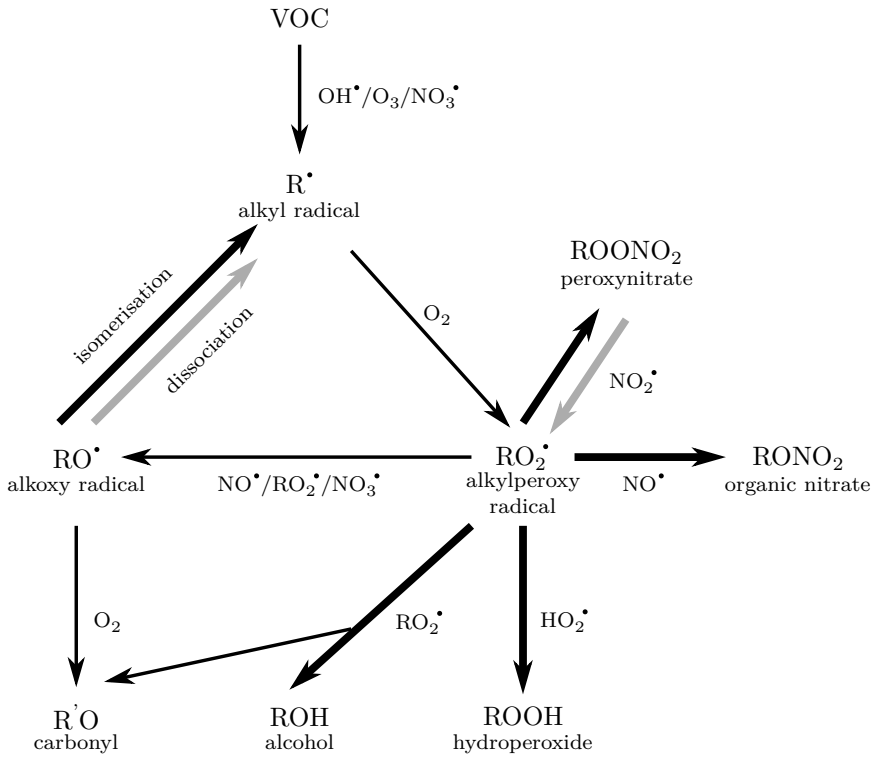

Figure 1.3: Schematic of the VOC oxidation by different oxidants. Thick black arrows indicate reactions that can lead to a significant decrease in volatility, gray arrows indicate reactions that can substantially increase volatility. Details of the ozonolysis of alkenes are omitted. Figure adapted from Kroll and Seinfeld (2008).

specific functional group which is added, whilst the nature of the attacking radical does not matter in the case of hydrogen abstraction (Kroll and Seinfeld 2008).

After the initial formation of alkyl radicals, these quickly form alkylperoxy radicals ($RO_2^\bullet$) (Kroll and Seinfeld 2008). Further reactions depend on the gas-phase composition, namely the NO_x (NO and NO_2) concentrations: At low-NO_x conditions, the alkylperoxy radicals tend to react with $HO_2^\bullet$ to form hydroperoxides (ROOH). These hydroperoxides are of relatively low volatility and have been shown to be major constituents of SOA formed from alkene ozonolysis and low-NO_x isoprene photooxidation (Kroll and Seinfeld 2008; Hallquist et al. 2009). Besides the formation of hydroperoxides, alkylperoxides may also undergo self- and cross-reactions to form alkoxy radicals ($RO^\bullet$) or an alcohol and a carbonyl compound. Furthermore, the self-reaction of large

alkylperoxides may lead to the formation of organic peroxides with very low volatilities (Kroll and Seinfeld 2008; Hallquist et al. 2009).

Under high-NO_x conditions, $RO_2^\bullet$ reacts with $NO^\bullet$ to form organic nitrates ($RONO_2$), which goes along with a decrease in volatility. Though nitrates have been found in laboratory and in ambient aerosol samples, less than 25 % of $RO_2^\bullet$ react through this channel (Kroll and Seinfeld 2008; Hallquist et al. 2009). The reaction of alkylperoxy radicals with nitrogen dioxide ($NO_2^\bullet$) leads to the reversible formation of peroxynitrates ($ROONO_2$). Peroxynitrates are of very limited stability and act as reservoirs for both alkylperoxy radicals and NO_x. Nonetheless, they likely can partition into the particle phase, where they may decompose to yield $RO_2^\bullet$ for further reactions (Kroll and Seinfeld 2008). The main channel for the reaction of $RO_2^\bullet$ radicals under high-NO_x conditions is the formation of alkoxy radicals ($RO^\bullet$) (Kroll and Seinfeld 2008; Hallquist et al. 2009).

There are three pathways for the reaction of alkoxy radicals. Firstly, alkoxy radicals may undergo dissociation, i.e. the cleavage of a carbon-carbon bond next to the alkoxy functionality to yield a carbonyl and an alkyl radical. Secondly, the alkoxy radical may isomerize in a 1,5-hydrogen shift to form a 4-hydroxyalkyl radical. Lastly, by reacting with oxygen, a carbonyl and $HO_2^\bullet$ are formed. The molecular structure of the alkoxy radical strongly influences the rates of reaction, therefore the main reaction channel may vary from radical to radical (Kroll and Seinfeld 2008; Hallquist et al. 2009).

The pathway for the oxidation by ozone differs from the oxidation by radicals, as can be seen in figure 1.4. After the addition of ozone to the C=C double bond in a 1,3-dipolar cycloaddition, the bond is cleaved to yield a carbonyl and the Criegee intermediate. The Criegee intermediate can be quenched to form the stabilized Criegee intermediate, which in turn reacts with water or oxygenated organic compounds (SCI channel) (Kroll and Seinfeld 2008; Hallquist et al. 2009). If no quenching occurs, the Criegee intermediate decomposes to form a hydroxyl radical and an alkyl radical, which can react further as shown in figure 1.3 and described above (Kroll and Seinfeld 2008; Hallquist et al. 2009).

Other than lower volatility products, smaller components may be formed as well, which will remain in the gas phase and potentially influence gas phase chemistry (Hoffmann, Zetzsch and Rossi 2007; Kroll and Seinfeld 2008). Besides gas-phase oxidations, other processes involving the condensed phase can potentially produce SOA compounds as well. The particle-phase reaction of organic acids and amines or ammonia might yield organic salts with low volatilities (Riipinen et al. 2012). Furthermore, higher molecular

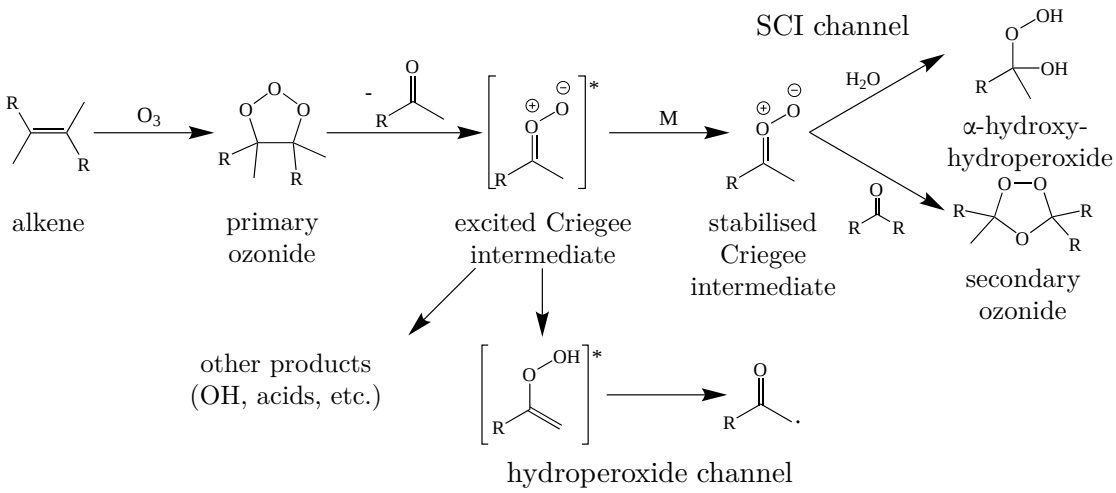

Figure 1.4: Schematic of the ozonolysis of alkenes. Figure adapted from Kroll and Seinfeld (2008).

weight (MW) compounds can be formed in the condensed phase through oligomerisation and/or polymerisation reactions, as has been observed in both biogenic and anthropogenic SOA (Riipinen et al. 2012; Hoffmann, Zetzsch and Rossi 2007; Hoffmann et al. 1998). From laboratory experiments, between 25 % and 70 % of the SOA mass is estimated to consist of oligomeric compounds (Hallquist et al. 2009). Esterifications, the formation of anhydrides as well as the acid catalysed formation of acetals, hemiacetals and aldol condensations are typically associated with the formation of higher MW compounds. Often reaction mechanisms are unclear and oligomers have also been observed in the absence of acids (Hoffmann, Zetzsch and Rossi 2007; Hallquist et al. 2009; Kroll and Seinfeld 2008). The formation of esters is suspected to not only happen through the condensation reaction of a carboxylic acid and an alcohol, but might also involve epoxides and anhydrides as starting materials (Hallquist et al. 2009).

Additionally, also the uptake of small carbonyl compounds with relatively high vapour pressures from the gas phase followed by a chemical reaction which makes the uptake irreversible, has been observed (Hoffmann, Zetzsch and Rossi 2007; Seinfeld and Pandis 2006; Kroll and Seinfeld 2008). Acid catalysed acetal/hemiacetal formations and aldol reactions are possible mechanisms involved in reactive uptake processes (Hallquist et al. 2009; Hoffmann, Zetzsch and Rossi 2007; Pöschl 2005). Besides the reactions mentioned before, the recombination of radicals in the gas phase and radical polymerisations in cloud droplets may lead to compounds with high molecular weights

and low volatilities (Hoffmann, Zetzsch and Rossi 2007; Hallquist et al. 2009). The production of high MW compounds in the gas phase might be important in new particle formation (Hallquist et al. 2009).

1.2 Physicochemical effects of particle size

In section 1.1.3.1, the Kelvin diameter has already shortly been introduced. In this section, the Kelvin effect will be explained a little further, as will be the equation of Young and Laplace.

1.2.1 The Kelvin effect

The equilibrium partial pressure over a flat liquid surface at a given temperature is called the saturation vapour pressure p_S. In case of a strongly curved surface, fewer molecules are in immediate vicinity to a molecule at the surface, therefore the attractive forces between the molecules at the surface are reduced, and evaporation is facilitated. In order to maintain mass equilibrium, the partial pressure of vapour p_A around the droplet must be greater than the saturation vapour pressure (Hinds 1999, 2011; Seinfeld and Pandis 2006).

To assess the effect of curvature on the equilibrium vapour pressure, the change in Gibbs free energy ΔG upon the formation of a droplet with a radius r_p and n molecules of a pure liquid A is estimated:

$$\Delta G = G_{droplet} - G_{vapour} \tag{1.8}$$

If the total number of vapour molecules initially is N, after the formation of the droplet remain $N_1 = N_0 - n$ molecules in the gas phase. Assuming the Gibbs free energies of a molecule in the gas and liquid phase to be g_v and g_l, respectively, equation 1.8 becomes equation 1.9. As a new surface is created upon the formation of a droplet, the surface energy $4\pi r_p^2\gamma$ with the surface tension γ and the particle radius r_p has to be taken into account (Seinfeld and Pandis 2006).

$$\Delta G = N_1 g_v + n g_l + 4\pi r_p^2 \gamma - N_0 g_v \tag{1.9}$$

The number of molecules in the droplet and the droplet radius are connected by equation 1.10.

$$n = \frac{4\pi r_p^3}{3V_l} \tag{1.10}$$

Rewriting equation 1.9 and substituting with equation 1.10 yields equation 1.11, where V_l denotes the volume occupied by a single molecule in the liquid phase (Seinfeld and Pandis 2006).

$$\Delta G = \frac{4\pi r_p^3}{3V_l}(g_l - g_v) + 4\pi r_p^2 \gamma \tag{1.11}$$

The number of molecules and the temperature do not change. Therefore, employing equation 1.12, the energy difference between a molecule in the liquid and in the gas phase can be written as $g_l - g_v = (V_l - V_v)dp$. As the volume occupied by a molecule in the gas phase V_v is much larger than the volume occupied by a molecule in the liquid phase, this simplifies to $g_l - g_v = -V_v dp$. Further assuming the gas phase to be ideal, one obtains $V_v = \mathrm{k_B}T/p$. Integration leads to equation 1.13 (Seinfeld and Pandis 2006).

$$dG = -SdT + Vdp + \sum_{i=1}^{k} \mu_i dn_i \tag{1.12}$$

$$g_l - g_v = -\mathrm{k_B}T \int_{p_S}^{p_A} \frac{dp}{p} = -\mathrm{k_B}T \ln \frac{p_A}{p_S} \tag{1.13}$$

In equation 1.3 the ratio of p_A and p_S has been defined as the saturation ratio. When substituting 1.13 into 1.11, equation 1.4 is obtained. ΔG reaches a maximum ΔG^* at $r_p = r_p^*$. The radius at the maximum can be computed by setting $\delta \Delta G / \delta r_p = 0$ to yield equation 1.14 (Seinfeld and Pandis 2006; Sellegri and Boulon 2016).

$$r_p^* = \frac{2\gamma V_l}{\mathrm{k_B}T \ln(S)} \tag{1.14}$$

Rearranging yields equation 1.15, a common representation of the Kelvin equation (Seinfeld and Pandis 2006),

$$\frac{p_A}{p_S} = \exp\left(\frac{2\gamma V_l}{\rho \mathrm{k_B} T r_p^*}\right) \tag{1.15}$$

which can also be written in terms of molar units as in equation 1.16 (Seinfeld and Pandis 2006; Hinds 1999, 2011):

$$\frac{p_A}{p_S} = \exp\left(\frac{2\gamma M}{\rho \mathrm{R} T r_p^*}\right) \tag{1.16}$$

In equation 1.16, M and ρ denote the molecular mass and density of the liquid constituting the droplet. r_p^* is the Kelvin radius, the radius of a droplet which will neither

evaporate nor grow (Hinds 1999, 2011). For a given saturation ratio, only particles with a Kelvin radius of r_p^* are stable, larger particles will grow, while particles with a radius $r < r_p^*$ will evaporate. Conversely, for every particle size a certain saturation ratio exists, at which particles are stable. At higher saturations particles will grow, while at lower saturations particles will shrink (Hinds 1999, 2011).

The right hand side term of equation 1.16 is always positive, therefore the saturation ratio is always greater than unity. Accordingly, supersaturation is needed at all times to prevent particles from evaporating. This is called the Kelvin effect. The Kelvin equation is only valid for pure liquids, as impurities or electric charges have an influence on the vapour pressures and therefore change the situation (Hinds 1999).

1.2.2 Laplace pressure

As has already been mentioned in sections 1.1.3.1 and 1.2.1, the surface energy of a system amounts to $4\pi r_p^2\gamma$. The reduction of the surface area therefore leads to a reduction of the total free energy by $8\pi r\gamma dr$. The tendency to shrink is balanced by a pressure difference across the surface Δp in such a way that the work necessary to counteract the pressure equals the decrease in energy (Adamson and Gast 1997)

$$8\pi r\gamma dr = \Delta p 4\pi r_p^2 dr \tag{1.17}$$

which simplifies to yield equation 1.18, the equation of Young and Laplace.

$$\Delta p = \frac{2\gamma}{r_p} \tag{1.18}$$

The pressure difference across a curved surface is called Laplace pressure. If the object of interest is not spherical, it might be necessary to describe the curved surface by two radii of curvature, r_1 and r_2 (Adamson and Gast 1997; Butt, Graf and Kappl 2003; Gennes, Brochard-Wyart and Quéré 2009):

$$\Delta p = \gamma\left(\frac{1}{r_1} + \frac{1}{r_2}\right) \tag{1.19}$$

The equation of Young and Laplace has several important consequences. Firstly, the pressure difference across a liquid surface can be calculated if the shape of the surface is known. Secondly, without external fields, the pressure is the same throughout the liquid. The pressure therefore is constant and accordingly the radius of curvature must be the

Table 1.1: Calculated pressures in aerosol particles. Pressures are calculated for two different surface tensions and different particle sizes.

	pressure Δp [bar]	
particle diameter [nm]	$\gamma = 73\,\mathrm{mN\,m^{-1}}$	$\gamma = 44.4\,\mathrm{mN\,m^{-1}}$
1000	2.5	1.9
100	15.6	9.9
10	147	89.8
1	1461	889

same everywhere. Lastly, the equilibrium shape of a liquid surface can be calculated, if the pressure difference as well as some conditions like the volume of the liquid and the surface tension are known (Butt, Graf and Kappl 2003).

For aerosol droplets with a diameter of 1 µm, the pressure inside the droplets is comparable to the atmospheric pressure (Gennes, Brochard-Wyart and Quéré 2009). However, with decreasing particle size, the pressure difference across the particle surface increases. Table 1.1 gives pressures for particles of different sizes. Pressures are calculated for the surface tension of water ($73\,\mathrm{mN\,m^{-1}}$ (Gennes, Brochard-Wyart and Quéré 2009)) and typical SOA compounds at 67 % relative humidity ($44.4\,\mathrm{mN\,m^{-1}}$ (Hritz, Raymond and Dutcher 2016)).

1.2.3 The Tolman length

According to Tolman (1949), the surface tension is expected to be a function of the particle radius. Tolman estimated from theoretical considerations that the surface tension would decrease with decreasing droplet size. Blokhuis and Kuipers (2006) give equation 1.20 for the surface tension of a liquid droplet of radius r.

$$\gamma(r) = \gamma\left(1 - \frac{2\delta}{r}\right) \tag{1.20}$$

Here, δ is the Tolman length. As both the Kelvin equation and the Young-Laplace equation are a function of the surface tension and are most interesting at small particle sizes, a particle size-dependence of the surface tension might have an impact on our understanding of e.g. nucleation. However, both the sign and the magnitude of the Tolman length have been discussed in literature. Several authors report values for the Tolman length on the order of a fraction of a nanometre, making such effects significant

only for smaller clusters (Bruot and Caupin 2016; Adamson and Gast 1997; Giessen and Blokhuis 2009). Therefore, the curvature dependence of the surface tension most probably does not come into play for aerosol particles of a few nanometres and more.

1.3 Chemical basics of the reaction systems

1.3.1 Pressure dependence of chemical reactions

In many chemical reactions, the volumes of the reactant(s), the transition state and the product(s) will differ. The changes in volume are commonly referred to as activation volume and reaction volume. The activation volume ΔV^* is the difference between the volume of the transition state and the reactant(s), whereas the term reaction volume ΔV_R describes the difference in volume between the product(s) and reactant(s), as equations 1.21 and 1.22 show.

$$\Delta V^* = V^* - V_E \tag{1.21}$$

$$\Delta V_R = V_P - V_E \tag{1.22}$$

Here, V^* denotes the volume of the transition state and V_E and V_P the volumes of the educt(s) and product(s), respectively (Jenner 2002; Asano and Le Noble 1978). A decrease in volume, leading to negative values for the activation and reaction volume, may result from several different processes: The formation of a new bond leads to a decrease in distance between the involved atoms from the Van der Waals distance to the bonding distance (3.6×10^{-10} m to 1.5×10^{-10} m in case of a C–C bond formation), thus reducing the occupied volume (Klärner, Diedrich and Wigger 1997; Benito-López et al. 2008; Borukhova et al. 2015; Klärner and Wurche 2000). Similarly, the formation of ions and – to a lesser extent – the increase of charges, leads to a decrease in volume due to the attractive interactions, an effect called electrostriction (Klärner, Diedrich and Wigger 1997; Benito-López et al. 2008; Borukhova et al. 2015; Klärner and Wurche 2000). Furthermore, reactions proceeding through cyclic transition states as well as reactions involving dipolar transition states exhibit negative activation and reaction volumes. Sterically hindered reactions may also show negative activation and reaction volumes (Benito-López et al. 2008; Borukhova et al. 2015; Jenner 2002; Klärner and Wurche 2000).

Negative activation volumes lead to an acceleration of the reaction at elevated pressures. The pressure reduces the Gibbs enthalpy of activation ΔG^* and therefore increases the rate constant k_p at pressure p. Conversely, reactions with positive activation volumes will be decelerated (Jurczak and Gryko 1997). Equation 1.23 connects the activation volume with pressure and the activation energy or else the rate constant.

R denotes the universal gas constant and T the temperature (Klärner and Wurche 2000; Asano and Le Noble 1978).

$$\Delta V^* = \left(\frac{\partial \Delta G^*}{\partial p}\right)_T = \left(\frac{-\partial \ln k_p}{\partial p}\right)_T \mathrm{R}T \tag{1.23}$$

Similarly, negative reaction volumes will lead to a shift in equilibrium towards the product(s) at increased pressures. This can be easily understood from the principle of Le Chatelier (Jurczak and Gryko 1997; Benito-López et al. 2008). Equation 1.24 shows the connection of the reaction volume with the Gibbs enthalpy ΔG and the equilibrium constant K_p at pressure p (Klärner and Wurche 2000).

$$\Delta V = \left(\frac{\partial \Delta G}{\partial p}\right)_T = \left(\frac{-\partial \ln K_p}{\partial p}\right)_T \mathrm{R}T \tag{1.24}$$

1.3.2 The Diels-Alder reaction

In the late 1920s, Otto Diels and Kurt Alder first reported the observation of a then new reaction (Diels and Alder 1928, 1929a, 1929b). The [4+2] cycloaddition has later been named after Diels and Alder (Bruckner and Harmata 2010; Wang 2010).

In a Diels-Alder reaction, a conjugated diene and a dienophile react to form a six-membered ring as is shown in figure 1.5. The diene and the dienophile will form two new σ bonds at the expense of two π bonds in a pericyclic reaction (Clayden, Greeves and Warren 2012). Diels-Alder reactions are one-step reactions, therefore no intermediates occur. In the transition state, all six π electrons taking part in the reaction are delocalised, giving the transition state an aromatic character (Clayden, Greeves and Warren 2012).

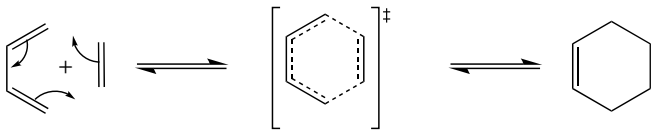

Figure 1.5: General reaction scheme of the Diels-Alder reaction.

To understand the mechanism of the Diels-Alder reaction, having a closer look at the frontier orbital description of the two reactants can help. The bonds are formed through the combination of a full and an empty orbital of appropriate symmetry. The corresponding orbitals in the Diels-Alder reaction are the HOMO (highest occupied

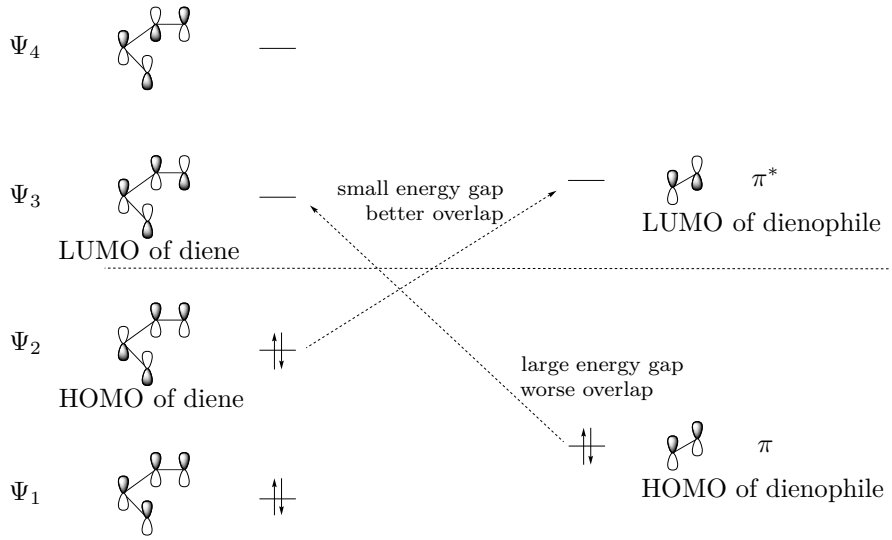

Figure 1.6: Frontier orbital description of the Diels-Alder reaction. Sketched are the energy levels of the HOMOs and LUMOs of a diene and an acceptor-substituted dienophile. Figure adapted from Clayden, Greeves and Warren (2012).

molecular orbital) of one reactant and the LUMO (lowest unoccupied molecular orbital) of the second reactant (Clayden, Greeves and Warren 2012).

Figure 1.6 shows the HOMOs and LUMOs of the diene and the dienophile. As can be seen, the orbitals of the HOMO of one reactant have the same symmetry as the LUMO orbitals of the second reactant and therefore can overlap to form two new σ bonds (Clayden, Greeves and Warren 2012). However, simple reactions as the one depicted in figure 1.5 will react only under harsh conditions. Therefore, Diels-Alder reactions are mostly carried out with acceptor-substituted and hence electron-deficient dienophiles and donor-substituted and thus electron rich dienes (Bruckner and Harmata 2010; Wang 2010; Clayden, Greeves and Warren 2012; Becker 2001). The acceptor-substitution of the dienophile leads to a decrease of the energy of the LUMO, while the donor-substitution of the diene increases the HOMO energy. Therefore, the energy gap is reduced and the reaction facilitated. Alternatively, in inverse electron demand Diels-Alder reactions donor-substituted dienophiles react with acceptor-substituted dienes (Clayden, Greeves and Warren 2012; Bruckner and Harmata 2010; Becker 2001).

As many other chemical reactions, the Diels-Alder reaction is strongly influenced by pressure. Due to the negative activation and reaction volumes, Diels-Alder reactions

are accelerated and the equilibria are shifted towards the products at higher pressures. The activation and reaction volumes are comparably large in magnitude, which makes the effect of pressure more pronounced than in reactions with activation and reaction volumes smaller in magnitude (Klärner and Wurche 2000; Klärner, Diedrich and Wigger 1997; McCabe and Eckert 1974). Furthermore, Diels-Alder reactions are highly tolerant of functional groups (Hou et al. 2018). Therefore, Diels-Alder reactions seemed to be a suitable choice for the purposes of this study.

1.4 Aerosol measuring techniques

Over the last decades, the need for measuring aerosols has increased drastically. Aerosols are measured by federal agencies to quantify the exposure of populations towards particulate mass, scientists in atmospheric research measure aerosols to get a better understanding of their formation and their impact on the Earth's climate, and engineers and material scientist are interested in aerosols as means to produce novel materials (Kulkarni, Baron and Willeke 2011).

The measurement of different aerosol properties requires distinct instruments. In the following sections, a short overview of instruments for the measurement of particle concentrations and particle size distributions will be given and the instrumentation used in this study will be introduced. The chemical characterisation of aerosol particles will be discussed in section 1.5.

1.4.1 Measurement of particle concentrations

Several different methods for the measurement of particle concentrations exist. The most used offline method probably is the collection of aerosol particles on a suitable filter material, followed by weighing the filter. Dividing the mass on the filter by the sampling volume yields the mass concentration (Kulkarni and Baron 2011; Raynor et al. 2011). However, the filter sampling is time-consuming and the obtained particle concentrations will be averaged over the whole sampling time, therefore quick changes in the particle concentration will not be measurable (Kulkarni and Baron 2011).

In contrast, online methods provide much higher time resolution on the order of minutes or in real-time even. A popular instrument for the measurement of number concentrations is the Optical Particle Counter (OPC). Aerosol particles pass a beam of light and photodetectors detect the light scattered by each particle. As every particle causes a scattering event, the number of particles can be obtained from the number of light pulses detected by the optical sensors. Light scattering is in principal particle size-dependent, but the dependence on the particle surface and refractive index makes sizing inaccurate (Kulkarni and Baron 2011; Sorensen et al. 2011). As particle size decreases, the detection by light scattering becomes less sensitive. The lower size threshold is at about 100 nm under ideal conditions (Cheng 2011; Flagan 2011).

Condensation Particle Counters (CPC) as the ones used in this study allow for the measurement of smaller particles. In contrast to the OPC, particles are grown through

the condensation of a working fluid prior to the detection by light scattering (Kulkarni and Baron 2011; Cheng 2011; Hinds 1999). Particles reach – independently of their initial size – very similar diameters of 2 µm to 15 µm, the final size depends on operating conditions, system configuration and the particle number density (Cheng 2011; Hinds 1999).

The first step in a CPC measurement is the supersaturation of the gas phase with the working fluid. Typical working fluids in modern CPCs are water and *n*-butanol. Three operation principles have been realized in the past to initiate supersaturation and condensation, i.e. adiabatic expansion, thermal diffusion, and the mixing of hot and cold streams (Cheng 2011; Hinds 1999). Supersaturation then leads to condensation of the working fluid onto the aerosol particles in a second step. Thereby, the particles grow to a uniform size. Lastly, the grown particles are counted. While in the past particles were counted by eye, modern CPCs exploit light scattering (Cheng 2011).

Different types of CPCs with differing operation principles have been built. The first CPC built by Aitken in 1888 worked as an expansion-type CPC. The aerosol was saturated with water vapour at room temperature. Afterwards, supersaturation was achieved by cooling the aerosol by volume expansion or pressure relief. As CPCs of this type work in cycles, time resolution is worse than for continuously operating CPC, by which they have largely been replaced (Cheng 2011).

Thermal diffusion CPCs offer the advantage of continuous operation, especially important for coupling with diffusion batteries or Differential Mobility Analysers (see section 1.4.2)(Cheng 2011). Depending on the working fluid, their working principles vary. Conductive cooling CPC operate with alcohols such as *n*-butanol. The aerosol stream passes a heated reservoir, where the gas phase is saturated with the fluid. Afterwards, the aerosol reaches the cooled condenser. Supersaturation is initiated by gas cooling, whilst the gas phase concentrations of the working fluid remain high due the to slow transport to the condenser walls. The grown particles are then detected by light scattering (Cheng 2011; Hinds 1999).

Thermal diffusion CPCs, which run on water as working fluid, operate as differential diffusion CPCs. In a differential diffusion CPC, the aerosol flows through a wet-walled tube. In the first part of the growth tube, the conditioner, the temperature is reduced below room temperature and the gas phase is supersaturated with water. Afterwards, the aerosol passes a warmer part of the growth tube (initiator), in which water vapour from the wet walls migrates to the aerosol stream to supersaturate the gas phase. This is

only possible because the mass diffusivity of water is higher than the thermal diffusivity of air. Therefore, the aerosol remains at a lower temperature, which leads to condensational growth of the particles. A following colder part (moderator) of the growth tube removes excess water through condensation to the moderator walls. Growth of the particles continues to sizes which are optically detectable. Light scattering is employed for the detection of the grown particles (Cheng 2011; TSI Incorporated 2019). Figure 1.7 shows the schematic setup of the TSI Water-based Condensation Particle Counter (WCPC) Model 3789 employed in this study. The WCPC offers two different preconfigured temperature settings for the growth tube for the detection of particles with a lower size limit of 2 nm and 7 nm, respectively. Additionally, the temperatures can be configured freely. Also, the user has the choice of flow rates of either $1.5\,\mathrm{L\,min^{-1}}$ (high flow) or $0.6\,\mathrm{L\,min^{-1}}$ (low flow). In either mode, $0.3\,\mathrm{L\,min^{-1}}$ of the aerosol flow passes the growth tube while the rest is filtered and pumped out of the instrument. In the case of the high flow mode, the cross valve connects the bypass flow to the pump and closes the make-up air flow. In low flow mode, the bypass flow is shut and filtered make-up air is drawn in. The manufacturer suggests to operate the instrument in high flow mode to reduce diffusion losses and to increase the response time. The low flow mode serves in applications were aerosol flow rates might have to be reduced, e.g. in case of reduced sheath air flow in a SMPS system for increased size range (TSI Incorporated 2019).

Lastly, CPCs which create supersaturation by mixing hot and cold streams, are called mixing-type CPCs. The warmer flow consists of saturated vapours of the working fluid. Rapid mixing of the cold aerosol with the warm vapours leads to supersaturation and condensational growth of the aerosol particles, which can then be detected by light scattering (Cheng 2011).

1.4.2 Measurement of aerosol particle size distributions

As has been discussed in section 1.1.1, the size of an aerosol particle and accordingly the particle size distribution of an aerosol are probably the most important properties of aerosol particles and aerosols, respectively. Therefore, scientists working in aerosol research are naturally interested in measuring particle size distributions or size-classifying aerosol particles.

Instruments working with different principles can be used for the measurement of particle size distributions: Optical Particle Sizers use light scattering (see section 1.4.1), Aerodynamic Particle Sizers and impactors exploit the inertia of particles and the mo-

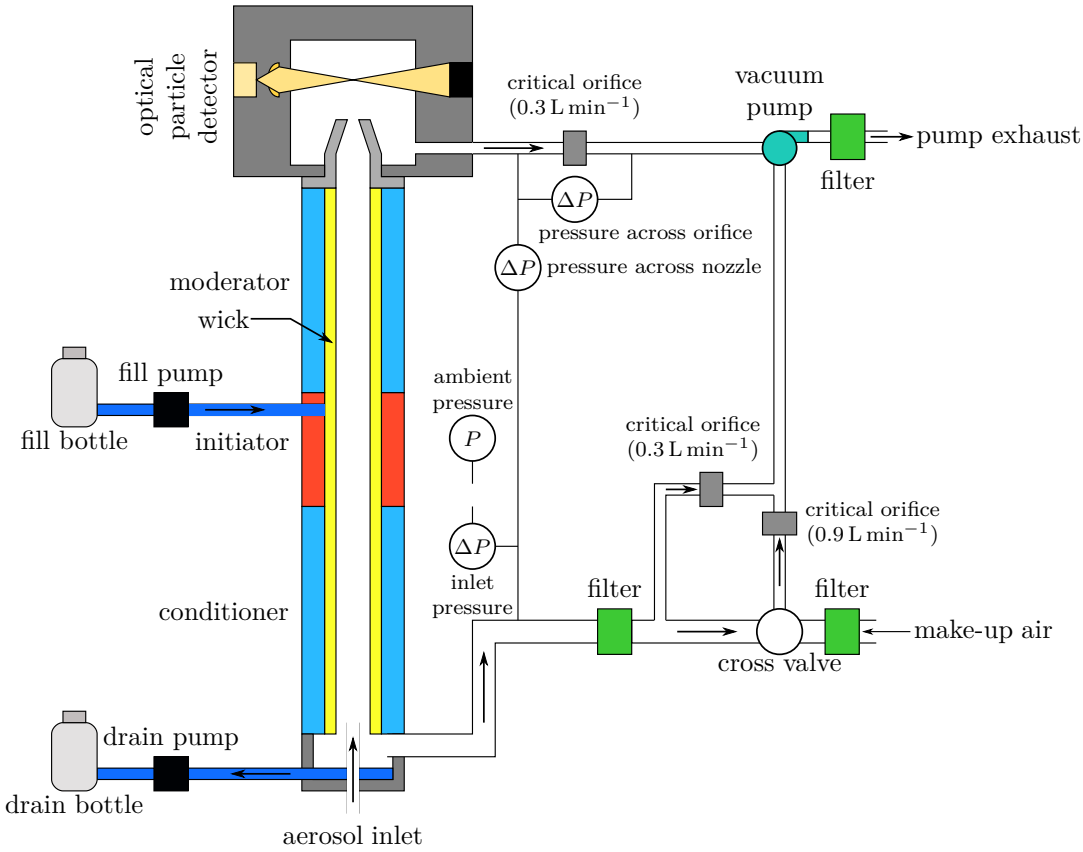

Figure 1.7: Schematic setup of the TSI Water-based Condensation Particle Counter Model 3789. Figure adapted from TSI Incorporated (2019).

bility of charged particles in an electrostatic field is employed by measurements using a Differential Mobility Analyser (DMA) (Sorensen et al. 2011; Baron et al. 2011; Flagan 2011; Hinds 1999).

Aerosol particles with diameters smaller than 100 nm are difficult to measure optically (see section 1.4.1). Due to their low mass and inertia, also methods based on inertia are mostly not suitable for the measurement of ultrafine particles (Flagan 2011). Therefore, an Electrostatic Classifier Model 3082 equipped with a Nano DMA Model 3085A was used in this study.

A DMA consists of two concentric electrodes, in between which a high voltage of up to 10 000 V is applied. The polydisperse aerosol enters the volume between the two electrodes through a narrow slit in the outer electrode. A stream of particle free sheath air separates the aerosol from the high voltage central electrode. At the end of the

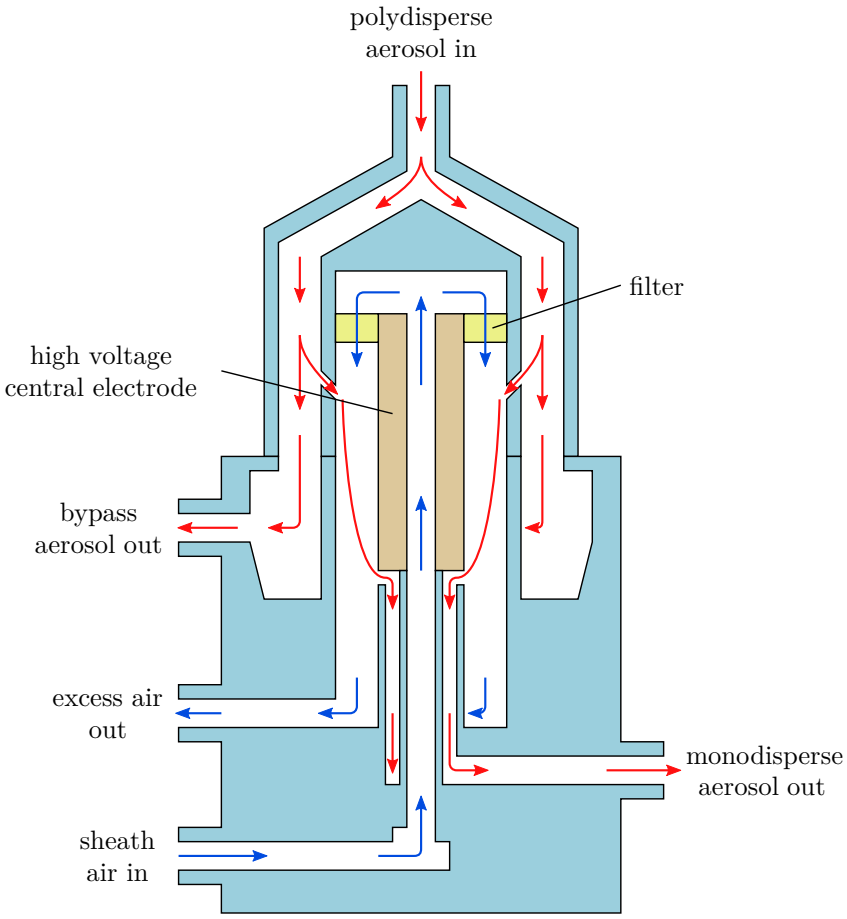

Figure 1.8: Schematic view of the Model 3085A Nano DMA. Figure adapted from TSI Incorporated (2016).

central electrode, a narrow slit allows the classified, nearly monodisperse aerosol to leave the DMA (Flagan 2011; Hinds 1999; TSI Incorporated 2016). Figure 1.8 shows a sketch of the used Nano DMA.

The electric field between the central rod and the grounded outer electrode causes oppositely charged particles to migrate towards and impact on the central electrode. The position of their impaction depends on the particle electrical mobility, the aerosol and sheath air flow rates, the applied voltage and the geometry of the DMA. Particles with high electrical mobilities impact on the part of the central electrode closest to the entrance slit, particles with lower mobility impact further downstream. Only particles within a narrow mobility range exit the DMA through a narrow slit (Flagan 2011; TSI Incorporated 2016).

The used Nano DMA has a characteristic length – the distance between the middle of the inlet slit and the middle of the outlet slit – of 4.987 cm. The outer diameter of the inner electrode and the inner diameter of the outer electrode amount to 0.937 cm and 1.905 cm, respectively. An optional bypass flow allows for higher flow rates to the DMA to avoid particle losses due to diffusion. The sheath air flow is routed through the centre of the central electrode before being turned by 180°. Afterwards, the flow is straightened by passing a Dacron screen (TSI Incorporated 2016).

To obtain particle size distributions, the voltage between the outer electrode and the central electrode is ramped and the exiting particles are detected by a CPC. Such a setup is then called a Scanning Mobility Particle Sizer (SMPS). Due to the time delay between exiting the DMA and detection in the CPC, the measured raw data must be deconvoluted before interpretation (Flagan 2011). Instead of using the classifier in SMPS mode, it can also be used to deliver a monodisperse aerosol for further experiments.

For accurate results, the charge of the aerosol particles must be known. Usually, bipolar diffusion chargers also referred to as neutralisers are employed to adjust the charge on the aerosol particles. In these devices, the surrounding gas is ionised commonly by either a radioactive source, a corona discharge or a X-ray source (Flagan 2011; TSI Incorporated 2016). By exposing the aerosol particles to large concentrations of gas ions of both polarities, the particles quickly reach a steady charge equilibrium, in which the bipolar charge distribution is known (TSI Incorporated 2016). However, the charging probability for very small particles is small, making them especially difficult to measure. Particles larger than 100 nm have a considerable chance to acquire more than one charge and particles larger than 200 nm will be present in several different charge states, making charge corrections necessary (Flagan 2011; TSI Incorporated 2016).

1.4.3 Filter sampling for offline analysis

Filter sampling for subsequent laboratory analysis is one of the most important techniques for the analysis of aerosol particles. The filter may be subjected to weighing to obtain the particle mass concentration, individual particles may be examined by various microscopic techniques or the particles may be analysed chemically or biologically (Kulkarni and Baron 2011; Hinds 1999).

In many applications, care must be taken to ensure representative sampling. Especially when sampling from a moving airstream, the size and geometry of the inlet are of importance, as well as the orientation of the sampling probe and the velocity of the

sample flow (Brockmann 2011). In some cases, the inlet also includes a preseparator such as a cyclone or an impactor to remove particles with diameters larger than a certain size (Kulkarni and Baron 2011).

The filter itself is placed in a filter holder, where it is supported on the back with a wire screen or a similar backup medium. The filter is sealed in place by the filter holder to ensure no air can bypass the filter (Raynor et al. 2011).

The choice of filter material depends on the sampling conditions and on the employed analysis method. The three main types of filters are fibre filters, membrane filters and capillary pore filters. Fibre filters consist of mats or weaves of fibres of different materials such as cellulose, glass, quartz or polymers with porosities between 60 % and 99 %. Particles are deposited in the whole volume of the filter. They provide high collection efficiencies at sufficiently low flow rates and the lowest pressure drop of the three filter types. Cellulose filters have been the standard for air sampling, but are sensitive to moisture and have relatively low filtration efficiencies for sub-micrometre particles. Glass fibre filters exhibit less moisture sensitivity and higher filtration efficiencies of greater than 99 %. Active sites on the fibres may although catalyse chemical reactions. Quartz fibre filters show low trace contamination levels and are often used for the collection of aerosol samples for subsequent chemical analysis (Raynor et al. 2011; Hinds 1999).

Membrane filters are often made from polymers such as polyvinyl chloride or Teflon. They provide high collection efficiencies at the cost of high pressure drops. The porosity generally is lower than 85 % and they provide a relatively uniform microstructure, in which particles are captured through attachment to microscopic structures on the internal surface. Membrane filters made from Teflon are often used for mass and elemental analysis due to low background values and low moisture sensitivity (Raynor et al. 2011; Hinds 1999).

Capillary pore filters consist of polymer membranes such as polycarbonates or polyesters with pores perpendicular to the filter surface. As they provide a smooth surface on which particles are deposited, they are suitable for microscopic analyses such as light and electron microscopy (Raynor et al. 2011; Hinds 1999).

The filtration of particles by fibres has been studied extensively. Therefore, the influence of flow velocity, particle size and characteristics of the filter media on the filtration efficiency is well established. Filtration theory in a first step examines the capture of particles by a single fibre. The most important mechanisms leading to

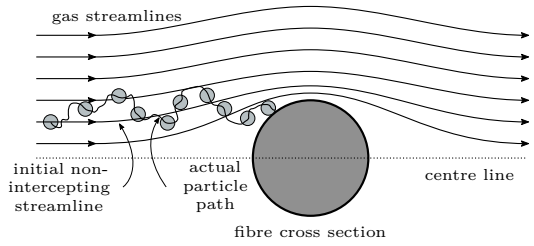

(a) Single fibre collection by diffusion.

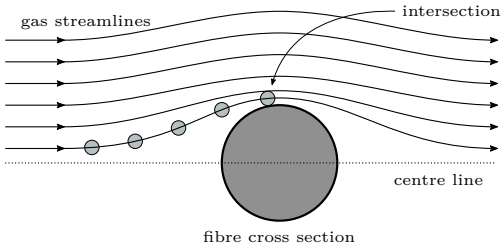

(b) Single fibre collection by interception.

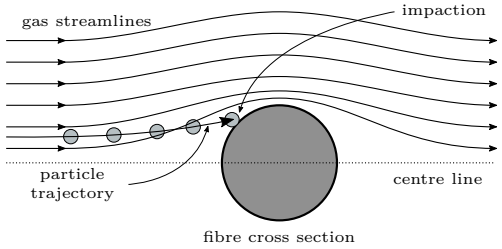

(c) Single fibre collection by impaction.

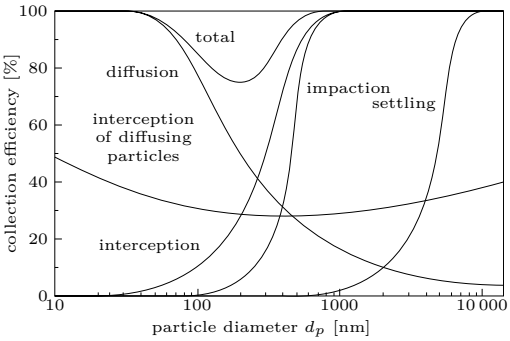

(d) Efficiency for different deposition mechanisms and total collection efficiency.

Figure 1.9: Single fibre deposition mechanisms and collection efficiency size-dependence. (a)-(c) schematically demonstrate the mechanisms diffusion, interception and impaction, respectively, leading to the deposition of aerosol particles on filter fibres. (d) shows the size-dependence of the different deposition mechanisms. Figures adapted from Hinds (1999).

the deposition of particles on a fibre are diffusion, interception and inertial impaction. Additionally, gravitation and electrostatic attraction may also come into play in some cases (Raynor et al. 2011; Hinds 1999).

Figure 1.9(a)-(c) schematically show the three main deposition mechanisms diffusion, interception and impaction. Diffusion is effective especially for small particles and is the only mechanism whose efficiency increases with decreasing particle diameter d_p. The Brownian motion of small particles increases the probability of particles, which travel on a non-intercepting streamline, to deposit on a fibre. The driving force for the diffusion towards a fibre is the concentration gradient normal to the surface of the fibre. Due to longer residence times in the vicinity of a fibre, the effect of diffusion becomes more important at lower flow rates (Hinds 1999; Raynor et al. 2011).

Particles following a streamline may still be deposited on a fibre, if the streamline brings the particle centre as close as one particle radius or less to the surface of the fibre. The mechanism, called interception, is displayed in figure 1.9(b). In contrast to diffusion and impaction, the efficiency of interception does not depend on the flow velocity. Interception is the only deposition mechanism that does not result from a particle leaving its streamline (Hinds 1999; Raynor et al. 2011).

If the inertia of a particle prevents the particle from following the abruptly changing streamlines in front of a fibre, the particle leaves its streamline and impacts on the fibre. The corresponding mechanism is called impaction and is represented in figure 1.9(c). Impaction is an important mechanism for rather large particles. Unlike diffusion, impaction benefits from increased flow rates (Hinds 1999; Raynor et al. 2011).

Electrostatic attraction may help increasing the collection efficiency. As many particles carry a charge, the use of special fibres carrying a permanent charge may increase the filtration efficiency without increasing the back pressure. Even in the absence of charged fibres, electrostatically charged particles may induce an image force on neutral fibres and therefore increase the filtration efficiency. Vice versa, electrostatically charged fibres may induce a dipole in uncharged particles, leading to increased collection efficiency (Raynor et al. 2011; Hinds 1999).

In sampling situations with low flow velocities, large particles may be influenced by gravitational settling. In vertical flows, gravitational settling may either increase or decrease the collection efficiency, depending on the direction of the flow. The impact of settling is relatively small compared to the other mechanisms and becomes even smaller in horizontal sampling flows (Raynor et al. 2011; Hinds 1999).

Figure 1.9(d) shows the contribution of the different collection mechanisms as well as the total collection efficiency as a function of particle size. Whilst collection efficiencies are close to 100 % for most particle sizes, the total collection efficiency curve shows a minimum at about 300 nm. As the efficiency of diffusional deposition decreases with increasing particle size and the efficiencies of interception and impaction decrease with decreasing particle size, several mechanisms are at work in this size regime, yet none of them is dominant (Hinds 1999; Raynor et al. 2011).

With increasing particle load on the filter, the filtration efficiency increases as particles already collected protrude into the airstream. Accordingly, also the pressure drop increases due to the increased flow restrictions. Filters may ultimately be blocked by solid particles. Droplets on the other hand do not lead to an enhanced collection efficiency.

As liquid particles are collected, they coalesce into drops and due to the obstructed flow path, the flow velocity in the filter is increased, leading to decreased filtration efficiency from diffusion (Raynor et al. 2011; Hinds 1999).

1.5 Chemical characterisation of aerosol particles

Even though measurements of particle size and concentration reveal many important information about an aerosol, the chemical nature of the aerosol remains unresolved. However, many aspects of aerosol research rely on chemical information on the aerosols in question. The chemical composition may give hints on e.g. the origin and age of an aerosol. Therefore, the chemical characterisation of aerosols is an important tool in understanding aerosol processes (Lanz et al. 2007; Johnston and Kerecman 2019; Farmer and Jimenez 2010).

1.5.1 Liquid chromatography

Chromatography is a commonly used technique for the separation of analytes. Generally, the analytes are separated due to different distribution coefficients between the mobile and stationary phase (Skoog et al. 2014; Gey 2008). The most commonly used and most versatile chromatographic method is the high-performance liquid chromatography (HPLC). Analytes are separated based on different partitioning equilibria between a liquid mobile (hence liquid chromatography) and a stationary phase (Skoog et al. 2014).

A HPLC system mainly consists of mobile phase reservoirs, a degasser, a high pressure pump, an injector unit, the HPLC column and a detector. The eluents are degassed prior to entering the chromatographic system from gases such as nitrogen and oxygen to avoid the formation of gas bubbles and subsequently flow fluctuations. The high pressure pump delivers a constant flow of mobile phase through the chromatographic system, usually at high pressures of up to several hundred bars. By employing more than one pump head, gradient elution is facilitated. A mixing chamber ensures thorough mixing of the eluents (Skoog et al. 2014; Gey 2008; Harris 2014).

In the injector, a small volume of the sample is injected into the flow of mobile phase. Many chromatographic systems employ a six-way valve to introduce the sample into the liquid flow without interruption of the flow. The sample is transported to the chromatographic column. HPLC columns usually consist of a stainless steel housing with a length between 5 cm and 25 cm and an internal diameter of 3 mm to 5 mm. Columns are filled with the stationary phase. The stationary phase usually consist of chemically modified silica gel particles of up to 5 µm in diameter. One distinguishes between normal phase (NP-HPLC) and reversed phase (RP-HPLC) separation. In

NP-HPLC, a polar stationary phase and an apolar mobile phase are used, whereas RP-HPLC employs an apolar stationary phase and a polar mobile phase. To protect the analytical column from particles, usually a precolumn is used (Skoog et al. 2014; Gey 2008; Harris 2014).

Better separation can be achieved by using columns packed with smaller particles. However, higher pressures are necessary to overcome the increased back-pressure of the column. Such systems are referred to as UHPLC (ultrahigh-pressure liquid chromatography) or UPLC (ultra performance liquid chromatography (Gross 2013; Harris 2014).

Analytes exiting the column are detected by the detector. Amongst the mostly used detectors are absorbance and fluorescence detectors as well as mass spectrometers (see section 1.5.2). The resulting chromatogram yields qualitative (retention time) and quantitative (peak height or area) information (Skoog et al. 2014; Gey 2008; Harris 2014).

1.5.2 Mass spectrometry

Mass spectrometry is a very versatile analytical technique, allowing for highly sensitive analyses at the molecular level. Consequently, mass spectrometry is the most important technique for the molecular characterisation of aerosol samples (Prather, Hatch and Grassian 2008; Farmer and Jimenez 2010; Pratt and Prather 2012a). On the one hand, mass spectrometry is used for online measurements of either the bulk aerosol phase or even single particles. Online techniques provide great time resolution, therefore allowing for the observation of quickly changing conditions. However, most instruments use hard ionisation techniques. The high degree of fragmentation makes the identification of single compounds impossible, allowing for the identification of functional groups or elemental composition at most (Farmer and Jimenez 2010; Pratt and Prather 2012b; Hoffmann, Huang and Kalberer 2011). Soft ionisation methods such as atmospheric pressure chemical ionisation (APCI) has been employed in some studies (Hoffmann et al. 1998; Kückelmann, Warscheid and Hoffmann 2000; Warscheid and Hoffmann 2001). Due to the soft ionisation, molecular ions are preserved which allows for the chemical characterisation of the examined aerosols. Zuth et al. (2018) recently reported the use of APCI-Orbitrap-MS for the online analysis of aerosols.

On the other hand, offline techniques still play an important role. Though collection of filter samples can introduce artefacts, mass spectrometric analysis of aerosol samples

– especially when coupled with separation techniques – can provide high selectivity and speciation of aerosol compounds. Therefore, individual compounds can be detected in even very low concentrations (Pratt and Prather 2012a; Farmer and Jimenez 2010). Especially the use of ultrahigh-resolution mass spectrometry (UHRMS) such as Fourier-transform ion cyclotron resonance mass spectrometry (FTICR-MS) or Orbitrap mass spectrometry allows for the measurement of the exact mass and the assignment of an unambiguous sum formula (Hu et al. 2005; Hoffmann, Huang and Kalberer 2011).

Mass spectrometers generally consist of an ion source, a vacuum system, ion transfer optics, a mass analyser and a detector. Depending on the application, ionisation may be conducted either at reduced pressures or at atmospheric conditions. Vacuum ionisation techniques include amongst others electron ionisation (EI) and chemical ionisation (CI), whereas atmospheric pressure ionisation techniques are e.g. electrospray ionisation (ESI) and atmospheric pressure chemical ionisation. Though vacuum ionisation techniques have been used for LC-MS techniques in the past, ESI and APCI have almost completely replaced them in this field (Gross 2013; Gey 2008; Hoffmann and Stroobant 2011). The ESI source will be described in more detail in section 1.5.2.1.

The ions generated in the ion source are – in case of atmospheric pressure ionisation – transferred through a vacuum interface and some ion transfer optics to the mass analyser, where they are separated according to their mass-to-charge ratio (m/z) and subsequently detected by the detector. Time-of-flight, quadrupole, ion trap, Fourier-transform ion cyclotron resonance and Orbitrap are examples for mass analysers. Whilst the first three require a separate detector, Orbitrap and FTICR employ a different detection system (Gross 2013; Gey 2008; Hesse, Meier and Zeeh 2012; Hoffmann and Stroobant 2011). The Orbitrap will be explained in more detail in section 1.5.2.2.

1.5.2.1 Electrospray ionisation (ESI)

Electrospray ionisation is one of the most popular atmospheric pressure ionisation techniques and usually the first choice for LC-MS measurements (Gross 2013; Gey 2008). The highly diluted, liquid analyte solution flows through a capillary (either metal or fused silica) which is held at a high potential of typically 3 kV to 4 kV. The high electric field strength induces a charge separation in the exiting solution and deforms the liquid at the capillary tip into a Taylor cone. Once the electrostatic forces exceed the surface tension of the liquid, a thin liquid stream is emitted from the tip of the Taylor cone

towards the counter electrode at the inlet of the mass spectrometer (Gross 2013; Gey 2008; Harris 2014; Hoffmann and Stroobant 2011).

The charge density is highest at the tip of the Taylor cone, therefore the emitted jet carries a high number of ions. After disintegration of the jet, small droplets are formed which are repelled from each other due to Coulomb repulsion. Evaporation of solvent leads to an increase in charge density at the droplets surface, until the electrostatic repulsion exceeds the surface tension at the Rayleigh limit. Even smaller droplets are emitted from the initial droplet which carry around 10 % to 18 % of the charge, but only 1 % to 2 % of the mass of the primary droplets. This process is referred to as Droplet Jet Fission (Gross 2013; Hoffmann and Stroobant 2011).

Two different models describe the further formation of gas phase ions from highly charged droplets. The charged residue model (CRM) assumes the evaporation of solvents from charged droplets containing no more than one analyte molecule to yield a fully desolvated analyte ion. In contrast, the ion evaporation model (IEM) postulates the direct evaporation of desolvated ions from the surface of highly charged micro-droplets, probably facilitated by Coulomb repulsion. It is believed nowadays that the assumptions of the CRM mechanism hold true for large molecules, while the IEM is more applicable to the description of the formation of small ions (Gross 2013).

Usually, a nitrogen stream is employed to support the nebulisation of the liquid in the ESI source. Additionally, the desolvation is promoted by either a heated nitrogen stream (curtain gas) or a heated transfer capillary (Gross 2013; Harris 2014; Hoffmann and Stroobant 2011).

1.5.2.2 The Orbitrap

The mass analyser referred to as Orbitrap was developed in the 1990s by Makarov (2000). The Orbitrap is an electrostatic ion trap, in which – unlike the quadrupole ion trap – the ions are stored without the need for a radio frequency field. The most important features of the Orbitrap mass analyser are the high resolution and high mass accuracy, as well as a high upper mass limit, a high dynamic range and a high space charge capacity (Makarov 2000; Makarov et al. 2006; Hu et al. 2005; Hoffmann and Stroobant 2011; Hesse, Meier and Zeeh 2012; Gross 2013).

The Orbitrap mass analyser consists of a barrel-shaped outer electrode and a coaxial spindle-like central electrode. The outer electrode is split in two halves along the plane of symmetry perpendicular to the z axis shown in figure 1.10. The two halves of the

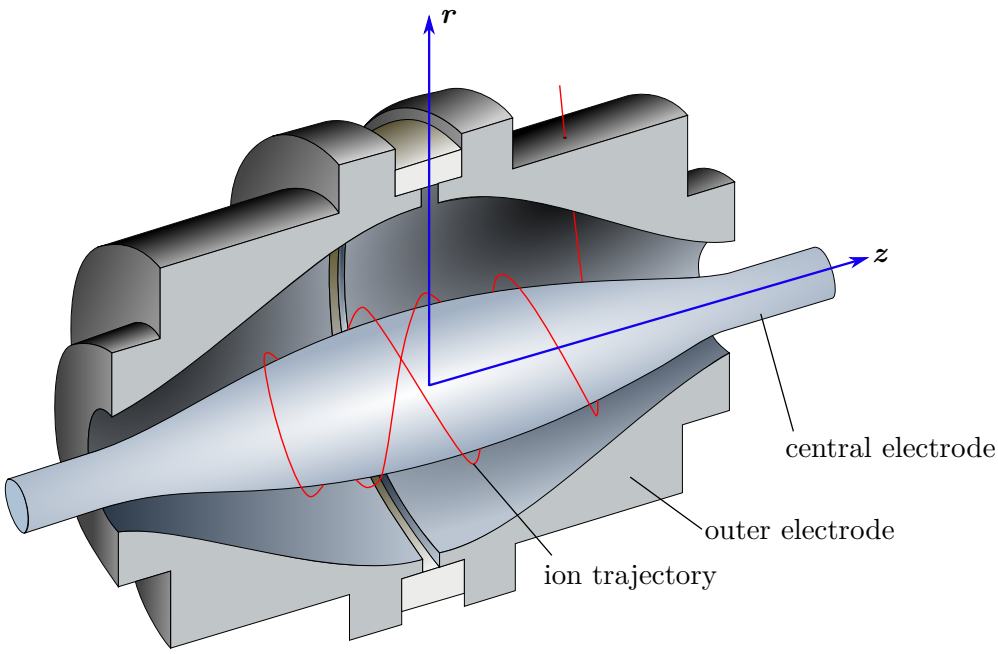

Figure 1.10: Schematic setup of the Orbitrap. Ions are introduced offset from the plane of symmetry and orbit around the central electrode on a helical trajectory. Adapted from Böckmann (2017), figure originally adapted from Makarov et al. (2006).

outer electrode are separated by an insulator. A voltage is applied between the grounded outer and the inner electrode. The polarity of the applied voltage is opposed to the polarity of the ions which are to be measured (Makarov 2000; Gross 2013; Hesse, Meier and Zeeh 2012; Hoffmann and Stroobant 2011; Hu et al. 2005).

Ions are introduced tangentially and offset from the plane of symmetry with a kinetic energy of about 1600 eV. The force resulting from the electrostatic field and the centrifugal force resulting from the motion of the ions around the central electrode forces the ions on nearly circular trajectories around the central electrode, if the potential of the central electrode is properly tuned to the kinetic energy of the ions. A field gradient is induced from the complex shape of the central electrode which causes the ions to oscillate in a harmonic axial movement along the inner electrode. Stable ion trajectories are therefore composed of a radial movement around as well as an axial movement along the central electrode. As the axial oscillation is independent of the energy and spatial spread of the ions, only the motion along the z axis is used to determine the mass spectra (Makarov 2000; Hu et al. 2005; Hoffmann and Stroobant 2011; Gross 2013).

The movement of the ions induces an image current into the split outer electrodes which is measured in the time domain. Fourier transformation yields signals in the frequency domain from which the mass spectra are calculated. As the detection is conducted in the mass analyser, no separate detector is necessary (Makarov 2000; Hoffmann and Stroobant 2011; Gross 2013).

Commonly, Orbitrap mass analysers are combined with a multipole. Furthermore, an ion trap, which is referred to as C-trap due to its shape, is used to collect and thermalise ions. This makes it possible to satisfy the high demands of the mass analyser regarding kinetic energy and energy distribution of the ions, injection time and duration, and dosing of the ions (Gross 2013).

1.6 Thesis objectives and outlines

Aerosols are important for the Earth's climate as they exert both a direct and an indirect influence on the atmosphere's radiative budget (Curtius 2006; Pöschl 2005; Seinfeld and Pandis 2006; Intergovernmental Panel on Climate Change 2013). Due to their negative radiative forcing, aerosols partially mask the effect of greenhouse gas emissions (Intergovernmental Panel on Climate Change 2021). According to the Intergovernmental Panel on Climate Change (2021), the major influence of aerosols on the Earth's climate is due to aerosol-cloud interactions. Only particles with diameters of at least 30 nm to 100 nm are able to act as CCNs (Riipinen et al. 2011). Freshly nucleated particles with diameters of only a few nanometres are exceptionally prone to scavenging by larger particles. Therefore, their growth rates determine whether they can grow fast enough to sizes at which they can act as CCNs (Riipinen et al. 2011).

Particle growth requires the formation of compounds with sufficiently low vapour pressures, which migrate to and remain in the particle (Seinfeld and Pandis 2006; George and Abbatt 2010; Riipinen et al. 2011). One possible pathway for the formation of sufficiently low-volatility compounds are oligomerisations in the particle phase (Kroll et al. 2015; Riipinen et al. 2012; Shang et al. 2016). Due to the extraordinary conditions in ultrafine particles, an entirely different chemical environment compared to coarse particles or even the bulk is likely. Therefore, chemical reactions in ultrafine particles may proceed differently to reactions in the bulk phase, leading to a potentially size-dependent chemistry in small aerosol particles.

The scope of this thesis was the investigation of particle size-dependent chemical reactions in ultrafine aerosol particles, as such reactions might play a decisive role for the growth of ultrafine particles. To examine particle size effects, suitable organic reaction systems were to be selected and the influence of particle size on these reactions was to be observed. Due to the low mass of particles in the ultrafine size-range, sensitive techniques for the chemical characterisation were required. Therefore, chapter 2 deals with the experimental setup and optimisations to the aerosol generation and analysis.

The second part of this thesis deals with the size-dependent oxidation of 1,3-diphenylisobenzofuran. The oxidation mechanism will be discussed, as well as the influence of viscosity of aerosol particles on chemical reactions. Measurements of samples generated under varying experimental conditions will be presented in a number of figures. Chapter 3 presents this aspect of the study.

In chapter 4 of this study, the size-dependence of the Diels-Alder reaction of 1,3-diphenylisobenzofuran with maleic acid was investigated. The system was chosen to mimic accretion reactions in aerosol particles, which are known to form low-volatility products in atmospheric aerosols. Again, the reaction was studied under different experimental conditions to yield insights on the particle size-dependence.

To complement the investigation of the effect of particle size on chemical reactions, the influence of Laplace pressure on the Diels-Alder reaction mentioned above was modelled numerically. The influence of surface tension, rate constants and particle size on the conversion ratio was calculated. Furthermore, an attempt was made to represent the results from chapter 4 by the model used in this study. These results will be presented and discussed in chapter 5.

2 Size-resolved chemical characterisation of ultrafine particles

2.1 Introduction

The chemical characterisation of ultrafine aerosols is always challenging due to the extremely low mass of the aerosol particles. Attempting to chemically characterise monodisperse aerosols with a very narrow size distribution like those transmitted by a DMA is even more challenging due to the huge losses of particles smaller or larger than those selected for transmission and subsequent analysis.

However, the size-resolved chemical characterisation also reveals a lot of information. Potentially important insights on e.g. the nucleation and growth of atmospheric aerosol particles may be gained, as different chemical compositions at different particle sizes of aerosols from the same source may shed a light on chemical reactions in particles. In this study, the investigation of particle size-dependent reactions in ultrafine aerosol particles was attempted.

To achieve chemical characterisation, the whole setup needs to be optimised, beginning with the aerosol generation. Furthermore, mass spectrometric detection must be as sensitive as possible and chromatographic separation is important to avoid interferences of compounds in the ion source. In this chapter, the optimised experimental procedure employed in this study will be described and taken steps in the optimisation procedure will be indicated.

2.2 Experimental methods

2.2.1 Chemicals and materials

1,3-Diphenylisobenzofuran (97 %), maleic acid (≥99 %) and 3-benzyloxycyclobutane-1,1-dicarboxylic acid were purchased from Sigma-Aldrich. Ultrapure water was produced in-house. Methanol (HPLC grade and LC-MS grade) was purchased from Fisher

Scientific and Carl Roth, respectively. Acetonitrile (LC-MS grade) and formic acid (99 % LC/MS) were purchased from VWR and water (LC-MS grade) for HPLC-MS measurements was obtained from Merck. Ammonium acetate (>99 %) was obtained from Fluka. Syringe filters (Chromafil Xtra PTFE-20/13) were purchased from Macherey-Nagel and glass fibre filters (GF/A, 37 mm) were purchased from Whatman. All chemicals were used as received without further purification.

2.2.2 Aerosol generation and chemical characterisation

Aerosols were generated using a Model 3076 Constant Output Atomizer (TSI Incorporated, Shoreview, MN). Nitrogen with 5 % (v/v) oxygen was used for the aerosol generation. The sample solutions were delivered to the generator by a dual-channel peristaltic pump and mixed immediately before entering the nebuliser. Flow rates were adjusted between 0.2 mL and 0.7 mL to ensure optimum aerosol particle number concentrations. The reactants 1,3-diphenylisobenzofuran (1,3-DPIBF) and maleic acid (MA) were used in concentrations of $6\,\mathrm{mg\,L^{-1}}$ in methanol and $20\,\mathrm{mg\,L^{-1}}$ in ultrapure water, respectively. To the solution of 1,3-DPIBF, $2\,\mathrm{mg\,L^{-1}}$ of 3-benzyloxycyclobutane-1,1-dicarboxylic acid (BCDA) were added as an internal standard. Additionally, one set of experiments was executed with the addition of $40\,\mathrm{mg\,L^{-1}}$ glycerol to both solutions to investigate the plasticising effect of glycerol. Further experiments were conducted with methanolic solutions of maleic acid with added glycerol concentrations of $40\,\mathrm{mg\,L^{-1}}$ and $80\,\mathrm{mg\,L^{-1}}$.

Besides aerosol generation with the Constant Output Atomizer, also the use of an Advanced Electrospray Aerosol Generator Model 3482 (TSI Incorporated, Shoreview, MN) has been investigated. Samples were delivered by a dual-channel syringe pump at flow rates from $5\,\mathrm{\mu L\,min^{-1}}$ to $20\,\mathrm{\mu L\,min^{-1}}$. The Electrospray Aerosol Generator (EAG) has been operated both with and without a buffer. Settings were separately optimised for aerosol concentrations at different particle diameters.

After the nebulisation, the aerosol was subsequently dried by an activated charcoal denuder before entering a flow tube reactor. The flow tube reactor had a volume of 11.8 L and flow rates through the reactor were $1.01\,\mathrm{L\,min^{-1}}$ and $1.41\,\mathrm{L\,min^{-1}}$, corresponding to plug flow residence times of 11.7 min and 8.4 min, respectively. Reynolds numbers[1] at a flow rate of $1.01\,\mathrm{L\,min^{-1}}$ of 13.3 and of 18.6 at a flow rate of $1.41\,\mathrm{L\,min^{-1}}$ clearly suggest laminar flow in the flow tube reactor. The flow tube was held at at-

1. Calculations in section A.1 on page 97

mospheric pressure via a filtered pressure relief between the aerosol generator and the activated charcoal denuder. The setup is displayed in figure 3.1.

Electrically conductive tubing was used for all aerosol flows to avoid excessive losses of charged aerosol particles due to electrostatic fields and tubing was kept as short as possible. The aerosol was size-classified by an Electrostatic Classifier Model 3082 equipped with an Advanced Aerosol Neutraliser Model 3088 and a Nano-DMA (TSI Incorporated, Shoreview, MN). The monodisperse aerosol flow was split. Aerosol concentrations were measured using a Water-based Condensation Particle Counter Model 3789 (TSI Incorporated, Shoreview, MN) operating in the 2 nm-mode. In parallel, filter samples were collected for about 48 h each to ensure sufficient particle mass for subsequent chemical analysis and to avoid bias due to different sampling times. Filter samples were stored in sealed Petri dishes at −28 °C until extraction.

Chemical analysis

For chemical analysis, filters were cut and extracted with 3 mL of a mixture of methanol and acetonitrile (1:1 (v/v)) for 30 min on an orbital shaker. The solutions were filtered through a syringe filter and the solvents were evaporated at 35 °C under a gentle nitrogen stream. The extraction procedure was repeated twice with solvent volumes of 1.0 mL. The combined extracts were dissolved in 0.5 mL of a 9:1 (v/v) mixture of water and acetonitrile and filtered through a syringe filter.

LC-MS measurements were conducted on an UltiMate 3000 UHPLC system (Dionex, Thermo Fisher Scientific, Bremen, Germany) equipped with a Hypersil Gold C18 column (50 mm × 2 mm, 1.9 µm, Thermo Fisher Scientific, Bremen, Germany). The LC system was connected to a Q-Exactive Orbitrap mass spectrometer equipped with a heated ESI source (Thermo Fisher Scientific, Bremen, Germany).

A method was developed to separate and detect the analytes of interest. The chromatographic flow rate was set to 0.5 mL min^{-1}. Eluent A was water containing 2 % acetonitrile and 0.04 % formic acid and eluent B was acetonitrile containing 2 % water. Gradient elution was employed to separate the analytes. Before the start of each measurement, the column was equilibrated for two minutes at 0 % eluent B. After the injection, isocratic elution at 0 % B for one minute was followed by a gradual increase in B to 50 % at four minutes and 95 % at six minutes. The eluent composition was held at 95 % B until minute nine, before the fraction of B was gradually reduced to 0 % at minute 9.5 and held until the end of the measurement.

To obtain the lowest possible limits of detection, the mass spectrometric parameters were optimised for measurements in the positive and negative mode separately. The mass spectrometer was calibrated on a daily basis to ensure appropriate mass accuracy.

2.2.3 Data evaluation

XCalibur 2.2 (Thermo Fisher Scientific, Bremen, Germany) was used to identify the compounds of interest and to integrate the mass spectra. Background subtraction was performed in MS Excel, as were further calculations.

Particle concentration data were imported by the Aerosol Instrument Manager software (TSI Incorporated, Shoreview, MN) and exported as comma-separated values files. Matlab R2020a (Mathworks Incorporated, Natick, MA) was used to import and plot time resolved particle concentrations and to calculate the filter loading (see section A.2.1 and A.2.2 for Matlab code).

As will be described in section 3.3, 3-benzyloxycyclobutane-1,1-dicarboxylic acid (BCDA) was used as an internal standard to facilitate data interpretation. The mass spectrometric signal of BCDA correlates well with the particle mass deposited on the filter. Therefore, the comparison of the peak areas of the compounds of interest with the peak area of the internal standard allows for the comparison of filter samples with varying amounts of particle mass. Additionally, the impact of changes in sensitivity of the mass spectrometer is reduced and therefore the comparison of different sets of filter samples enhanced.

To compare filter samples obtained for e.g. different particle diameters, the corresponding peak areas were divided by the peak area of the internal standard to yield the relative peak area (RPA). Subscripts may be used to indicate the relative peak area for a sample of a given particle size, e.g. $RPA_{20\,\mathrm{nm}}$ refers to the relative peak area of a filter sample of a monodisperse aerosol with a particle diameter of 20 nm.

2.3 Results and Discussion

2.3.1 Aerosol generation

Samples were delivered to the Electrospray Aerosol Generator by a syringe pump. To avoid reactions of the reactants prior to aerosol generation, a method for sample delivery by two separate syringes in a dual-channel syringe pump was developed. The

sample flow from the two syringes was combined in a Tee connector approximately 7 cm downstream of the syringes and the combined flow was delivered to the EAG.

The Electrospray Aerosol Generator is usually operated with ammonium acetate buffers, in which the solutes are dissolved (TSI Incorporated 2014). The buffer remains at least partially in the generated particles. To avoid complications from the added buffer, the generation of aerosols without buffer was investigated. Solvents typically used in LC-ESI-MS were examined for their operationality in EAG sample delivery, however electrical conductivity appeared to be too low in most cases (isopropyl alcohol/methanol (1:1), water/acetonitrile (1:1), water/acetonitrile (9:1), water/methanol (1:1), water:methanol (9:1)). By mixing methanol with formic acid, the electrical conductivity became high enough to provide a stable spray. The operation was further improved by the addition of water with a seemingly ideal solvent composition of 89 % methanol, 10 % ultrapure water and 1 % formic acid.

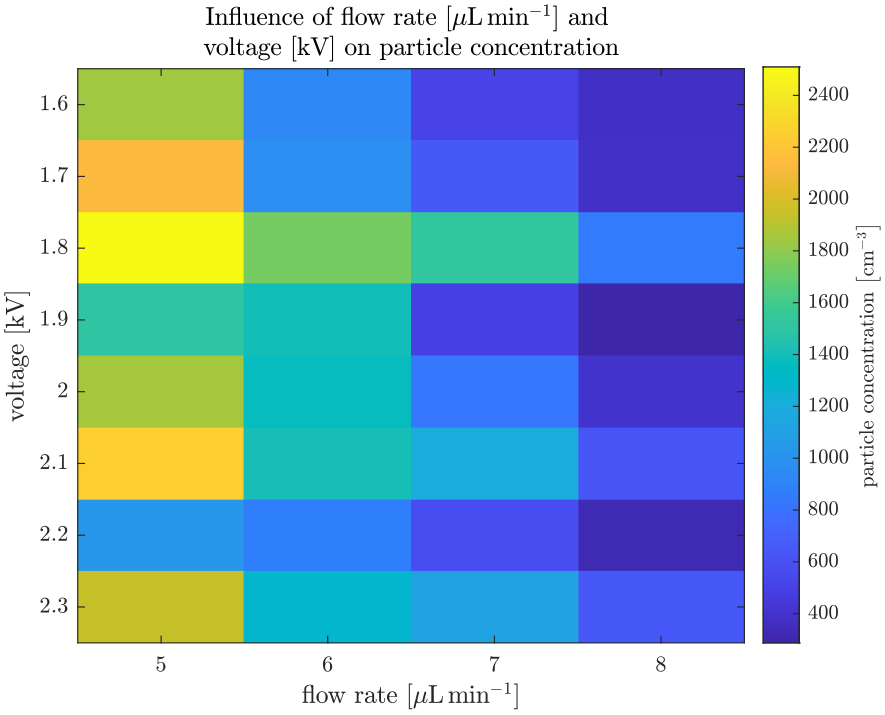

Figure 2.1: Optimisation of EAG parameters for particles with a diameter of 20 nm. The particle concentration is plotted against the flow rate and the voltage.

The flow rates and voltages were varied to obtain the highest possible particle concentrations at a given particle diameter. CPC data were imported and evaluated using

the Matlab scripts given in sections A.2.3 and A.2.4. Figure 2.1 shows the results of the optimisation for particles with a diameter of 20 nm. Apparently, the highest concentrations of particles with diameters of 20 nm were obtained with relatively low flow rates of 5 µL min^{-1}. Lower flow rates lead to an unstable spray and were therefore not included in the optimisation. Intermediate voltages of 1.8 kV lead to the highest concentration of monodisperse aerosol particles on the order of 2400 cm^{-3}. However, fluctuations in the aerosol particle concentration with varying voltage appeared arbitrary. Furthermore, repetition of the experiments (graphical representation of the results displayed in figure A.1 on page 115) yielded entirely different parameters for which the highest aerosol concentrations were achieved. Therefore, the reproducibility unfortunately was low and the buffer free aerosol generation with the EAG did not seem to be a viable route to produce aerosols for this study.

Though the EAG is designed for the generation of aerosol particles between 2.5 nm and 150 nm in diameter (TSI Incorporated 2014), the use without a buffer impairs its performance. Though primarily designed for the generation of larger particles between 20 nm and 300 nm in diameter (TSI Incorporated 2005), better results were obtained with the Constant Output Aerosol Generator.

As described in section 2.2.2, the solutions were delivered to the nebuliser by a dual-channel peristaltic pump in order to avoid reactions in the solution prior to nebulisation. The concentrations of the nebulisation solutions were chosen to yield the highest particle concentrations in the size range of interest. An excess of maleic acid was used to shift the equilibrium towards the products. The combined flow rate was varied to optimise the aerosol particle concentration at a given particle size prior to each experiment. The flow rates of the diene solution and the dienophile solution were kept equal to avoid different particle compositions.

Fluctuations in the aerosol particle concentration occurred but were mainly due to pressure fluctuations of the nebulising gas. Number concentrations usually were on the order of 800 cm^{-3}, 4500 cm^{-3} and 5000 cm^{-3} for monodisperse aerosols with particles of 20 nm, 50 nm and 80 nm in diameter, respectively.

2.3.2 Optimisation of the MS parameters

The MS parameters were optimised separately for measurements in the positive and negative ion mode. Optimisation was performed by injecting standards in the LC

system and separating the compounds on the chromatographic column. Table 2.1 gives the selected parameters for negative and positive mode.

Table 2.1: MS settings for the analysis in the positive and negative mode.

parameter	setting in the positive mode	setting in the negative mode
Scan parameters		
Scan type	Full MS	Full MS
Scan range	53.4 to 800 m/z	50 to 750 m/z
Fragmentation	None	None
Resolution	140 000	140 000
Microscans	1	1
Lock masses	off	112.985 63
AGC target	1×10^6	1×10^6
Maximum inject time	50	50
HESI source		
Sheath gas flow rate	30	40
Aux gas flow rate	10	10
Sweep gas flow rate	2	10
Spray voltage (|kV|)	5.00	5.00
Capillary temperature (°C)	350	350
S-lens RF level	50.0	50.0
Aux gas heater temperature (°C)	350	300

In contrast to optimisation via direct infusion of standards, no interferences between different compounds in the ion source are to be expected and the solvent composition matches the composition during the actual measurements.

The position of the ion source relative to the inlet of the mass spectrometer was optimised in the same way. The HESI source was moved as far out the Ion Max housing as possible (position D) and as far to the right as possible (-1). The front-to-back position was set to 1.5.

Maleic acid, BCDA and 1,4-diphenyl-1,2,3,4-tetrahydro-1,4-epoxido-naphthalene-2,3-dicarboxylic acid (DTEND) were detected as $[M-H]^-$ at m/z 115.0037, m/z 249.0774 and m/z 385.1081, respectively. 1,3-DPIBF was detected as both M^+ and $[M+H]^+$ at m/z 270.1039 and m/z 271.1117 with similar intensities. 1,2-dibenzoylbenzene was detected as $[M+H]^+$ at m/z 287.1067.

2.3.3 Optimisation of the LC method

Standards were injected and the gradient was adjusted to yield good separation and short analysis times. Separation was achieved by using gradient elution with the conditions given in section 2.2.2. The retention times were 0.37 min for maleic acid, 3.49 min for BCDA, 4.73 min for DTEND, 4.93 min for 1,2-dibenzoylbenzene and 6.14 min for 1,3-DPIBF. As compounds that were detected in the negative mode eluted during the first part of the run, followed by those which were detected in the positive mode, polarity and mass spectrometric parameters were switched during the analysis to allow for the measurement in positive and negative mode during one chromatographic run.

2.3.4 Utilisation of an internal standard for the evaluation of LC-MS measurements

3-Benzyloxycyclobutane-1,1-dicarboxylic acid (BCDA) was added as an internal standard to the nebulisation solution of 1,3-DPIBF. The internal standard was chosen as it is easily detectable with ESI in the negative mode and as it was not expected to interfere with the examined reactions. Furthermore, it is – like 1,3-DPIBF – essentially non-volatile and its concentration therefore not expected to be influenced by evaporation.

As not all filters could be sampled with the exact same amount of particle mass, this had to be accounted for. One possibility would be to divide the concentrations or peak areas of the compounds of interest by the calculated deposited particle mass. However, this procedure leads to bias once the composition of the aerosol particles is changed, as for example by the addition of glycerol.

Therefore, the exploitation of an internal standard is a necessary measure to compare filter samples loaded with different amounts of aerosol particles. Dividing the peak area of the compound of interest by the peak area of BCDA, the relative peak area *RPA* is obtained. As the ratio of BCDA to 1,3-DPIBF and MA in the nebulising solutions is constant, the change in composition of the aerosol particles is compensated. Furthermore, changes in sensitivity of the mass spectrometer are accounted for, as long as they affect all m/z ratios equally.

2.4 Conclusion

The extremly low particle mass of ultrafine particles poses difficulties for their size-resolved chemical characterisation. Therefore, optimisation of the experimental setup is

critical. An important part is the generation of sufficiently high number concentrations of particles of a certain size. The Electrospray Aerosol Generator therefore is a natural choice in terms of aerosol generation. Whilst it was possible to ensure the sample delivery with two separate syringes, running the EAG without the use of a buffer severely impairs its performance and most of all the repeatability. Therefore, a Constant Output Aerosol Generator had to be used. The supply of nebulisation solutions was handled by a dual-channel peristaltic pump and the total flow rate was adjusted to yield optimal generation conditions.

Aerosol particles were sampled on filters to accumulate the particle phase over a time span of approximately 48 h. Filter samples were extracted and measurements were conducted after optimisation of the LC method and the MS parameters. An internal standard was employed to facilitate the evaluation of the LC-MS measurements.

The aerosol generation leaves room for further optimisations. Developing a solvent mixture which allows for the buffer-free aerosol generation with the EAG might help to exploit the potential of this aerosol generator. Increased particle concentrations may be expected compared to the Constant Output Aerosol Generator, therefore the sampling times necessary to accumulate sufficient particle mass may be decreased.

Furthermore, other means of particle collection could further enhance the particle size-dependent chemical characterisation. Micro-Orifice Uniform Deposition Impactors (MOUDI) facilitate the sampling of several particle size-ranges in parallel. Modern devices collect particles as small as 10 nm, making them interesting for this research. However, the cut points of commercially available instruments are spaced too far apart to allow for the proper investigation of the impact of size on aerosol chemistry, a custom-built device would therefore be necessary.

Zuth et al. (2018) achieved very low limits of detection by measuring aerosol particles in an Online-Orbitrap setup. A similar setup might also be interesting for the analysis of size-classified aerosols. If necessary, limits of detection might be further improved by a setup similar to the FIGAERO described by Lopez-Hilfiker et al. (2014).

3 Size-dependent oxidation reactions in organic aerosol particles

This chapter is a reprint of the manuscript

Size-dependent oxidation reactions in organic aerosol particles

Maximilian Böckmann, Thorsten Hoffmann

in preparation for Atmospheric Chemistry and Physics

Abstract Various mechanisms are discussed for the formation of low vapour pressure organic compounds in the atmosphere. Low-volatile organic compounds are of central importance, especially for the formation of new particles and the early growth of newly formed particles. Possible pathways include oxidation of volatile organic compounds (VOCs) in the gas phase, heterogeneous oxidations at the particle surface, formation of organic salts and oligomerisation reactions. Here we report on the observation of particle size-dependent heterogeneous oxidation of a model organic system. The results are based on UHPLC-ESI-HRMS measurements of filter samples of monodisperse aerosols. Solutions of 1,3-diphenylisobenzofuran and maleic acid were nebulised and the resulting aerosol was size classified using an electrostatic classifier to obtain a monodisperse aerosol. Particle sizes of 20 nm, 50 nm and 80 nm were selected for this study. The aerosol was sampled on filters, which were then extracted. The extracts were measured using an ultra-high performance liquid chromatography system coupled to an Orbitrap mass spectrometer via an electrospray ionisation source. Our results show a strong preference for the oxidation of 1,3-diphenylisobenzofuran in smaller particles, far beyond what would be expected based on different surface-area-to-volume ratios alone. Such size-dependent chemical reactions could be important for the growth of freshly formed particles to sizes at which they can act as cloud condensation nuclei (CCNs).

3.1 Introduction

Aerosols have a significant impact on human health and the Earth's climate (Kolb and Worsnop 2012; Pöschl 2005; Schulz et al. 2005; Seinfeld and Pandis 2006; Curtius 2006). Particularly small particles are capable of penetrating deep into the lungs and can cause allergic reactions, respiratory and cardiovascular diseases (Pöschl 2005; Kolb and Worsnop 2012; Schulz et al. 2005). According to the World Health Organization, there were 348,000 deaths attributable to exposure to aerosol particles in the European Union in 2000 (World Health Organization 2006). In addition to health effects, aerosols have a net negative radiative forcing and thus (in the vast majority of cases) cool the atmosphere (Seinfeld and Pandis 2006; Pöschl 2005; Kolb and Worsnop 2012; Intergovernmental Panel on Climate Change 2014). While particle interactions with radiation, such as reflection and scattering, have a direct effect on the radiation budget, the ability of aerosol particles to serve as cloud condensation nuclei is referred to as an indirect effect (Pöschl 2005; Kolb and Worsnop 2012; Curtius 2006; Seinfeld and Pandis 2006). To better understand the effects of aerosols on climate and human health, it is import-

ant to know how they are formed, how they grow, and what they are made of. In this regard, organic components make up a very large portion of the atmospheric particulate phase (Jimenez et al. 2009; Zhang et al. 2007; Curtius 2006). Since the growth rates of fine particles in the size range of 2 to 20 nm are much larger than can be explained by the condensation of sulfuric acid alone, low-volatile organics are also considered the most likely contributor in the growth of fine atmospheric particles (Riipinen et al. 2011; Pierce et al. 2011).

Sufficiently low vapour pressures are required for molecules to be able to transfer from the gas phase to the particle phase or to remain there (Seinfeld and Pandis 2006; Riipinen et al. 2011; George and Abbatt 2010). Several pathways for the formation of compounds with particularly low vapor pressures are discussed: direct formation through gas-phase oxidations of volatile organic compounds where, in particular, rapid auto-oxidation steps are responsible for the incorporation of multiple oxygen functionalities, heterogeneous oxidations at the particle surface, the formation of organic salts in the particle phase, and the formation of higher molecular weight compounds through condensation and oligomerization reactions in the particle phase (Riipinen et al. 2012; Shang et al. 2016; Kolb and Worsnop 2012; Kroll et al. 2015). Newly formed aerosol particles must grow to a size of at least 30 nm in diameter to act as CCNs (Riipinen et al. 2011; Riipinen et al. 2012). Ultrafine particles, however, are susceptible to uptake by larger particles (coagulation), so their growth rate is critical for their fate (Riipinen et al. 2011). Preferential formation of compounds with sufficiently low vapour pressure especially in smaller particles could increase the growth rate of small particles compared to larger particles, making their survival more likely. This could ultimately affect the number of CCNs and thus cloud properties (Riipinen et al. 2011; Riipinen et al. 2012; Seinfeld and Pandis 2006).

Here we report observations of a particle size-dependent chemical response in a model system. Our results indicate a strong preference for oxidation of 1,3-diphenylisobenzofuran in small particles over larger particles. Assuming that size-dependent reactions also occur in the atmosphere, they could have a major impact on particle growth, making the survival of small particles more likely.

3.2 Methods and materials

3.2.1 Materials

1,3 Diphenylisobenzofuran (97 %), maleic acid (≥99 %) and 3-benzyloxycyclobutane-1,1-dicarboxylic acid were purchased from Sigma-Aldrich. Ultrapure water was prepared in-house. Methanol (HPLC grade and LC-MS grade) was purchased from Fisher Scientific and Carl Roth, respectively. Acetonitrile (LC-MS grade) and formic acid (99 % LC/MS) were purchased from VWR and water (LC-MS grade) for HPLC-MS measurements was obtained from Merck. Syringe filters (Chromafil Xtra PTFE-20/13) were purchased from Macherey-Nagel and glass fibre filters (GF/A, 37 mm) were purchased from Whatman. All chemicals were used as supplied without further purification.

3.2.2 Aerosol generation

Aerosols were generated with a Constant Output Generator Model 3076 (TSI Incorporated, Shoreview, MN). In our study, both compressed air and a mix of nitrogen (95 % (v/v)) and oxygen were used for aerosol generation. Gases were filtered through a hydrocarbon trap prior to nebulisation. The pressure was set to 2.2 bar corresponding to a volumetric flow of approximately $3\,\mathrm{L\,min^{-1}}$. The solution containing the organic model substances was nebulised from two individual solutions which were separately delivered by a dual-channel peristaltic pump and mixed immediately before entering the nebuliser.

Since the present study was designed to be part of a series of experiments on particle size-dependent bond-forming reactions, the second solution contained maleic acid as a reagent of a Diels-Alder reaction. The composition of the solutions is shown in table 3.1. For one series of experiments, glycerol was added to both solutions at a concentration of $40\,\mathrm{mg\,L^{-1}}$ to investigate possible plasticizing effects.

The flow rates of the liquids were adjusted in the range of 0.2 mL to 0.7 mL to optimise the concentration of aerosol particles at a given particle size. The generated aerosol was dried using an activated charcoal denuder before passing a flow-tube reactor with a volume of 11.8 L under dark conditions. The flow rate through the flow-tube reactor was adjusted to $1.01\,\mathrm{L\,min^{-1}}$, corresponding to a plug flow residence time of 11.7 min. The flow through the reactor was laminar, as suggested by Reynolds numbers of 14.2 and 16.1 for air and nitrogen, respectively. A series of experiments was also performed at a higher flow rate of $1.41\,\mathrm{L\,min^{-1}}$, corresponding to a residence time of

Table 3.1: Composition of solutions for aerosol generation.

	solution 1	**solution 2**
reagent	1,3-diphenylisobenzofuran ($6\,\mathrm{mg\,L^{-1}}$)	maleic acid ($20\,\mathrm{mg\,L^{-1}}$)
internal standard	3-benzyloxycyclobutane-1,1-dicarboxylic acid ($2\,\mathrm{mg\,L^{-1}}$)	–
solvent	methanol (HPLC grade)	ultrapure water

8.4 min. The pressure within the flow-tube reactor was maintained at atmospheric levels via filtered pressure relief between the aerosol generator and the denuder. Figure 3.1 shows schematically the setup used.

3.2.3 Sample collection setup

After passing the flow-tube reactor, aerosol particles were size-classified using an Electrostatic Classifier Model 3082 (TSI Incorporated, Shoreview, MN) equipped with a Nano-DMA. The flow was split behind the DMA. Particle concentrations were measured using a Model 3789 Water-based Condensation Particle Counter (TSI Incorporated, Shoreview, MN) and filter samples were collected for subsequent chemical analysis. Filter samples were collected for approximately 48 hours each to ensure sufficient mass for chemical analysis and to eliminate bias due to varying sampling times.

3.2.4 Chemical Analysis

For chemical analysis, the filters were cut and extracted for 30 min on an orbital shaker with 3 mL acetonitrile-methanol (1:1). The extracts were filtered through a syringe filter and the solvents were evaporated under a gentle nitrogen stream at 35 °C. The extraction process was repeated twice with a solvent volume of 1 mL each time. After evaporation, the samples were dissolved in an acetonitrile-water mixture (1:9). Measurements were performed using a UHPLC system (Thermo Fisher Scientific, Waltham, MA) equipped with a Hypersil Gold C18 column (Thermo Fisher Scientific, 50 mm × 2.1 mm, 1.9 µm). A Q-Exactive Orbitrap mass spectrometer (Thermo Fisher Scientific, Waltham, MA) with a HESI source was used for detection.

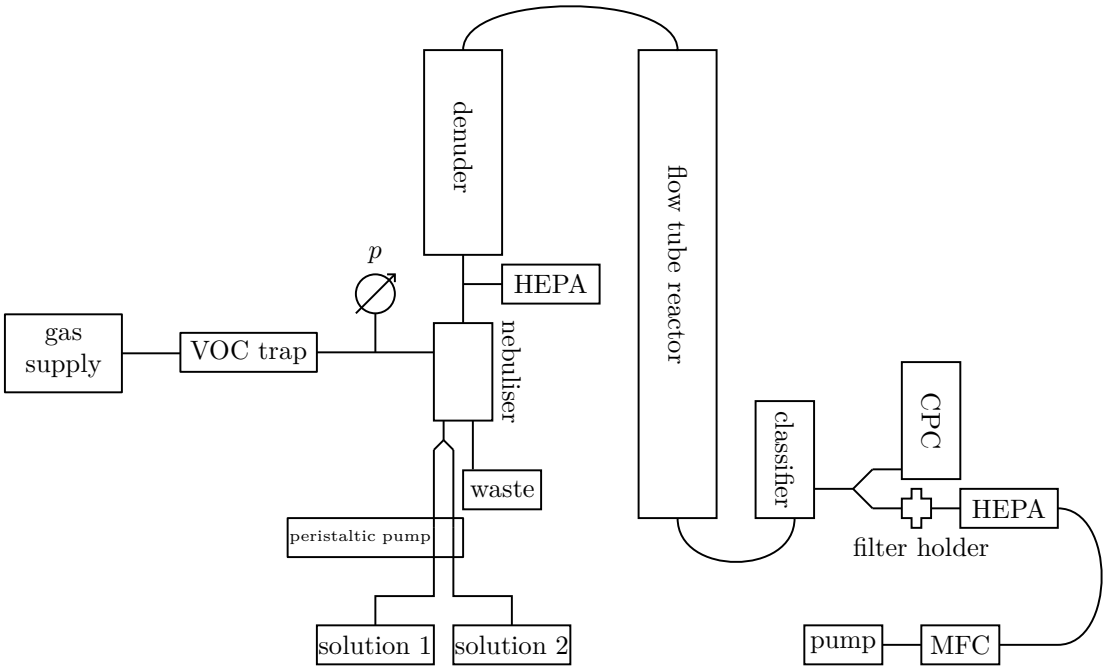

Figure 3.1: Experimental setup for the collection of filter samples. After nebulisation, aerosols are dried and pass the flow tube reactor. Afterwards, aerosols are size-classified and the monodisperse aerosol flow is split. Aerosol concentrations are measured by a WCPC and particles are sampled on a filter for subsequent chemical analysis.

A method for separation and quantification of the analytes of interest was developed. The eluents used for chromatographic separation were water with 0.04 % formic acid and 2 % acetonitrile (eluent A) and acetonitrile with 2 % water (eluent B). The flow rate was set at $0.5\,\mathrm{mL\,min^{-1}}$. Each chromatographic run was preceded by a 2-minute column equilibration with 0 % eluent B. The gradient was chosen as follows: Starting with an isocratic elution at 0 % B for one minute, B was gradually increased to 50 % after four minutes and 95 % after six minutes. The eluent composition was then held at 95 % until minute nine where it was decreased to 0 % B until minute 9.5 , at which the composition was kept until the end of the measurement at eleven minutes. Measurements were conducted in both negative and positive mode. Mass calibration was performed on the mass spectrometer daily to ensure accurate measurements.

3.3 Results and discussion

3.3.1 Mechanism of the oxidation of 1,3-diphenylisobenzofuran

1,3-Diphenylisobenzofuran is used as a trapping agent for singlet oxygen ($^1O_2$) and the superoxide radical anion ($O_2^{\bullet -}$) (Zhang and Li 2011; Gomes, Fernandes and Lima 2005; Lala, Rabek and Ranby 1980). The oxidation mechanism is assumed to proceed through the addition of singlet oxygen to form a secondary ozonide, followed by the fission of the oxygen-oxygen bond to yield 1,2-dibenzoylbenzene (Zhang and Li 2011). Furthermore, the degradation of 1,3-diphenylisobenzofuran in halogenated solvents in the absence of singlet oxygen is described by Zhang and Li (2011). Lala, Rabek and Ranby (1980) propose a radical mechanism, in which radicals are formed through an intersystem crossing of 1,3-diphenylisobenzofuran to a triplet state, followed by the addition of oxygen to form an ozonide. Photolysis of the oxygen-oxygen bond then yields a biradical, which can form 1,2-dibenzoylbenzene or undergo a rearrangement to finally form 2-benzoylphenyl benzoate. Figure 3.2 shows the reaction scheme of the oxidation of 1,3-diphenylisobenzofuran to 1,2-dibenzoylbenzene via a secondary ozonide.

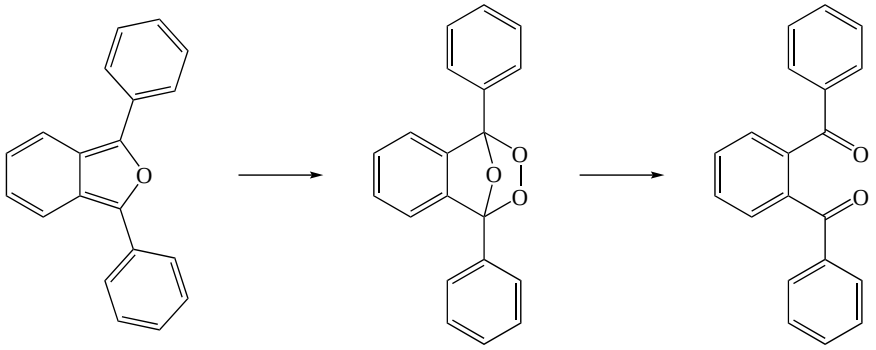

1,3-diphenylisobenzofuran secondary ozonide 1,2-dibenzoylbenzene

Figure 3.2: The figure shows the reaction scheme for the oxidation of 1,3-diphenylisobenzofuran to 1,2-dibenzoylbenzene via a secondary ozonide.

The reaction was carried out under dark conditions. However, due to the size of the experimental setup, absolute darkness could not be guaranteed. Nevertheless, photochemical reactions are considered unlikely due to the general avoidance of light. However, the effect of curvature could possibly play a role in facilitating the oxidation reaction. On

small scales, such as in ultrafine aerosol particles, the surface energy could be altered by curvature and therefore possibly lead to different reaction pathways than would be expected in bulk reactions. Such an effect was observed, for example, by Fang, Li and Feng (2017) upon the investigation of oxidation reactions on highly curved metallic and crystal surfaces. Similarly, Kou et al. (2007) observed curvature dependent oxidation reactions on gold nanoparticles.

In this context, it is worth noting that even within electrospray ionization sources, certain reactions are accelerated that occur very slowly in the bulk phase (Bain, Pulliam and Cooks 2015; Müller, Badu-Tawiah and Cooks 2012; Banerjee et al. 2017). In these systems, the high electric field strengths as well as the high charge density at the ESI droplet surface are usually considered as the main drivers for the reaction acceleration. However, by comparing reaction rates in bulk solution and in Leidenfrost droplets, Bain et al. (2016) have shown that interfacial effects play an important role in accelerating reactions in small droplets. Therefore, interfacial effects and radius of curvature could also be important for heterogeneous oxidation reactions in ESI droplets and in ultrafine particles, providing an explanation for the observations described.

3.3.2 Viscosity of ultrafine aerosol particles

Several publications have addressed the phase state of (secondary) organic aerosols. Zobrist et al. (2008) first proposed the formation of glasses in atmospheric aerosol. Virtanen et al. (2010) concluded from the bounce behaviour of aerosol particles in an electrical low pressure impactor and from scanning electron microscope images of SOA particles that particles smaller than 30 nm behave like viscous liquids, while particles with diameters of more than 30 nm show a more solid behaviour. For particles up to 17 nm in diameter, the bounce was further reduced, indicating viscous fluid properties (Virtanen et al. 2011). The differences in viscosity were attributed, at least in part, to the different chemical composition of the aerosol particles studied, as the smaller particles were less oxidized (Virtanen et al. 2011). Cheng et al. (2015) reported size-dependent phase transitions in aerosol nanoparticles. According to them, particles with the same chemical composition can coexist in different phase states depending solely on their diameter.

According to the equation of Young and Laplace, relatively high pressure differences are expected across the highly curved surface of small aerosol particles (Adamson and Gast 1997; Butt, Graf and Kappl 2003; Gennes, Brochard-Wyart and Quéré 2009). The

pressure difference depends on the surface tension and radii of curvature of the droplets (Adamson and Gast 1997; Butt, Graf and Kappl 2003). However, pressure also has an effect on viscosity. Both an increase of viscosity with pressure (Wonham 1967; Griest, Webb and Schiessler 1958) and a decrease in viscosity with increasing pressure have been reported, e.g. for water and some glasses (Schmelzer, Zanotto and Fokin 2005).

For most organic substances, there is a positive correlation of pressure and viscosity (Griest, Webb and Schiessler 1958; Dow, Fenske and Morgan 1937). However, the pressure range investigated in many studies far exceeds the pressures expected in aerosol particles; moreover, the substances investigated in such studies are rarely important in atmospheric aerosol research. For hydrocarbons, Griest, Webb and Schiessler (1958) reported an increase in viscosity of about a factor of two when the pressure was increased from atmospheric to several hundred bar. For aerosol particles, much lower pressures are expected, so that no large effect of pressure on the viscosity of aerosol particles is to be expected.

3.3.3 Verification of the performance of the internal standard

The chemical analysis of aerosol particles is always challenging, especially when the aerosol particles are classified by size before filter sampling, resulting in an extremely low mass of particles deposited on the collection medium. To simplify the interpretation of the measured data, 3-benzyloxycyclobutane-1,1-dicarboxylic acid (BCDA) was added as an internal standard to the methanolic solution of 1,3-diphenylisobenzofuran. The internal standard was chosen because it is not expected to interfere with the reactions under investigation and because it is readily detectable by ESI-MS.

As Fig. 3.3 shows, plotting the peak area of the internal standard against the total mass of deposited particles gives an excellent linear correlation. Therefore, comparing the peak areas of the compounds of interest with the peak area of the internal standard allows for the comparison of filter samples with different amounts of particles, which is particularly critical when comparing different particle sizes. It also minimizes the effects of changes in mass spectrometer sensitivity to improve the comparability of different sets of filter samples. The peak areas of the analytes were divided by the peak area for BCDA to obtain the relative peak areas (RPA).

To compare the influence of particle size, the ratios of relative peak areas were calculated. The peak area ratios (PAR) for particles with diameter d were calculated as in Eq. 3.1.

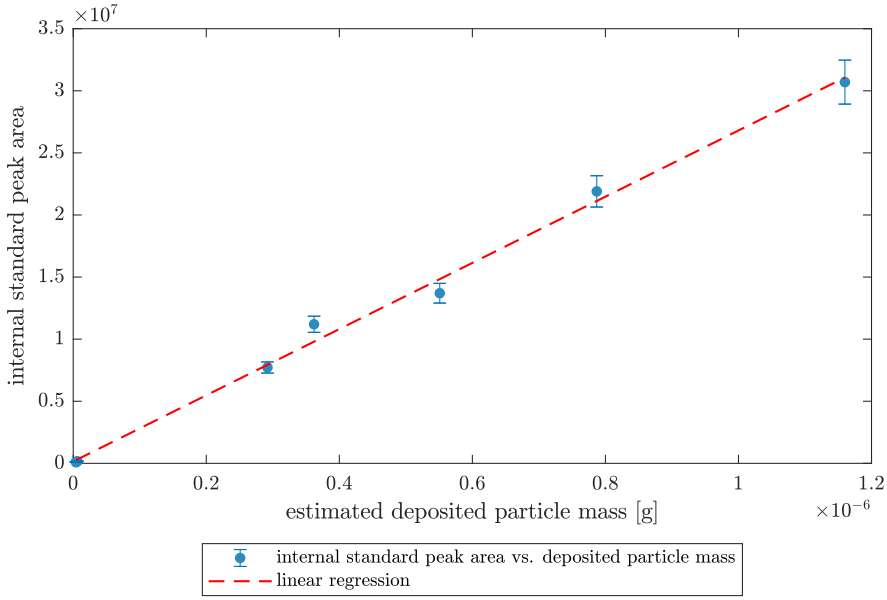

Figure 3.3: The figure shows the linear correlation between the total particle mass deposited on the filter and the peak area of the internal standard. The correlation coefficient $R^2 = 0.9953$ indicates good agreement.

$$PAR_d = \frac{RPA_d}{RPA_{80\,\mathrm{nm}}} \tag{3.1}$$

3.3.4 Particle size-dependent oxidation of 1,3-diphenylisobenzofuran

3.3.4.1 Air-generated aerosols

Here we report the observation of particle size-dependent oxidation of 1,3-diphenylisobenzofuran to 1,2-dibenzoylbenzene. As Fig. 3.4 shows, the extracts from filters sampled with monodisperse aerosol of 20 nm, 50 nm and 80 nm, respectively, exhibit much larger relative peak areas for the smallest particles than for the larger particles, with a PAR_{20} of about 120 (light blue bars), i.e., even normalised to particle mass, more than 2 orders of magnitude more of the oxidation product is found in the 20 nm particles than in the larger particles. The extracts of aerosol samples with a particle size of 50 nm also show larger relative peak areas than those of the 80 nm particles ($PAR_{50} = 2$), even though the effect is much less pronounced. Assuming a heterogeneous oxidation reaction, one would have expected the product yield to scale with particle surface area. However, the particle surface area per unit mass is only a factor of 4 and 1.6 larger for

particles of 20 nm and 50 nm, respectively, than for particles of 80 nm. Therefore, other aspects must also be taken into account.

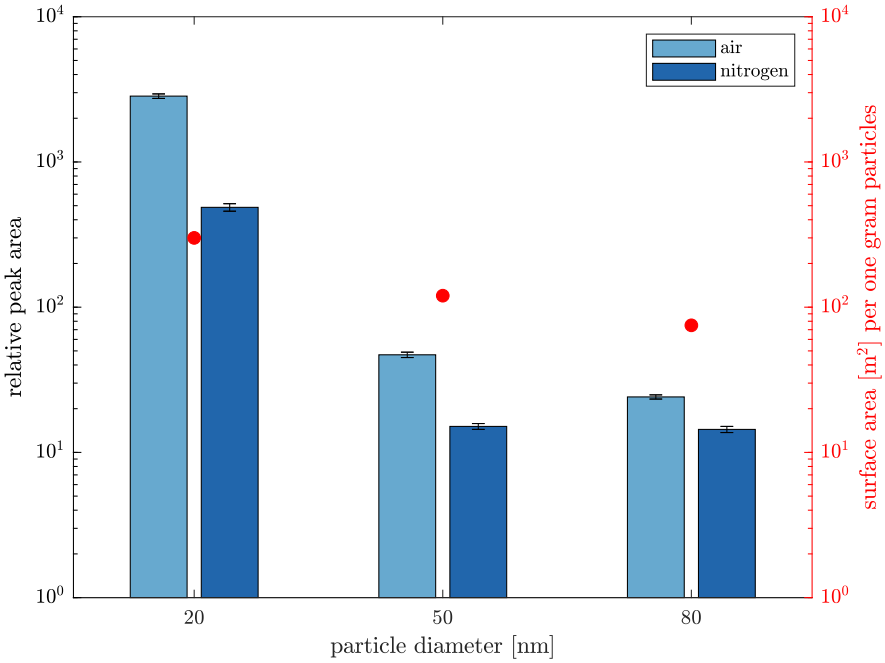

Figure 3.4: Displayed are the relative peak areas of 1,2-dibenzoylbenzene for aerosol samples generated with compressed air (light blue) and nitrogen (blue), respectively, for the three examined aerosol particle sizes. Red markers indicate the calculated surface area per gram particle mass.

As mentioned earlier, studies suggest that organic aerosol particles with diameters greater than 30 nm are amorphous or solid-like particles, but smaller particles tend to be lower viscosity (Virtanen et al. 2010; Riipinen et al. 2012; Reid et al. 2018). Viscosity, in particular, massively affects diffusion coefficients in the condensed phase, which in turn affects the kinetics of chemical reactions, e.g. reactants introduced from the gas phase (Virtanen et al. 2010; Shiraiwa et al. 2011). It is precisely these relationships that provide an explanation for the observations made here: The observed higher concentrations of oxidation products in smaller particles are explained by the low viscosity and the associated higher reactivity. While this influence is still comparatively small in the comparison between 80 nm and 50 nm particles, the striking jump in the smallest particles indicates a correspondingly large difference in viscosity in the 20 nm particles. In addition, the effect of curvature itself could play a role. Since the surface of the smal-

lest particles is much more curved than the surface of the larger particles, differences in surface energy could lead to easier oxidation for particles with a diameter of 20 nm than for the larger particles.

3.3.4.2 Oxygen-depleted aerosol

The gas used for the experiments was generated with a nitrogen generator for LC-MS instruments. According to the manufacturer, the nitrogen generated contains about five percent oxygen. As can be seen in Fig. 3.4, the *RPAs* are generally lower than the *RPAs* of aerosols generated from air. Although this influence can only be interpreted qualitatively due to the lack of a precise determination of the oxygen concentration and also the lack of other oxygen concentrations, it does show that with increased oxygen availability, the product formation of the reaction also increases. These results could also be interpreted as an indication of a size-dependent viscosity. The lower viscosity of small organic particles increases diffusion and mass transport, thus having a decisive influence on the kinetics of the oxidation reactions taking place.

A series of experiments were performed with a reduced aerosol particle residence time of 8.4 minutes. Interestingly, the relative peak areas for 50 nm and 20 nm diameter aerosol samples remained unchanged within the margin of error, but the *RPA* of 80 nm aerosol samples shows a steep drop of about 70 % when the residence time in the flow-tube reactor is reduced, as shown in Fig. 3.5. Shown are the results with the experimental setup with reduced oxygen concentration using the nitrogen generator. Apparently, the reaction rates for particles with diameters of 20 nm and 50 nm are high enough to allow similar yields. A surprisingly large effect was observed for the 80 nm particles, possibly an indication of a sudden increase in viscosity of the investigated organic model substances in the larger particles.

Petters and Kasparoglu (2020) reported increasing depressions of the melting point for spherical particles with decreasing particle size. Assuming the Boyer-Kauzmann relation (Koop et al. 2011; Petters and Kasparoglu 2020) to hold true for this model system, similar size-dependent depressions of the glass transition temperature might result in large variation of the viscosity of differently sized particles. For 1,2-dibenzoylbenzene, a glass transition temperature of 258 K is calculated employing the parametrization described by Li et al. (2020). Under the premise of a reduction of the glass transition temperature to 250 K for particles with a diameter of 80 nm and a further reduction by

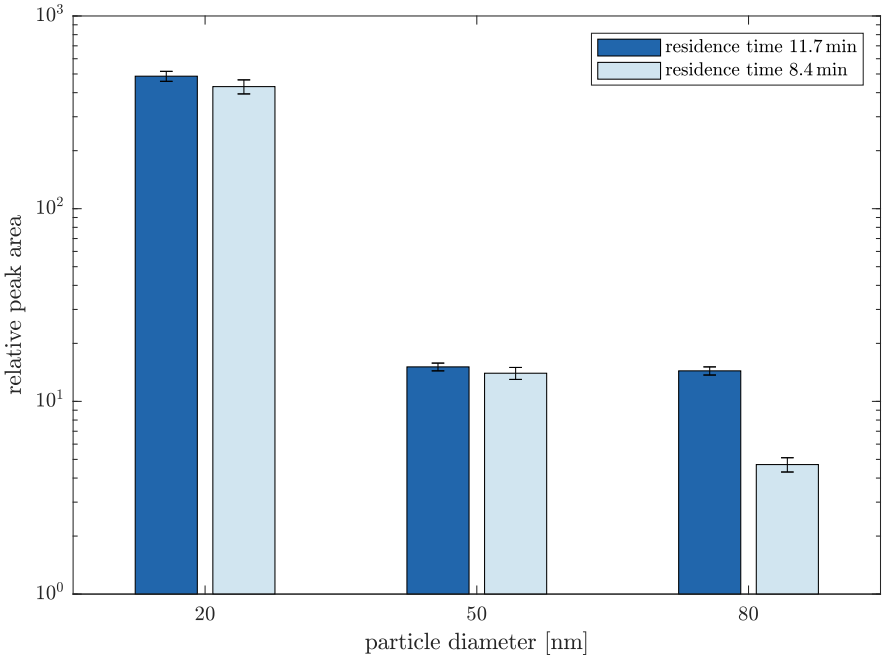

Figure 3.5: The figure shows the relative peak areas for nitrogen-generated aerosol samples at two different flow rates. Shown are the *RPAs* at a flow rate of 1.01 L min^{-1} (dark blue) and 1.41 L min^{-1} (light blue).

20 K for particles with a diameter of 20 nm, a viscosity almost two orders of magnitude higher in 80 nm particles is to be expected.

To investigate the influence of viscosity on the reaction, glycerol was added to the aerosol solutions at a concentration of 40 mg L^{-1}. Glycerol should act as a plasticizer and reduce the viscosity of the aerosol produced. As Fig. 3.6 shows, a remarkable effect can be seen especially in aerosol samples with a particle size of 80 nm, i.e. a significant increase in the formation rate of the oxidation product. Although less pronounced, the aerosol samples with particles of 50 nm diameter also show increased *RPAs* compared to samples without glycerol addition in the aerosol solutions. In contrast, a decrease in *RPAs* is observed for the smallest particles. Moreover, contrary to the previously described trends, the *RPA* for aerosol particles with a diameter of 50 nm is slightly smaller than the corresponding *RPA* for 80 nm aerosol particles.

The increase in *RPA* compared to the aerosol samples generated without glycerol addition indicates faster reactions in these particles, likely due to the lower viscosity in the glycerol-containing particles. Since, as discussed above, viscosity is higher in larger

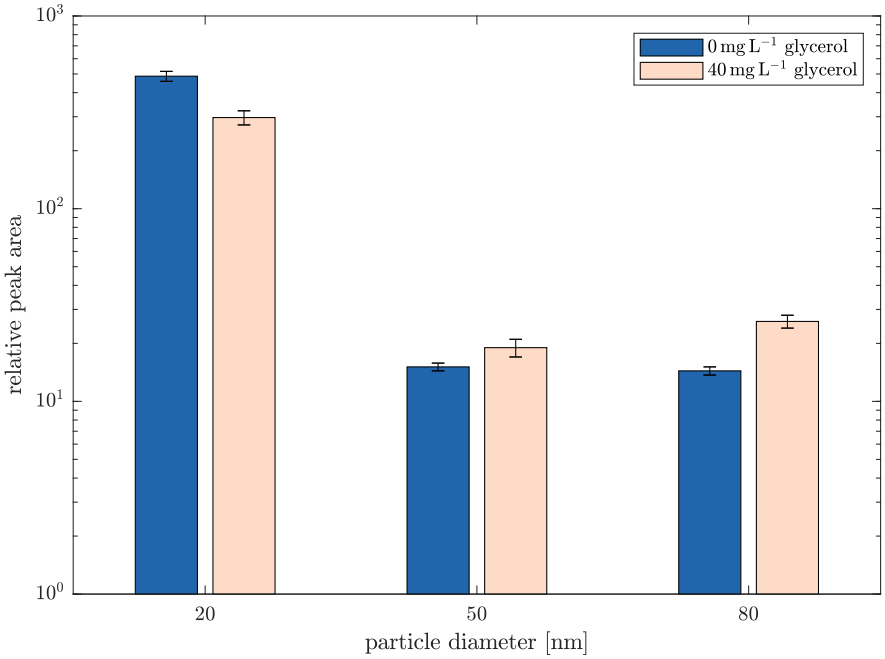

Figure 3.6: The figure shows the *RPAs* for different aerosols. Blue bars represent the *RPAs* of aerosol generated from the solutions described in Table 3.1. Light red bars represent aerosol samples for which glycerol had been added to the solutions prior to nebulisation.

particles, the accelerating effect in the presence of glycerol is most pronounced in the largest particles examined in this study. However, this does not explain the slight reduction in *RPAs* when moving from particles with a diameter of 80 nm to particles with a diameter of 50 nm, nor the reduction in *RPAs* of particles with a diameter of 20 nm when comparing samples prepared with and without the addition of glycerol. A possible reason for the opposite trend for 20 nm particles could be the partial evaporation of glycerol from these particles, possibly favoured by the Kelvin effect. Wright et al. (2016) measured the evaporation of glycerol from aerosol particles and reported rapid volatilisation under dry conditions. On the other hand, the evaporation of glycerol is largely reduced by the presence of water (Wright et al. 2016). Since the aerosol was generated from aqueous solutions, sufficient presence of water can be assumed, and excessive evaporation of glycerol seems unlikely. A possible explanation would be the aggregation of glycerol on the particle surface. Because of the large excess of glycerol, oxidation of 1,3-diphenylisobenzofuran on the particle surface could be hindered by lower surface

concentrations of 1,3-diphenylisobenzofuran. For larger particles, the advantage of lower viscosity could more than compensate for this limitation. Furthermore, the dilution of the aerosol particles with glycerol might be a reason for the reduced *RPAs* in particles of 20 nm in diameter. The lowered concentration of the reactant possibly leads to decreasing rate constants. Additionally, the reduction of the 1,3-diphenylisobenzofuran content also limits the amount of 1,2-dibenzoylbenzene which can maximally be formed assuming a conversion of 100 %.

3.4 Conclusion

In a model system for organic aerosols, we have observed particle size-dependent oxidation reactions. Our studies show that the oxidation of 1,3-diphenylisobenzofuran is favoured in smaller particles. Assuming a heterogeneous reaction, this was to be expected to some extent as the surface-area-to-volume ratio increases with decreasing particle size. Interestingly, the extent to which reactions are favoured in smaller particles by far exceeds the increase in surface-to-volume ratio, suggesting that other effects also play a role. Presumably, the observed effect is due, at least in part, to differences in the viscosity of aerosol particles of different sizes. The observed size-dependent chemistry could play a critical role in the growth of ultrafine particles to sizes at which they can act as CCN. Since this could be an important factor in aerosol particle survival, further studies should be conducted on more atmospherically relevant chemical systems. In addition, the size-dependent chemistry of aerosol particles should not be studied only in the context of heterogeneous reactions. Reactions occurring exclusively in the particle phase could also be affected by particle size.

4 Diels-Alder reactions as model systems for oligomerisation reactions in ultrafine particles

4.1 Introduction

Aerosols have an important impact on the Earth's atmosphere. They are able to interact directly with radiation by reflecting and scattering incoming sunlight, but aerosol particles also act as cloud condensation nuclei and therefore have an indirect influence on Earth's radiative budget (Pöschl 2005; Kolb and Worsnop 2012; Curtius 2006; Seinfeld and Pandis 2006). Even though black carbon aerosols are considered to take part in heating up the atmosphere, aerosols are over all considered to have a negative radiative forcing and therefore are thought to cool the atmosphere (Seinfeld and Pandis 2006; Pöschl 2005; Kolb and Worsnop 2012; Intergovernmental Panel on Climate Change 2014).

Besides their effect on climate, aerosols are also detrimental to human welfare. The migration especially of small particles deeply into the lungs may lead to allergic reactions as well as respiratory and cardiovascular diseases (Pöschl 2005; Kolb and Worsnop 2012; Schulz et al. 2005).

A large part of the total organic aerosol mass consists of secondary organic aerosols (Jimenez et al. 2009; Zhang et al. 2007; Curtius 2006). Secondary organic aerosols, formed in the atmosphere from volatile precursor compounds, also make up the major part of fine and ultrafine aerosols, as growth rates of particles in the size range from 2 nm to 20 nm suggest (Riipinen et al. 2011; Pierce et al. 2011).

The formation of secondary aerosols requires sufficiently low vapour pressures (Seinfeld and Pandis 2006; Riipinen et al. 2011; George and Abbatt 2010). Formation pathways include the gas phase oxidation of volatile organic compounds, heterogeneous oxidations at the surface of aerosol particles, the formation of organic salts in the particle

phase and the formation of higher molecular weight compounds through oligomerisation reactions in the condensed phase (Riipinen et al. 2012; Shang et al. 2016; Kolb and Worsnop 2012; Kroll et al. 2015).

Freshly nucleated particles are prone to scavenging by larger particles. Therefore, the growth rate of ultrafine particles is critical for their survival (Riipinen et al. 2011). Particle size-dependent chemical reactions might hence play a decisive role in the survival of ultrafine particles. If chemical reactions are favoured in smaller particles, the growth rate of small particles might be increased and thus the likelihood of particle losses due to scavenging is decreased.

The size-dependent oxidation in small aerosol particles has been observed and discussed in chapter 3. Besides oxidation reactions, also reactions leading to the formation of higher molecular weight compounds such as oligomerisations might be influenced by particle size: As this kind of reactions involves the formation of chemical bonds, they are usually facilitated by high pressures. According to the equation of Young and Laplace, the pressure within small aerosol particles might be considerably higher than in larger particles, therefore potentially leading to increased reaction rates and in turn a size-dependent chemistry.

Diels-Alder reactions are known to have a high pressure dependence and therefore make a good system to examine the influence of particle size on a chemical reaction. Aerosols have been generated from two solutions containing the reactants of a Diels-Alder reaction and size-classified aerosol samples have been examined by UHPLC-UHRMS to investigate the impact of particle size on the reaction. A size-dependence has been observed under all examined conditions, different however from what was expected.

4.2 Experimental methods

Experimental methods and materials used have been described in detail in chapter 2. Nonetheless, the experimental setup will be described shortly in the following sections.

Aerosols were generated by nebulising two solutions in a Constant Output Atomizer with a mixture of 95 % nitrogen and 5 % oxygen. Solution 1 contained 1,3-diphenylisobenzofuran (1,3-DPIBF) and 3-benzyloxycyclobutane-1,1-dicarboxylic acid (BCDA) as internal standard in methanol. Solution 2 contained maleic acid in ultrapure water. To avoid reactions prior to nebulisation, solutions were delivered separately to the atomizer. Additionally, one set of experiments was executed with the addition of 40 mg L^{-1} glycerol to both solutions to investigate the plasticising effect of glycerol. Further ex-

periments were conducted with methanolic solutions of maleic acid with added glycerol concentrations of 40 mg L^{-1} and 80 mg L^{-1}.

The aerosol was dried by an activated charcoal denuder prior to entering the flow tube reactor. The flow tube was held at atmospheric pressure via a filtered pressure relief between the nebuliser and the denuder. Subsequently, the aerosol was size-classified by an Electrostatic Classifier and the monodisperse aerosol flow was split. Aerosol concentrations were measured by a Water-based Condensation Particle Counter and in parallel filter samples were collected for chemical analysis. Electrically conductive tubing was used to avoid particle losses. Filter samples were stored at −28 °C until extraction.

Filters were cut and extracted with 3 mL of a mixture of methanol and acetonitrile (1:1 (v/v)) for 30 min on an orbital shaker. Solutions were filtered through a syringe filter and the solvents were evaporated at 35 °C under a gentle nitrogen stream. The procedure was repeated twice with volumes of 1 mL each. The combined extracts were dissolved in 0.5 mL of a 9:1 (v/v) mixture of water and acetonitrile and filtered through a syringe filter.

Measurements were conducted on an UHPLC-MS system consisting of an UltiMate 3000 UHPLC system (Dionex, Thermo Fisher Scientific, Bremen, Germany) and a Q-Exactive Orbitrap mass spectrometer equipped with a heated ESI source (Thermo Fisher Scientific, Bremen, Germany). A Hypersil Gold C-18 column was used for separation.

A method was developed to separate and detect the analytes of interest. To obtain the lowest possible limits of detection, the mass spectrometric parameters were optimised for measurements in the positive and negative mode separately.

4.3 Results and discussion

4.3.1 Diels-Alder reaction of 1,3-DPIBF and MA

The reactants 1,3-DPIBF and MA react in a Diels-Alder reaction to form 1,4-diphenyl-1,2,3,4-tetrahydro-1,4-epoxido-naphthalene-2,3-dicarboxylic acid (DTEND).

The formation of DTEND has been observed in numerous laboratory generated aerosol samples. However, no literature regarding the synthesis of DTEND from 1,3-DPIBF and MA is available. Direct synthesis of DTEND from MA and 1,3-DPIBF has not been successful, and the reaction does not take place under standard conditions. Therefore,

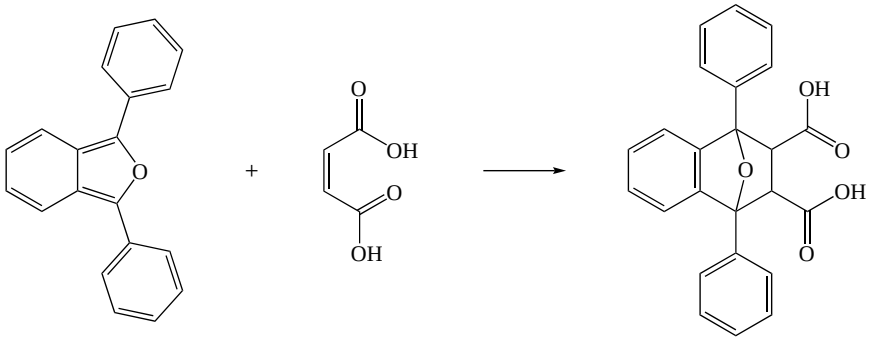

Figure 4.1: Reaction scheme of the Diels-Alder reaction of 1,3-DPIBF with MA to yield DTEND.

separate delivery of the reactants to the nebuliser is not necessary, but was still practised to ensure reactions would be strictly limited to the particle phase.

As no Diels-Alder reaction occurs in the bulk, it seems natural to explain the formation of DTEND by the effect of curvature. In ultrafine particles, the surface energy might be altered due to the strong curvature of the particle surface. Reactions depending upon the curvature of a surface have for example been reported by Fang, Li and Feng (2017) and Kou et al. (2007), who investigated the oxidation of highly curved metal and crystal surfaces. Additionally, Bain et al. (2016) reported the acceleration of reactions in Leidenfrost droplets and the importance of interfacial effects in the acceleration of reactions in microdroplets.

4.3.2 Particle size-dependent DTEND formation

The analysis of liquid extracts of filters sampled with monodisperse aerosols of 20 nm, 50 nm and 80 nm revealed a size-dependence in the formation of DTEND, the product of the Diels-Alder reaction of 1,3-DPIBF and MA. As figure 4.2 shows, the product formation apparently is facilitated in larger aerosol particles. This implies that either the reaction proceeds faster in larger particles, leading to a quicker build-up of the Diels-Alder product, or that the equilibrium of the Diels-Alder reaction is shifted towards the product side for larger particles.

According to the equation of Young and Laplace (eq. 1.18), increasing pressure differences across the surface of particles of decreasing size would be expected. However, the observed size-dependence is contrary to what would be expected from a facilitation of the Diels-Alder reaction by increased pressures, assuming a negative activation and/or

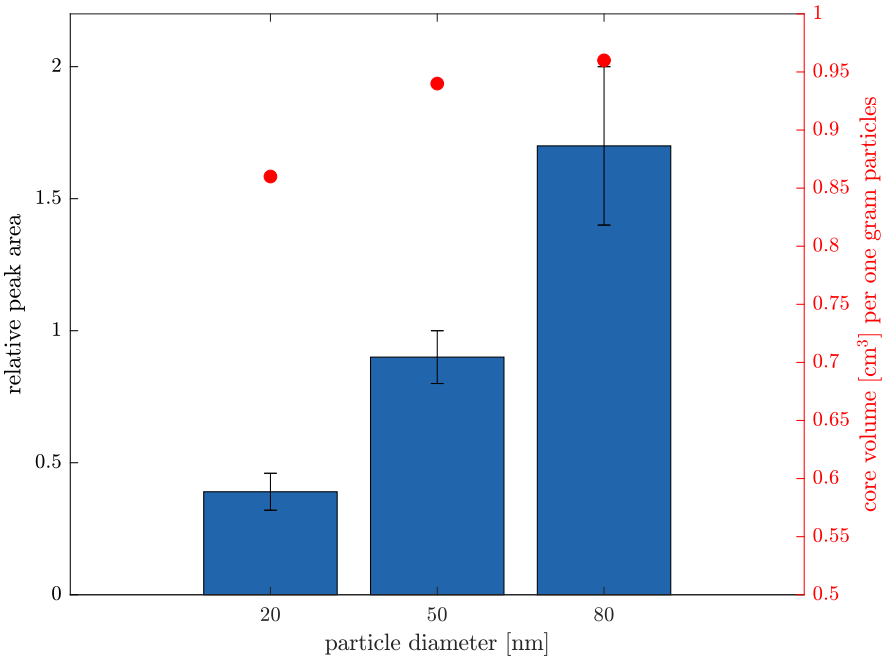

Figure 4.2: Particle size-dependent formation of DTEND. The relative peak areas are plotted against the particle diameter. Red dots mark the particle core volume per one gram of particles at an exemplary surface layer thickness of 0.5 nm.

reaction volume for the formation of DTEND from 1,3-DPIBF and MA. Therefore, other effects must be assumed to be of importance for the size-dependence as well.

1,3-DPIBF is readily oxidised to 1,2-dibenzoylbenzene, as has been reported in chapter 3. As reported, the oxidation of 1,3-DPIBF shows a significant size-dependence with a large preference for smaller particles. Therefore, the degradation of 1,3-DPIBF might limit the extent to which DTEND can be formed, giving a potential explanation of the observed behaviour. However, the differences in the relative peak area of 1,2-dibenzoylbenzene between particles of 80 nm and 50 nm are quite small (approximately 4 %). Consequently, this hardly explains a difference of almost a factor of two between the relative peak areas of DTEND for particles of 80 nm and 50 nm, respectively.

According to Cai et al. (2015), the vapour pressure of maleic acid at 298 K is between 3.74×10^{-4} Pa and 1.71×10^{-3} Pa (3.69×10^{-9} atm to 1.69×10^{-8} atm). Goldstein and Galbally (2007) give the following vapour pressure ranges for VOCs, SVOCs and

non-volatile compounds: substances with vapour pressures larger than 1×10^{-5} atm are considered to be in the gas phase, compounds with vapour pressures ranging from 1×10^{-5} atm to 1×10^{-11} atm will be semivolatile and compounds with lower vapour pressures will be in the condensed phase. Therefore, maleic acid must be considered to be a SVOC which implies partitioning between the gas phase and the condensed phase. Consequently, the differences in particle size may lead to different concentrations of maleic acid in the condensed phase and therefore to different product yields.

Furthermore, the particle surface-to-volume ratio might be a possible explanation for the observed particle size-dependence. Under the obvious assumption that the Diels-Alder reaction proceeds mainly if not exclusively in the particle core and not at the particle surface, a preference for larger particles might be explained by a larger core volume per particle mass, as the red markers in figure 4.2 show for an exemplary surface thickness of 0.5 nm. Going further, also a fixed configuration of molecules at the particle surface – therefore forming a stiff outer layer – might explain the observation, as the reaction volume within the particle is reduced and only a fraction of the molecules is available for the Diels-Alder reaction.

Variation of residence time

Further experiments were conducted to gain better understanding of effects which possibly influence the size-dependence of the Diels-Alder reaction. In a first step, the residence time in the flow tube reactor was decreased from 11.7 min to 8.4 min.

Figure 4.3 shows the resulting relative peak areas of the DTEND signal at particle sizes of 20 nm, 50 nm and 80 nm and for the two different residence times. The overall trend stays the same. The decrease in residence time leads to a decrease in relative peak area for particles of 80 nm in diameter. However, the other particle sizes are much less affected. Whilst barely any change with decreased reaction time is observed for particles of 20 nm in diameter, a slight increase in relative peak area is observed for particles of 50 nm in diameter. The difference between the relative peak areas for particles of 50 nm in diameter is relatively small and within the error margin. Therefore, the difference is probably not significant.

Regardless of the implications of the differences in the relative peak areas for different residence times in the flow tube reactor, the difference between the relative peak areas for particles with a diameter of 80 nm suggests that the chemical reaction is terminated

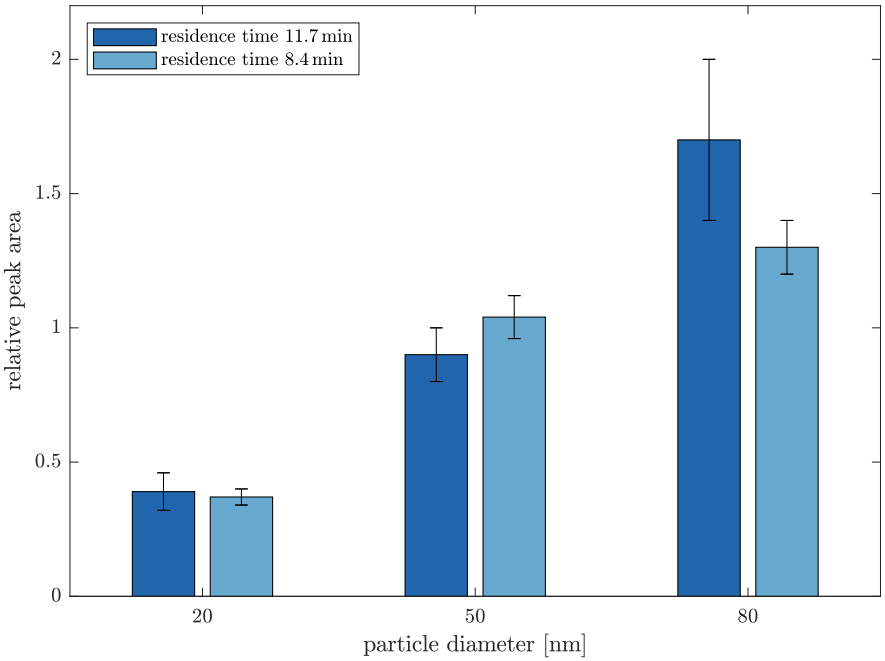

Figure 4.3: Comparison of DTEND yields at different reaction times. The relative peak areas for residence times of 11.7 min and 8.4 min are plotted against the particle sizes.

with the deposition of the particles on the filter, as otherwise the difference in residence times would not imply a difference in reaction times.

As the $RPA_{20\,\mathrm{nm}}$ and $RPA_{50\,\mathrm{nm}}$ remain relatively unaffected by a reduction of the residence time from 11.7 min to 8.4 min, this may indicate that the Diels-Alder reaction has come to completeness in less than 8.4 min. Therefore, it may be deemed unlikely that the reaction is limited by the rate constant, hence probably the equilibrium at the given particle size is reached and the reaction terminated. The difference between the relative peak areas of particles with a diameter of 80 nm at different reaction times indicates that – in contrast to the lower particle sizes – the reaction is not complete after 8.4 min. Probably the equilibrium is not reached in the reduced time span. Therefore, one must assume that the rate constant is not high enough to allow for reaching the equilibrium in the reduced time span. However, with the apparently shifted equilibrium compared to particles with smaller diameters, no conclusion can be drawn on whether or not the rate constant differs from the rate constants in smaller particles.

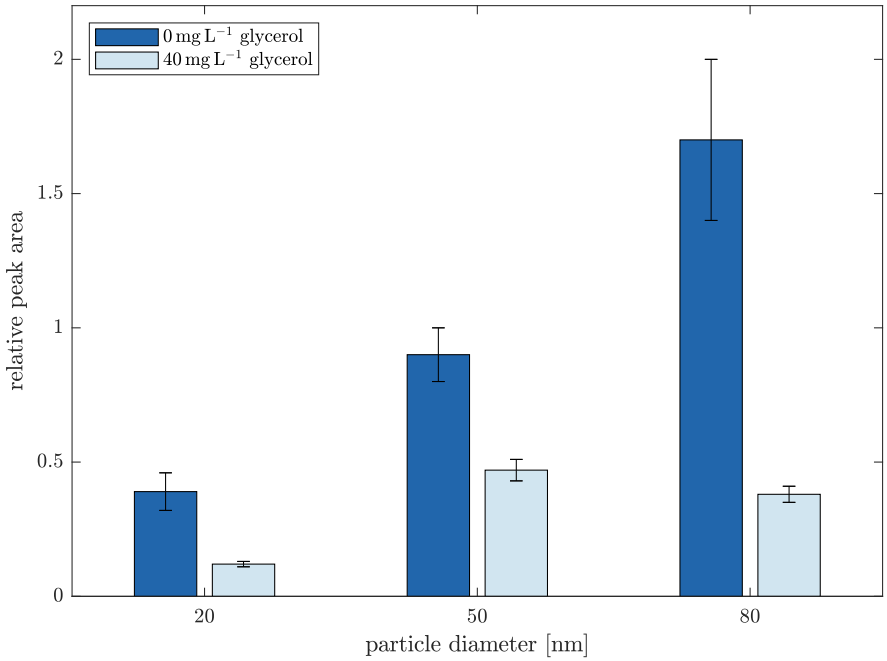

Figure 4.4: Comparison of DTEND yields at different particle sizes and glycerol concentrations. The relative peak areas for glycerol concentrations of 0 mg L^{-1} and 40 mg L^{-1} are plotted against the particle size. Ultrapure water was used as solvent for the solutions of maleic acid.

Addition of glycerol to the nebulisation solutions

Due to the Kelvin effect, the solvents might evaporate more effectively from smaller particles. Accordingly, the evaporation of the solvent might lead to higher viscosities and a limitation of the reaction through impaired diffusion. To avoid bias resulting from different viscosities, 40 mg L^{-1} glycerol were added to all nebulisation solutions.

As figure 4.4 clearly shows, the addition of glycerol leads to an overall decrease in relative peak area compared to samples without glycerol. Additionally, the $RPA_{80\,\mathrm{nm}}$ exhibits a significantly stronger decrease than the relative peak areas for aerosol samples with particle diameters of 20 nm and 50 nm. In fact, the highest relative peak area is observed for aerosol samples with a diameter of 50 nm, amounting to 124 % and 392 % of $RPA_{80\,\mathrm{nm}}$ and $RPA_{20\,\mathrm{nm}}$, respectively.

The observation may be explained by looking at the oxidation of 1,3-DPIBF under the same conditions (see chapter 3). By adding 40 mg L^{-1} glycerol to the nebulisation solutions, the formation of 1,2-dibenzoylbenzene is increased in aerosol particles of

50 nm and 80 nm in diameter, whereas a reduction is observed in particles of 20 nm. In case of the oxidation reaction, this has been explained by a decrease in viscosity in the larger particles. For particles with a diameter of 20 nm, a generally lower viscosity was assumed and therefore no beneficial effect of glycerol expected. The decrease in the formation of the oxidation product was assigned to the aggregation of glycerol at the particle surface which might impede the oxidation reaction.

However, a decrease in viscosity would be expected to also show in the formation of DTEND, increased instead of decreased relative peak areas were therefore expected. As this is not the case, the impact of glycerol on the viscosity of the aerosol particles is likely not the most important factor for the Diels-Alder reaction. Instead, the dilution of the particle phase by the addition of glycerol may exacerbate the Diels-Alder reaction. As the reaction rate depends on the concentration of the reactants, decreased concentrations would be expected to reduce the reaction rate and therefore probably the formation of DTEND in the limited time available for the reaction.

In contrast to particles with diameters of 50 nm and 20 nm, the yield of DTEND in particles with a diameter of 80 nm was influenced strongly by a reduction of the reaction time, as figure 4.3 shows. The assumption was made that in this case the reaction is terminated before the equilibrium was reached and that therefore the reaction rate was too low to complete the reaction in time. Assuming now lowered reaction rates due to the addition of glycerol, the much larger reduction of $RPA_{80\,\mathrm{nm}}$ compared to the reductions of $RPA_{50\,\mathrm{nm}}$ and $RPA_{20\,\mathrm{nm}}$ may be explained similarly: The lowered reaction rate makes reaching the equilibrium for the reaction at this particle size impossible, causing the reaction to be stopped at a *RPA* similar to the *RPA* observed for particles with a diameter of 50 nm, which might indicate the same or at least very similar rate constants in these particles.

Nebulisation from methanolic solutions of maleic acid

Certain amounts of water probably remained in the aerosol particles, to potentially differing degrees due to the Kelvin effect. To further limit the influence of the solvent on the reaction, the aqueous maleic acid solution was replaced with a methanolic solution containing glycerol in concentrations of $40\,\mathrm{mg\,L^{-1}}$ and $80\,\mathrm{mg\,L^{-1}}$. Due to the higher vapour pressure and the removal of gaseous methanol with an activated charcoal denuder, the solvent content was expected to be considerably lower.

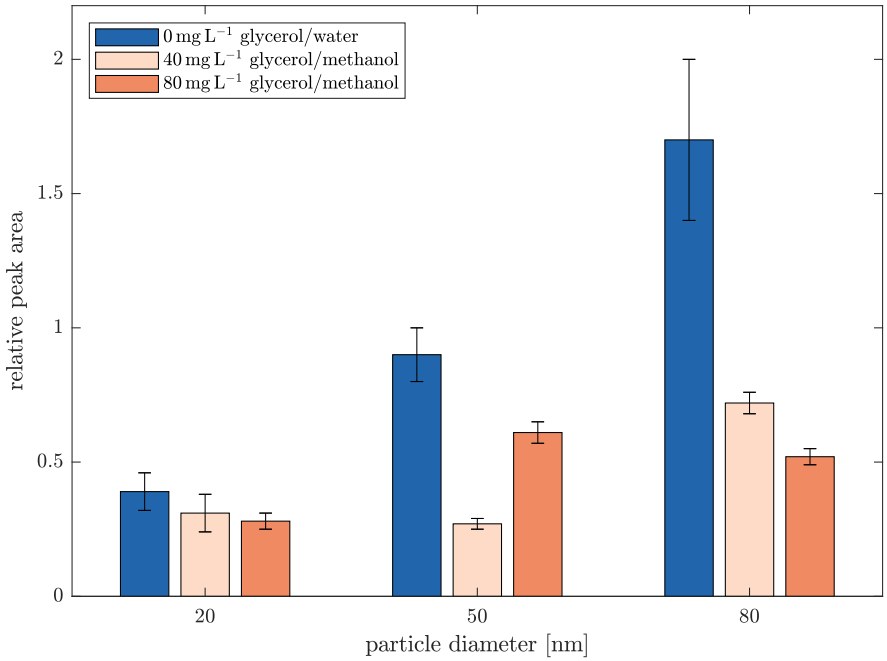

Figure 4.5: Comparison of DTEND yields for different particle sizes and glycerol concentrations of 40 mg L^{-1} and 80 mg L^{-1}. Maleic acid solutions were prepared in methanol. The relative peak areas for the glycerol-free aerosol are displayed for reference. Relative peak areas are plotted against the particle diameter.

Figure 4.5 shows the relative peak areas of DTEND obtained for aerosol particles with diameters of 20 nm, 50 nm and 80 nm and from nebulisation solutions with glycerol concentrations of 40 mg L^{-1} and 80 mg L^{-1}. As described above, the maleic acid solutions with glycerol concentrations of 40 mg L^{-1} and 80 mg L^{-1} were prepared using methanol instead of water as solvent.

Generally, *RPAs* for glycerol-containing samples appear to be smaller than for those without the addition of glycerol. This might again be indicative for dilution effects resulting from the addition of glycerol. Lower reactant concentrations result in lower reaction rates and therefore less DTEND formation in the limited timeframe available for the reaction. Furthermore, Diels-Alder reactions are known to be positively influenced by water (Rideout and Breslow 1980; Clayden, Greeves and Warren 2012), therefore the absence of water might be another reason for the lowered relative peak areas.

Both the trends observed for glycerol concentrations of 40 mg L^{-1} and 80 mg L^{-1} differ from the trend observed for aerosol samples containing no glycerol. At a concentration

of 40 mg L^{-1}, the relative peak area is highest at a particle diameter of 80 nm. The $RPA_{50\,nm}$ appears to be slightly smaller than $RPA_{20\,nm}$, however the difference is within the margin of error and therefore probably insignificant. For aerosols generated from nebulisation solutions containing 80 mg L^{-1}, the highest *RPA* is observed for particles with a diameter of 50 nm, followed by the *RPA* for particles with a diameter of 80 nm.

The observed particle size-dependence at a glycerol concentration of 40 mg L^{-1} might be explained by a reduction of the $RPA_{50\,nm}$. The higher reduction of the *RPA* at this size might result from different effects for larger and smaller particles, none of which is efficient for the formation of DTEND at this particle size. Such effects might be e.g. the Laplace pressure for smaller particles and the surface-to-core-volume ratio for larger particles.

The pattern observed for aerosol samples generated from methanolic solutions containing 80 mg L^{-1} shows similarities to the trend observable for aerosols generated from a methanolic 1,3-DPIBF solution and an aqueous solution of maleic acid, both containing 40 mg L^{-1}. Presumably, also here the reaction rate in the largest particles examined in this study is too low to reach equilibrium in the timeframe available for the reaction, leading to reduced relative peak areas.

Unfortunately, the results for this set of experiments are highly inconsistent. Further experiments are needed to investigate the effects of glycerol on the Diels-Alder reaction of 1,3-DPIBF and MA in particles of different diameters.

4.4 Conclusion

In this study, the reaction of 1,3-diphenylisobenzofuran and maleic acid has been employed to investigate particle size-dependent reactions in ultrafine aerosol particles with diameters of 20 nm, 50 nm and 80 nm. Unlike in the bulk solution, the reaction product has been formed in all examined samples. Therefore, an impact of the highly curved particle surface and resulting chemical conditions seems likely.

The formation of DTEND has been observed to be size-dependent. Unlike the oxidation reaction of 1,3-DPIBF, the Diels-Alder reaction shows a preference for larger particles. Several possible reasons for the size-dependence have been discussed, amongst which are the competition with the oxidation reaction, the volatility of maleic acid, and the different surface-to-volume ratios of the particles. Further studies will be necessary to understand which factors are responsible for the observed effects. Certainly, a reaction system in which none of the reactants is prone to oxidation or other side reactions

is highly desirable, as the oxidation of 1,3-DPIBF complicates the interpretation of the results. Besides Diels-Alder reactions, for example transesterifications would be interesting to examine. Not only are they supposed to be sensitive to the pressure in small particles, but additionally they are of atmospheric relevance.

Besides the investigation of other reaction systems, kinetic measurements would be of great aid to further understand processes in the aerosol phase.

Furthermore, modelling studies might be an interesting approach to get a better understanding of processes of importance for reactions in ultrafine particles. An attempt has been made in chapter 5, albeit further work in this field is necessary. Investigating for example the influence of volatility of reactants and solvents on the reactions might be worthwhile to further the knowledge on size-dependent chemistry.

5 NanoChemistry: Modelling size-dependent chemistry in ultrafine aerosol particles

5.1 Introduction

In the last two chapters of this thesis, several aspects of particle size-dependent chemical reactions have been discussed and possible explanations for the observed effects of particle size have been given. However, influencing factors leading to particle size-dependence are poorly understood. Among the factors which are potentially of importance are the Laplace pressure, viscosity, an influence of the strong curvature on the chemical potential and the ratio between the volumes of particle surface layer and particle core. Furthermore, the Kelvin effect might play a role in the evaporation of one of the reactants as well as the solvents.

To investigate at least some of these factors on a theoretical basis, the NanoChemistry model was developed by Dr. Coraline Mattei and Dr. Thomas Berkemeier at the Multiphase Chemistry department at the Max Planck Institute for Chemistry (MPIC) in Mainz. This model allows for the calculation of the conversion ratio and the number of molecules of each species in any of the two compartments covered by the model. In the model, the conversion ratio is influenced by the Laplace pressure under the assumption of an increase in reaction rate by higher pressures for reactions with a negative activation volume.

5.2 Description of the NanoChemistry model

The NanoChemistry model is a kinetic model which is run in Matlab (Mathworks Incorporated, Natick, MA). To allow for easy variations of the input parameters to the model function, these are read from an external `.mat`-file. The external file contains

the surface tension, the bulk diffusion coefficients of the three species (two reactants and one product), the particle radius and the rate constants for the bulk and surface reaction, respectively. Further parameters are set in the model code, changing them requires modifications to the model itself. These parameters include the temperature, the number of time values for which the output is calculated, start and end time, and the activation volume.

In the model, aerosol particles are subdivided into a surface and a bulk layer. The thickness of the surface layer is calculated from the effective diameter and the number of reactive sites of diene and dienophile. Up to date, no evaporation of solvents, reactants or products is incorporated. Diffusion is regarded only for the migration of reactants and products between the surface layer and the bulk phase, no effect of diffusion within the layers is considered. The model is limited to a single bimolecular reaction which would be expected for a Diels-Alder reaction without side reactions.

From the particle size and the surface tension, the Laplace pressure is calculated. The influence of pressure on the reaction rate is incorporated through a pressure dependent factor which is multiplied with the rate constant at ambient pressure k to yield the rate constant k_p at a given pressure p. Equation 1.23 gives the relation between the activation volume, the pressure and the rate constant, the pressure dependent factor is calculated in eq. 5.1. The influence of pressure on the reaction rate is regarded for the bulk reaction only, the surface reaction is assumed to be uninfluenced by the Laplace pressure.

$$\begin{aligned} \ln k_p &= -\frac{\Delta V^*}{\mathrm{R}T} p \\ \ln k_p - \ln k &= -\frac{\Delta V^*}{\mathrm{R}T} \left(p - 101\,325\,\mathrm{Pa}\right) \\ \ln k_p &= \ln k - \frac{\Delta V^*}{\mathrm{R}T} \left(p - 101\,325\,\mathrm{Pa}\right) \\ k_p &= k \exp\left(-\frac{\Delta V^*}{\mathrm{R}T} \left(p - 101\,325\,\mathrm{Pa}\right)\right) \end{aligned} \tag{5.1}$$

A set of six ordinary differential equations (ODEs) describes the depletion of the reactants and the formation of the product in the two compartments. For both reactants and products, diffusion between the compartments is included. The set of differential equations is solved using Matlabs ODE solver `ode23tb`. The calculations are stabilised by an analytical Jacobian matrix. Starting conditions are given as the number of

molecules of each of the reactants and the product in both the bulk and the surface layer.

5.3 Results and discussion

5.3.1 Variation of modelling parameters

Several parameters of the NanoChemistry model were varied in order to give an impression on reasonable particle sizes, time scales and potentially also rate constants for future experiments.

Variation of particle size

The first parameter to be varied was the aerosol particle size. The particle diameters were varied between 2 nm and 100 nm. Figure 5.1 shows the calculated conversion ratio as a function of time for different particle sizes.

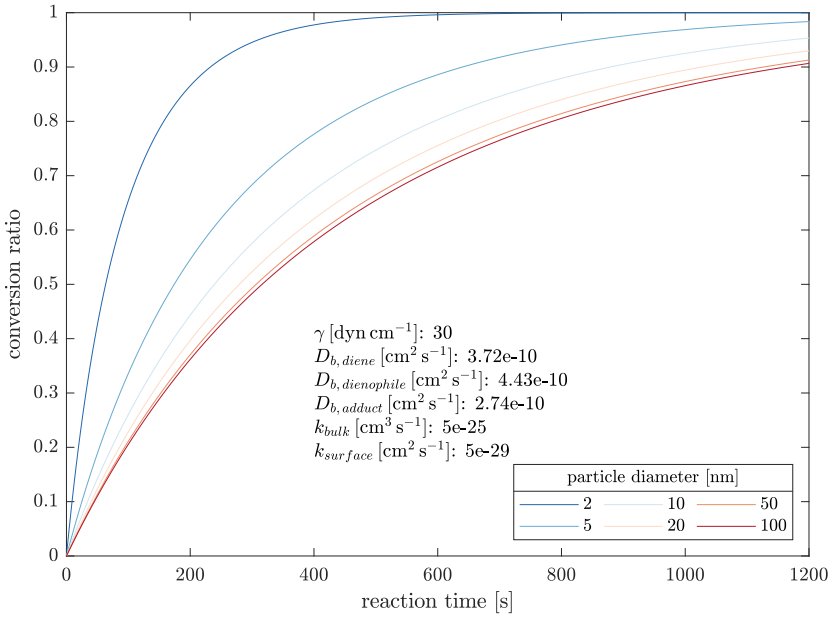

Figure 5.1: Variation of the particle size in the NanoChemistry model between 2 nm and 100 nm. Plotted are the conversion ratios for differently sized particles as a function of reaction time. The inserted text displays the surface tension γ, the diffusion constants D_b for diene, dienophile and Diels-Alder adduct, as well as the rate constants for the surface and bulk reaction used.

Clearly, the differences in conversion ratio are more pronounced the larger the size difference between aerosol particles in question is. Especially the smallest particles with a diameter of 2 nm show a vastly increased reaction rate. On the other hand, the differences in conversion ratio between particles of 50 nm and 100 nm are relatively small. Therefore, examination of particles as small as possible promises to be most interesting. However, these particles are also the most difficult to examine. As the smallest particle size which could reasonably well be investigated with the available equipment would be around 20 nm in diameter, particles with diameters of 20 nm, 50 nm and 80 nm were selected for further experiments.

Figure 5.2 shows the plots for the three selected particle sizes. The differences between the conversion ratios are relatively small at any time. The biggest differences and hence the best detectability of differences is to be expected between a reaction time of 400 s and 600 s.

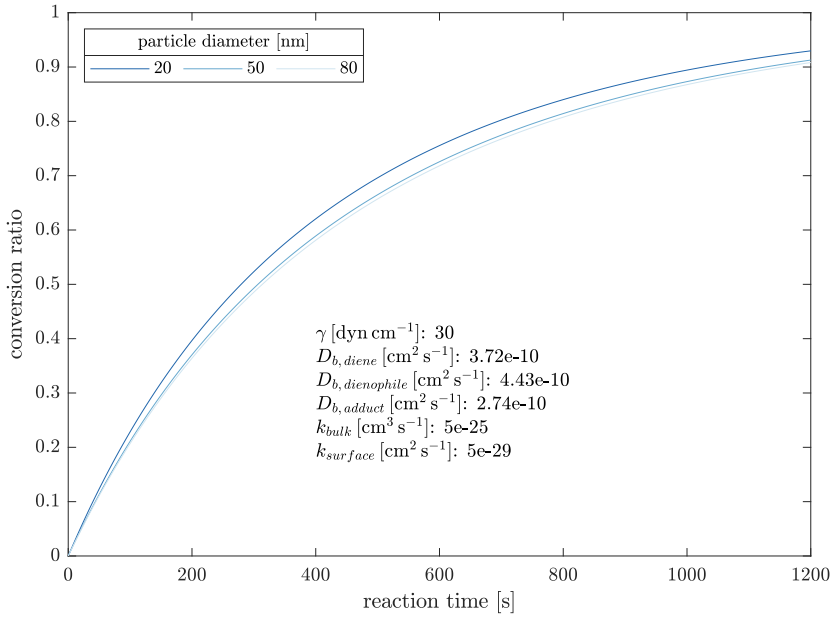

Figure 5.2: Variation of the particle size in the NanoChemistry model between 20 nm and 80 nm. Plotted are the conversion ratios for differently sized particles as a function of reaction time. The inserted text displays the surface tension γ, the diffusion constants D_b for diene, dienophile and Diels-Alder adduct, as well as the rate constants for the surface and bulk reaction used.

Therefore, reaction times of 8.4 min (504 s) and 11.7 min (702 s) were chosen for the experiments. However, due to a lack of data for e.g. surface tension and rate constants, some assumptions had to be made. Furthermore, the model is highly simplified, therefore some caution must be exercised using the data obtained here.

Variation of surface tension

As equation 1.18 demonstrates, the Laplace pressure and therefore potentially the formation of the Diels-Alder adduct depends on the surface tension of the aerosol particles. The surface tension of aerosol particles can be measured directly using e.g. atomic force microscopy, such measurements are however available only for very few SOA systems. To asses the impact of surface tension, it was varied between 20 dyn cm^{-1} and 70 dyn cm^{-1}. Figure 5.3 shows the conversion ratio as a function of reaction time for different surface tensions at an aerosol particle diameter of 50 nm.

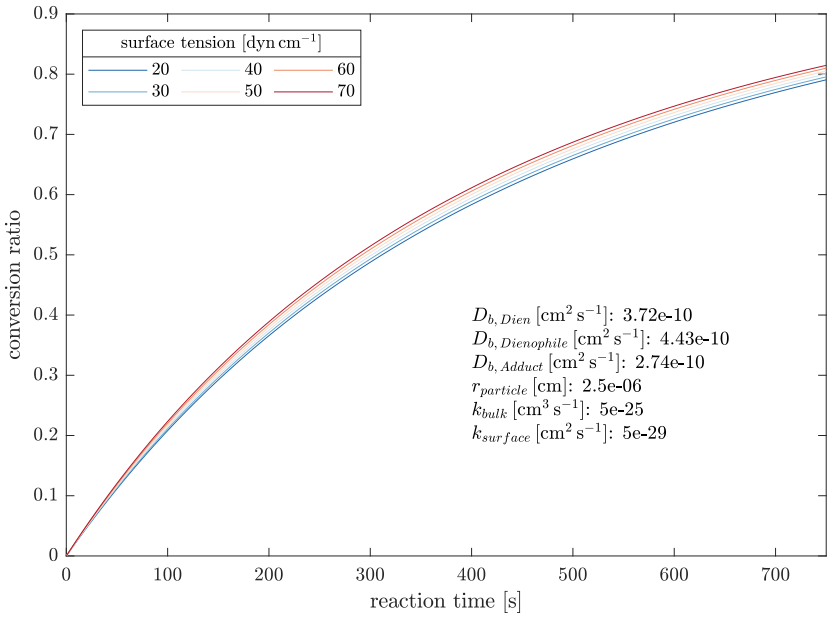

Figure 5.3: Variation of surface tension in the NanoChemistry model between 20 dyn cm^{-1} and 70 dyn cm^{-1}. Plotted are the conversion ratios as a function of reaction time for different surface tensions. The inserted text displays the diffusion constants D_b for diene, dienophile and Diels-Alder adduct, the particle radius $r_{particle}$ as well as the rate constants k for the surface and bulk reaction.

The differences in conversion ratio are relatively small, even when comparing the conversion ratios corresponding to surface tensions of $20\,\mathrm{dyn\,cm^{-1}}$ and $70\,\mathrm{dyn\,cm^{-1}}$. As the trend is very similar regardless of the actual value of the surface tension, these differences are probably negligible. However, differences in surface tension induced by different particle sizes (e.g. through varying evaporation from the particle phase depending on the particle size) might add complexity as well as the need for accurate measurements of the surface tension of single particles.

Variation of bulk rate constant

The bulk rate constant is the rate constant for the reaction happening in the core of the particle. The bulk rate constant was varied over six orders of magnitude between $5 \times 10^{-23}\,\mathrm{cm^3\,s^{-1}}$ and $5 \times 10^{-28}\,\mathrm{cm^3\,s^{-1}}$, the results are plotted in figure 5.4.

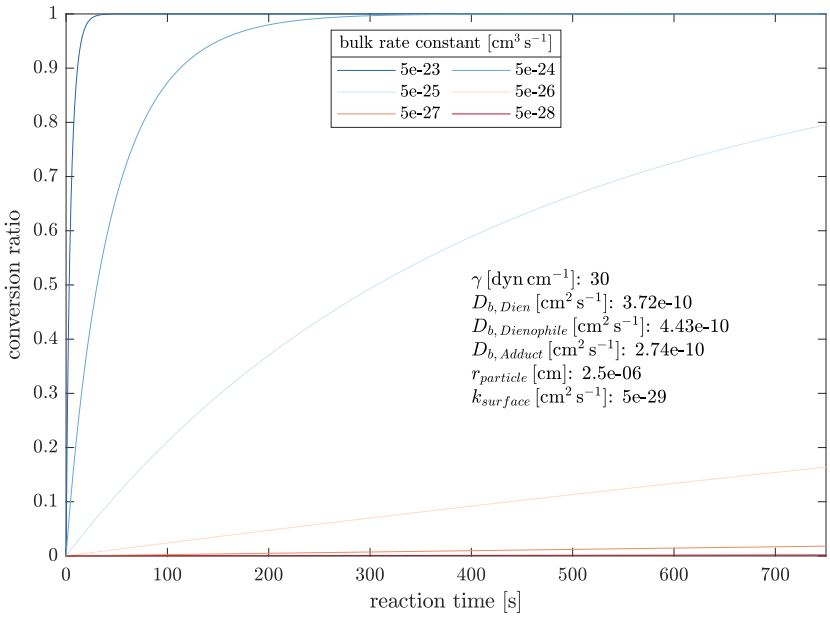

Figure 5.4: Variation of the bulk rate constant in the NanoChemistry model between $5 \times 10^{-23}\,\mathrm{cm^3\,s^{-1}}$ and $5 \times 10^{-28}\,\mathrm{cm^3\,s^{-1}}$. Plotted are the conversion ratios as a function of time for different bulk rate constants. The inserted text displays the surface tension γ, the diffusion constants D_b for diene, dienophile and Diels-Alder adduct, the particle radius $r_{particle}$ as well as the surface rate constant $k_{surface}$.

Figure 5.4 shows clearly that only a relatively small window of bulk rate constants leads to potentially detectable differences in the conversion ratio under the conditions and assumptions made for the model. A bulk rate constant of significantly larger than $5 \times 10^{-25}\,\mathrm{cm^3\,s^{-1}}$ leads to almost complete conversion within the first 300 s, hence differences between particles of different sizes cannot be detected under the experimental conditions. On the other hand, bulk rate constants on the order of $5 \times 10^{-26}\,\mathrm{cm^3\,s^{-1}}$ lead to conversion ratios too low to reliably detect any differences between particles of different diameters.

Therefore, the model might indicate which rate constants are appropriate to detect differences between particles of different sizes. Unfortunately however, for many reaction systems no rate constants are available in the literature which prevents the selection of reaction systems based on their rate constants. Furthermore, a selection based on the NanoChemistry model might oversee interesting systems as e.g. the reaction of 1,3-diphenylisobenzofuran and maleic acid, as the reaction proceeds too slow to be detected in the bulk phase. Nonetheless, the reaction product has been observed in all filters sampled with aerosols generated from solutions of these two reactants. Therefore, other effects of particle size are likely to play a role which are currently not incorporated in the NanoChemistry model.

Variation of surface rate constant

The surface rate constant is the rate constant for the reaction which takes place in the surface layer of the particle. To examine the influence of the surface rate constant, it was varied between $5 \times 10^{-10}\,\mathrm{cm^2\,s^{-1}}$ and $5 \times 10^{-35}\,\mathrm{cm^2\,s^{-1}}$. Figure 5.5 shows the conversion ratios for different surface rate constants as a function of reaction time.

From figure 5.5 the relatively low influence of the surface rate constant is obvious. Only for high surface rate constants of larger than $5 \times 10^{-15}\,\mathrm{cm^2\,s^{-1}}$ an effect is observable. All surface rate constants of $5 \times 10^{-15}\,\mathrm{cm^2\,s^{-1}}$ and lower show the same behaviour, indicating that the bulk rate constant is large enough to mitigate any effect of the variation of the surface rate constant.

5.3.2 Comparison of measurements with modelling results

The results from measuring the extracts of filters sampled with aerosol particles generated from solutions of 1,3-diphenylisobenzofuran (1,3-DPIBF) and maleic acid (MA) were compared to results obtained by running the NanoChemistry model. Several para-

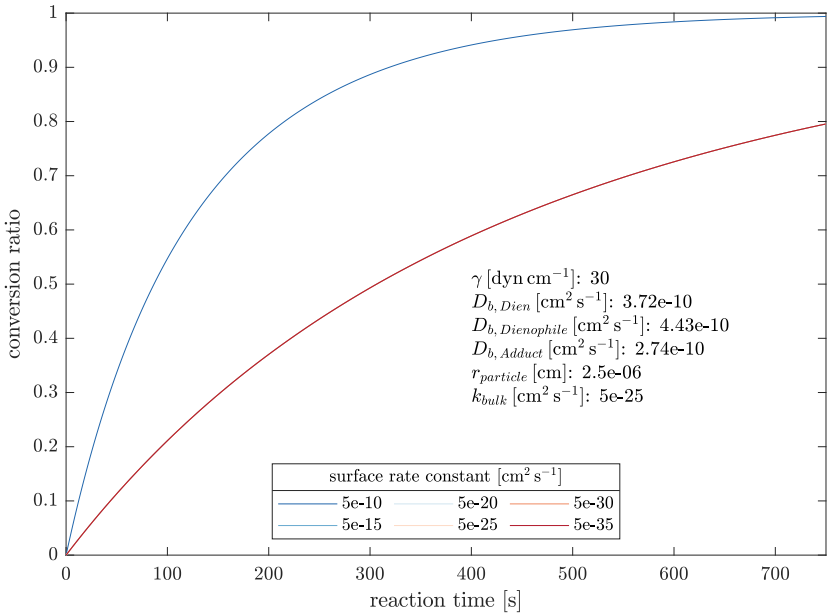

Figure 5.5: Variation of the surface rate constant in the NanoChemistry model between $5 \times 10^{-10}\,\mathrm{cm^2\,s^{-1}}$ and $5 \times 10^{-35}\,\mathrm{cm^2\,s^{-1}}$. The conversion ratios for different surface rate constants are plotted as a function of reaction time. The inserted text displays the surface tension γ, the diffusion constants D_b for diene, dienophile and Diels-Alder adduct, the particle radius $r_{particle}$ as well as the bulk rate constant k_{bulk}. The plotted conversion ratio at a surface rate constant of $5 \times 10^{-35}\,\mathrm{cm^2\,s^{-1}}$ superposes the conversion ratios for surface rate constants from $5 \times 10^{-15}\,\mathrm{cm^2\,s^{-1}}$ to $5 \times 10^{-30}\,\mathrm{cm^2\,s^{-1}}$.

meters in the NanoChemistry model were altered in the endeavour to fit the measured data with modelled data. Figure 4.2 on page 75 displays the data that was attempted to be replicated by modelling. However, the quantity observed in the measurements is the relative peak area of the Diels-Alder product, whereas the NanoChemistry model yields the conversion ratio. Therefore, comparison of both quantities requires some caution. To facilitate the comparison of measured and modelled data, the obtained relative peak areas were divided by the relative peak area obtained for particles with a diameter of 20 nm. The same procedure was applied to the conversion ratios.

As figure 5.6 demonstrates, the measured data is poorly described by the model. Neither the magnitude nor the trend are captured correctly by the model with its standard settings. As discussed in section 4.3.2, a potential explanation for the observed particle size-dependence might be the proceeding of the reaction mainly in the particle

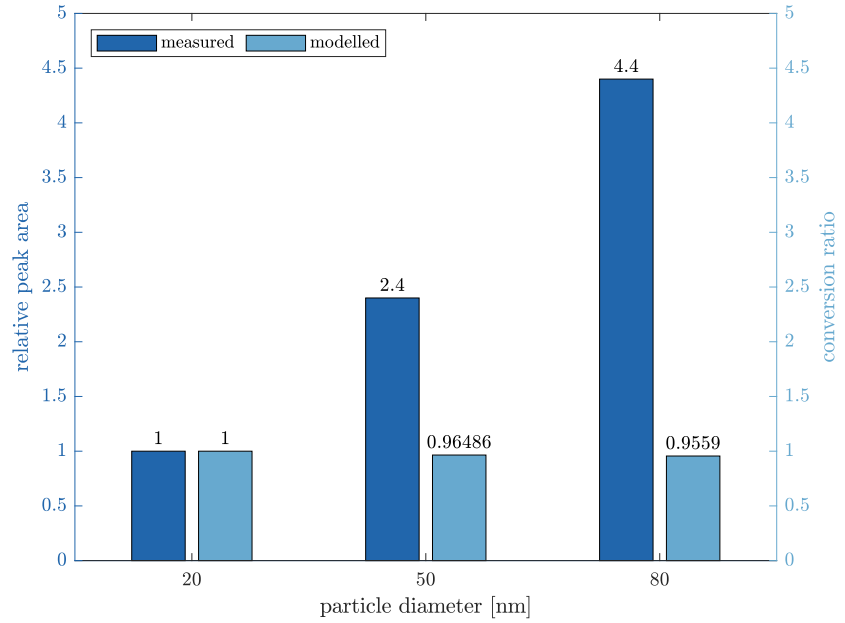

Figure 5.6: Comparison of relative peak areas and conversion ratios for the unaltered NanoChemistry model. Figure A.2 shows the conversion ratios as a function of time and gives the modelling parameters.

core. However, limiting the reaction to the bulk phase in the model does not have a significant influence and no change is observed compared to figure 5.6, as figure A.3 on page 117 shows.

Furthermore, the measured particle size-dependence might be a result of a fixed configuration of molecules at the particle surface. To depict this scenario, the diffusion between bulk and surface layer was prohibited in the NanoChemistry model. Assuming the thickness of the surface layer calculated from the effective molecular diameter, no significant difference to the earlier described observations is seen, as figure A.4 on page 118 shows.

Increasing the thickness of the surface layer to 2 nm in the NanoChemistry model leads to decreasing differences between the conversion ratios of differently sized particles, as figure A.5 on page 119 shows. Further increasing the surface layer thickness to 5 nm finally yields higher conversion ratios for larger particles, as can be seen in figure 5.7.

Interestingly, the highest conversion ratio is observed for particles with a diameter of 50 nm. The conversion ratio of particles of 80 nm in diameter is slightly smaller. This observation suggests at least two different mechanisms at play. One of them is

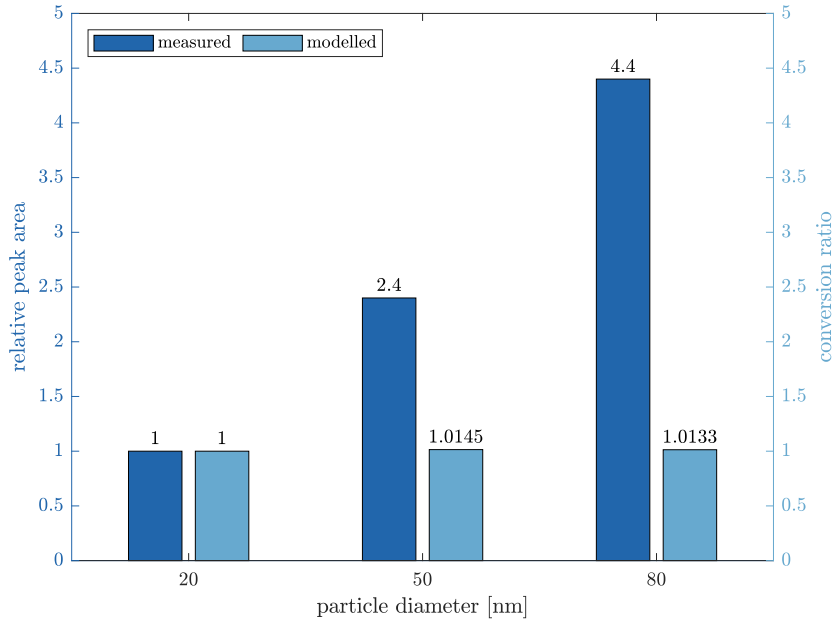

Figure 5.7: Comparison of relative peak areas and conversion ratios at a surface layer thickness of 5 nm. The surface rate constant was set to zero and no diffusion between surface and bulk was allowed. Figure A.6 shows the corresponding conversion ratios as a function of reaction time and gives further modelling parameters.

the facilitation of the Diels-Alder reaction under the increased pressure resulting from the lower diameter of 50 nm compared to 80 nm. This is counteracted by the relatively much larger volume of the surface layer for particles of 50 nm in diameter, where the surface layer volume amounts to 95 % of the bulk layer volume, compared to only 49 % for particles with diameters of 80 nm. Therefore, further increasing the thickness of the surface layer would further favour the product formation in larger particles under the assumption of a non-interacting surface layer. On the other hand, the formation of a surface layer with a thickness of several nanometres seems unlikely. In multilayer models, usually surface layer thicknesses of one effective molecular diameter are applied (see e.g. (Shiraiwa et al. 2012; Shiraiwa, Pfrang and Pöschl 2010)).

In the NanoChemistry model, initially $-50 \times 10^{-6}\,\mathrm{m^3\,mol^{-1}}$ is assumed as the activation volume. This is according to amount a relatively large value which is however not uncommon for Diels-Alder reactions (Borukhova et al. 2015; Klärner, Diedrich and Wigger 1997). Increasing the activation volume to a more conservative value of

$-30 \times 10^{-6}\,\mathrm{m^3\,mol^{-1}}$ leads to a further preference for larger particles, however still far less pronounced than what has been measured. Figure A.7 shows the corresponding plots. Increasing the activation volume further would presumably give higher conversion ratios for particles with diameters of 50 nm and 80 nm, positive activation volumes however are – from the chemical point of view – unlikely, as the transition state is supposed to be smaller in volume due to the occurring formation of two new single bonds.

5.4 Conclusion

Modelling is an interesting addition to laboratory studies. If the model is built upon a solid data base, relatively quick calculations may help in planning of experiments, e.g. by choosing appropriate reaction systems based on rate constants or by determining ideal reaction times. Furthermore, by comparing measured data with results from modelling and varying model inputs to match experimental data, experimental observations may be explained with some certainty.

However, to fully benefit from modelling, it is important to constrain the model with experimental data. The most important data to acquire in this case are probably the rate constants. Furthermore, the NanoChemistry model is oversimplified, as the comparison with measured data has shown. For example the volatilisation of maleic acid as well as the solvents might be an important issue potentially leading to the unexpected preference for the formation of the Diels-Alder adduct in larger particles. Similarly, diffusion is only considered between the two layers of the model, whereas diffusion might also be an issue hindering reactions in highly viscous particles.

For the reaction system investigated in this study, the oxidation of 1,3-diphenylisobenzofuran as a side reaction aggravated matters further. For further studies on this reaction system, the side reaction would have to be incorporated in the NanoChemistry model.

6 Summary and Outlook

In this study the particle size-dependence of two reactions has been investigated and shown. A setup for the generation, size-classification and collection of aerosol particles has successfully been developed. Additionally, a liquid chromatography method was optimised to reliably separate all compounds of the samples. The LC was interfaced to a mass spectrometer via an ESI source for soft ionisation. Ion source and mass spectrometric parameters were optimised for the detection of the analytes in question.

The size-dependence of two reactions could be shown. The oxidation of 1,3-diphenylisobenzofuran to 1,2-dibenzoylbenzene was significantly enhanced in small aerosol particles compared to larger ones. Assuming a heterogeneous oxidation of 1,3-diphenylisobenzofuran, this trend was to be expected due to the differences in the surface-to-volume ratios. However, the magnitude of the preference exceeded the expectations, indicating that other effects are of importance, too. The viscosity of aerosol particles has been described to be dependent on the particle size, with lower viscosities in smaller particles. The lower viscosity might facilitate the oxidation in smaller particles, adding to the effect of the surface-to-volume ratio.

The second size-dependent reaction observed in this study is the Diels-Alder reaction of 1,3-diphenylisobenzofuran with maleic acid. Interestingly, the reaction occurs only in small particles, no reaction could be observed in the bulk and no direct preparation of the product is described in the literature. Presumably, the chemical conditions are altered due to the high degree of surface curvature of small aerosol particles. Unlike the described oxidation reaction, the Diels-Alder reaction preferably proceeds in larger particles. Nonetheless, the effect is much less pronounced than in the case of the oxidation reaction. Potential reasons for the unexpected trend are the competing oxidation of 1,3-diphenylisobenzofuran, the volatility of maleic acid and the difference in surface-to-volume ratios.

Furthermore, a rather simple model was used to calculate the effects of surface tension, particle size and rate constants on the conversion ratio. Additionally, the reproduction of the observed size-dependences of the Diels-Alder reaction has been attempted. How-

ever, in the model only the effect of Laplace pressure is considered and the representation of actual measurements is highly inaccurate.

For future research, achieving higher aerosol concentrations and therefore lower sampling times would be desirable. The Electrospray Aerosol Generator seems to be promising, however a reliable buffer-free aerosol production must be ensured. Furthermore, different approaches to sample collection might be promising. Especially the simultaneous particle collection of a cascade impactor could decrease sampling times hugely. Modern MOUDIs have the capability to collect particles down to 10 nm, unfortunately the cut points of commercially available instruments are spaced too far apart to collect nearly monodisperse particles for the investigation of particle size-dependent chemical reactions. A custom-build would therefore be necessary. As an alternative to sample collection and subsequent chemical analysis, the direct analysis of aerosols via APCI-MS might be worthwhile. Zuth et al. (2018) reported very low limits of detection for their Online-Orbitrap setup, a similar setup might be interesting for investigations on particle size-dependent aerosol chemistry. A FIGAERO-like setup (Lopez-Hilfiker et al. 2014) might further enhance limits of detection if necessary.

Further investigations on the particle size-dependent oxidation of more atmospherically relevant systems might be interesting. Potential systems have been reported by Kroll et al. (2015), examples are the oxidation of squalene, oleic acid or linoleic acid with ozone or hydroxyl radicals. At least as interesting are however reactions in the condensed phase. Care should be taken to select reaction systems in which no competing reaction is to be expected, as the interpretation of results is unnecessarily complicated by side reactions. Furthermore, the investigation of more atmospherically relevant systems such as e.g. transesterifications might be worthwhile. Additionally, kinetic investigations on the examined reactions would be useful, especially with regard to modelling applications.

As an addition to laboratory studies, further numerical investigations on the size-dependent chemistry are necessary. However, the model needs to be far more constrained, important data to add are actually measured rate constants. Furthermore, volatility of the reactants and – depending on the reaction system – the product(s) may be of importance and must be included in a future model. Up to date, diffusion has only been taken into account for the migration of molecules between different layers of the model. In case viscosity is of importance, diffusion must be regarded for the movement of molecules within one compartment in order to precisely depict reality.

A Appendix

A.1 Calculation of Reynolds numbers

The Reynolds number characterises flow around an obstacle or through a pipe and serves as a benchmark to check whether a flow is laminar or turbulent. The flow through a pipe is laminar for Reynolds numbers R_e <2000. The Reynolds number is calculated from the relative velocity v_m, the diameter of the pipe d_{pipe}, the density of the fluid ρ and the viscosity of the fluid ν (Hinds 1999).

$$R_e = \frac{v_m \, d_{pipe} \, \rho}{\nu} \tag{A.1}$$

The relative velocity is obtained from the flow rate F and the cross sectional area of the pipe A_{pipe}:

$$v_m = \frac{F}{A_{pipe}} \tag{A.2}$$

Substituting equation A.2 into A.1 yields equation A.3.

$$R_e = \frac{F \, d_{pipe} \, \rho}{A_{pipe} \, \nu} \tag{A.3}$$

For nitrogen, a density of $1.12\,\mathrm{g\,L^{-1}}$ and a viscosity of $1.80 \times 10^{-5}\,\mathrm{kg\,s^{-1}\,m^{-1}}$ (Lide 2005) were assumed and correspondingly, a density of $1.20\,\mathrm{g\,L^{-1}}$ and a viscosity of $1.81 \times 10^{-5}\,\mathrm{kg\,s^{-1}\,m^{-1}}$ were assumed for air (Hinds 1999).

A.2 Matlab scripts

A.2.1 Import of particle concentration data

The following Matlab function was used to import the data from the .csv file generated by Aerosol Instrument Manager. The imported data was further used to calculate filter loading (see section A.2.2).

```
function [d,date] = import_CPC_TSI_mb(filename_CPC)
%Import of size distribution data from .csv-file
%   import .csv-data as table using fopen and textscan in
   variable d
%   extract date from imported data
%   convert table in string array
%   separate particle sizes
%   convert to double
fileID=fopen(filename_CPC,'r'); %acquire file-ID for SMPS-
   file
formatSpec = '%s%s%s%s%s%[^\n\r]';%give format spec - treat
    everything as string
startRow = 1; %define start row
endRow = inf; %define end row
f=textscan(fileID,formatSpec,endRow(1)-startRow(1)+1,'
   Delimiter',',','ReturnOnError',0); %read .csv file
fclose(fileID); %close file
d=[f{1:end-1}]; %convert array of cells to cell array
date=datetime(d(4,2),'InputFormat','yyyy-MM-dd HH:mm:ss');
date=datestr(date,'yyyymmdd');
end
```

A.2.2 Calculation of filter loading from particle concentration data

The particle mass deposited on the filter during sampling was calculated from the flow rates and the particle concentrations measured by the CPC. The following code was used to calculate the filter loading.

```
%% Script for estimation of filterloading

% * Import of .csv data from TSI CPC
% * display of particle concentration data
% * export of plotted concentration data as .eps and .png-
   files

% Use of LaTeX for displaying headers, labels etc.
set(groot,'DefaultTextInterpreter','latex');
set(groot,'DefaultAxesTickLabelInterpreter','latex');
set(groot,'DefaultAxesFontName','latex');
set(groot,'DefaultLegendInterpreter','latex');
set(groot,'DefaultColorbarTickLabelInterpreter','latex');
%% enter measurement parameters

% * name of data file(s)
% * path of data file(s)
% * selected particle size (nm)
% * assumed particle density
% * flow rates (total, CPC)

prompt1={'Number of data files:'};
dlg_title1 = 'Number of data files';
j=inputdlg(prompt1,dlg_title1,[1 50]);
df=str2double(j{1,1}); %read out number of data files

filename=cell(df,1); %preallocate filename for performance
for j=1:df
    prompt2={'Name of data file', 'Path of data file'};
    dlg_title2='File name and path';
```

```
    j=inputdlg(prompt2,dlg_title2,[1 50]);
    filename{df,1}=[j{2,1},'\',j{1,1}]; %write path and
       file name to filename
end

prompt4={'Path for saving figure','Name for figure'};
dlg_title4 = 'Figures';
j=inputdlg(prompt4,dlg_title4,[1 50]);
pathname=[j{1,1},'\',j{2,1}];
%%
conditions=cell(4,1);
prompt3={'Selected particle size [nm]:', 'Assumed particle
   density [g/ccm]:', 'Total flow rate [L/min]:', 'CPC flow
   rate [L/min]'};
dlg_title3='Sampling conditions';
j=inputdlg(prompt3,dlg_title3,[1 50]);
conditions{1,1}=str2double(j{1,1});
conditions{2,1}=str2double(j{2,1});
conditions{3,1}=str2double(j{3,1});
conditions{4,1}=str2double(j{4,1});

%% Import data from .csv file
datafile=cell(df,1);
for k=1:df
    [datafile{k,1},date] = import_CPC_TSI_mb(filename{k,1})
       ; % use function import_CPC_TSI_mb to import the
       whole .csv-file,
    %extract date and particle size information
end
data{1,13}=date;

%% extract time and particle concentration from datafile
time=cell(df,1); %preallocate cell array for better
   performance
```

```
prtcounts=cell(df,1); %preallocate cell array for better
   performance
clock=cell(df,1); %preallocate cell array for better
   performance
for k=1:df
    time{k,1}=datafile{k,1}(17:end,2); %extract time values
        from datafile
    time{k,1}=str2double(time{k,1}); %convert strings to
       double
    clock{k,1}=datafile{k,1}(17:end,1); %extract date and
       time from datafile
    prtcounts{k,1}=datafile{k,1}(17:end,4); %extract
       particle concentrations from datafile
    prtcounts{k,1}=str2double(prtcounts{k,1}); %convert
       strings to double
end

%% concatenate time and particle concentration sets
time_cat=[];
prtcounts_cat=[];
clock_cat=[];
for k=1:df
    time_cat=[time_cat;time{k,1}];
    prtcounts_cat=[prtcounts_cat;prtcounts{k,1}];
    clock_cat=[clock_cat;clock{k,1}];
end
time_dur=duration(0,0,time_cat); %convert the time data
   from double to duration
time_str=string(time_dur);

%% calculate total counts
counts=trapz(prtcounts_cat); %integrate area using trapz to
    get total CPC-counts
filter_FR=conditions{3,1}-conditions{4,1};
```

```
FR_factor_filter=filter_FR./0.3;
filter_counts=FR_factor_filter*counts;

%% calculate deposited mass
V_p=4/3*pi*(0.5*conditions{1,1}*1E-9)^3; %calculate volume
   of one particle
V_tot=V_p*filter_counts; %calculate volume of all particles
mass_filter=V_tot*1E6*conditions{2,1}; %calculate deposited
    mass

%% plot particle counts
figure
plot(time_dur,prtcounts_cat)
xlabel('Time $\mathrm{[hh:mm:ss]}$');
ylabel('Particle counts');
%ylim([0 40000]);
ax=gca;
figuretext={['estimated deposited particle mass [g]: ',
   num2str(mass_filter)]};
text(ruler2num(time_dur(round(0.1*length(time_dur))),ax.
   XAxis),10000,figuretext,'Interpreter','latex');

print('-painters',pathname,'-depsc');
print('-painters',pathname,'-dpng','-r400');
```

A.2.3 Evaluation of CPC data

The following Matlab code was used to analyse and plot particle concentration data after import with the function described in A.2.1. Imported data is split into individual datasets to compare particle concentrations under different experimental conditions and data is saved as a `.mat`-file for further calculations.

```
%% Script for display and analysis of CPC data

% * Import of .csv data from TSI CPC
% * display of particle concentration data
% * comparison of different datasets
% * export of plotted concentration data as .eps and .png-
   files
% * display of descriptive parameters

% Use of LaTeX for displaying headers, labels etc.

set(groot,'DefaultTextInterpreter','latex');
set(groot,'DefaultAxesTickLabelInterpreter','latex');
set(groot,'DefaultAxesFontName','latex');
set(groot,'DefaultLegendInterpreter','latex');
set(groot,'DefaultColorbarTickLabelInterpreter','latex');
%% enter measurement parameters

% * name of data file(s)
% * data averaging (1 Hz, 10 Hz, 50 Hz)
% * number of "data sets" aka different measuring
   conditions
% * identifyer for each data set
% * start and end time for each data set

prompt1={'Number of data sets:','Number of data files:', '
   data averaging (1 Hz, 10 Hz, 50 Hz):','selected particle
   size [nm]:','Did you take filter samples? (y/n)'};
dlg_title1 = 'Number of data sets';
```

```
j=inputdlg(prompt1,dlg_title1,[1 50]);
i=str2double(j{1,1}); %read out number of data sets
df=str2double(j{2,1}); %read out number of data files
dr=str2double(j{3,1}); %read out data averaging rate
data=cell(i,15);
data{1,12}=str2double(j{4,1});
fs=j(5,1);

if strcmp(fs,'y')
    prompt5={'first examined parameter (with units):','
       second examined parameter (with units):','Start of
       sampling (HH:mm)', 'End of sampling (HH:mm)'};
    dlg_title5 = 'Examined parameters';
    options5.Interpreter = 'tex';
    options5.Resize='on';
    defAns5={'x [xx]','y [yy]', 't_start [HH:mm]', 't_end [
       HH:mm]'};
    j=inputdlg(prompt5,dlg_title5,[1 50; 1 50;1 50;1 50],
       defAns5,options5);
    data{1,14}=j{1,1};
    data{1,15}=j{2,1};
    s_start=j{3,1};
    s_end=j{4,1};
else
    prompt5={'first examined parameter (with units):','
       second examined parameter (with units):'};
    dlg_title5 = 'Examined parameters';
    options5.Interpreter = 'tex';
    options5.Resize='on';
    defAns5={'x [xx]','y [yy]'};
    j=inputdlg(prompt5,dlg_title5,[1 50; 1 50],defAns5,
       options5);
    data{1,14}=j{1,1};
    data{1,15}=j{2,1};
```

```
end

%%
m=cell(3,1);
m{6,1}='00:00:00';
aflowrate=cell(i,1);
for k=1:i
    l=num2str(k);
    txtprompt1=[data{1,14},' for measurement ',l];
    txtprompt2=[data{1,15},' for measurement ',l];
    prompt2={'Identifyer for this data set:',txtprompt1,
       txtprompt2,'aerosol flow rate [L/min]','start time (
       hh:mm:ss)','end time (hh:mm:ss)'};
    dlg_title2 = ['Measurement parameters for measurement',
        ' ',l];
    options2.Interpreter = 'tex';
    options2.Resize='on';
    defAns2={l,'','','',m{6,1},''};
    m=inputdlg(prompt2,dlg_title2,[1 70; 1 70; 1 70;1 70;1
       70;1 70],defAns2,options2);
    data{k,1}=m{1,1};
    data{k,2}=m{5,1};
    data{k,3}=m{6,1};
    data{k,9}=m{2,1};
    data{k,10}=m{3,1};
    data{k,9}=str2double(data{k,9});
    data{k,10}=str2double(data{k,10});
    aflowrate{k,1}=str2double(m{4,1}); %get aerosol flow
       rate
end
%%
filename=cell(df,1);
for k=1:df
    l=num2str(k);
```

```
    prompt3={'Name of data file:'; 'Path of data file:'};
    dlg_title3 = ['Name of data file', ' ',1];
    options3.Interpreter = 'tex';
    options3.Resize='on';
    defAns3={'x';'path'};
    m=inputdlg(prompt3,dlg_title3,[1 70],defAns3,options3);
    filename{k,1}=[m{2,1},'\',m{1,1}];
end
prompt4={'Path for saving files:'};
dlg_title4 ='Path for saving files';
options4.Interpreter = 'tex';
options4.Resize='on';
defAns4={'path'};
savepath1=inputdlg(prompt4,dlg_title4,[1 70],defAns4,
   options4);
savepath=savepath1{1,1};

%% Import data from .csv file
datafile=cell(df,1);
for k=1:df
    [datafile{k,1},date] = import_CPC_TSI_mb(filename{k,1})
       ;% use function import_CPC_TSI_mb to import the whole
        .csv-file,
    %extract date and particle size informations
end
data{1,13}=date;

%% extract time and particle concentration from datafile
time=cell(df,1); %preallocate cell array for better
   performance
prtconc=cell(df,1); %preallocate cell array for better
   performance
clock=cell(df,1); %preallocate cell array for better
   performance
```

```
for k=1:df
    time{k,1}=datafile{k,1}(17:end,2); %extract time values
        from datafile
    time{k,1}=str2double(time{k,1}); %convert strings to
       double
    clock{k,1}=datafile{k,1}(17:end,1); %extract date and
       time from datafile
    prtconc{k,1}=datafile{k,1}(17:end,3); %extract particle
        concentrations from datafile
    prtconc{k,1}=str2double(prtconc{k,1}); %convert strings
        to double
end

%% concatenate time and particle concentration sets
time_cat=[];
prtconc_cat=[];
clock_cat=[];
for k=1:df
    time_cat=[time_cat;time{k,1}];
    prtconc_cat=[prtconc_cat;prtconc{k,1}];
    clock_cat=[clock_cat;clock{k,1}];
end

%% separate measurement data into data sets
time_dur=duration(0,0,time_cat); %convert the time data
   from double to duration
time_str=string(time_dur);
for k=1:i
    x=data{k,2};
    x=string(x);
    hit=strfind(time_str,x);
    emptyIndex = cellfun('isempty', hit);
    hit(emptyIndex) = {0};
    hit1 = logical(cell2mat(hit));
```

```
    start=find(hit1,1,'first');
    x=data{k,3};
    x=string(x);
    hit=strfind(time_str,x);
    emptyIndex = cellfun('isempty', hit);
    hit(emptyIndex) = {0};
    hit1 = logical(cell2mat(hit));
    finish=find(hit1,1,'last');
    data{k,4}=time_dur(start:finish);
    data{k,5}=prtconc_cat(start:finish);
end

%% Smooth data using moving average and set beginning of
   each measurement to zero
for k=1:i
    data{k,7}=smooth(data{k,5},dr,'moving');
    data{k,6}=data{k,4}-data{k,4}(1);
end

%% Plot (and export if wanted) smoothed data against time
prompt7={'Do you wish to export plotted data?(y/n)'};
dlg_title7 = 'Export of plotted data';
j=inputdlg(prompt7,dlg_title7,[1 50]);
if j{1,1}=='y'
    prompt8={'Do you wish to export plotted data as
       subplots ("sub") or each plot on its own ("singly")?'
       };
    dlg_title8 = 'Export of plotted data';
    z=inputdlg(prompt8,dlg_title8,[1 50]);
    if strcmp(z{1,1},'singly')
        for k=1:i
            figure
            plot(data{k,6},data{k,7})
            xlabel('Time $\mathrm{[hh:mm:ss]}$')
```

```
        ylabel('Particle concentration $\left[\mathrm{
            cm^{-3}}\right]$')
        k_name=num2str(k);
        title(['Measurement ',k_name]);
        name=[savepath,'\',date,'
            _particleconcentration_vs_time_',k_name];
        print('-painters',name,'-depsc'); %print figure
            as .eps
        print('-painters',name,'-dpng'); %print figure
            as .png
    end
elseif strcmp(z{1,1},'sub')
    num_row_2=i/2;
    num_row=ceil(num_row_2);
    figure
    for k=1:i
        subplot(num_row,2,k);
        plot(data{k,6},data{k,7})
        xlabel('Time $\mathrm{[hh:mm:ss]}$')
        ylabel('$c\, \left[\mathrm{cm^{-3}}\right]$')
        k_name=num2str(k);
        title(['Measurement ',k_name]);
    end
    name=[savepath,'\',date,'
        _particleconcentration_vs_time_sub'];
    set(gcf, 'PaperUnits', 'centimeters');
    x_width=20 ;
    y_width=25;
    set(gcf, 'PaperPosition', [0 0 x_width y_width]);
    %set(gcf,'PaperPositionMode','auto')
    print('-painters',name,'-depsc'); %print figure as
        .eps
    print('-painters',name,'-dpng'); %print figure as .
        png
```

```
    end
else
    for k=1:i
        figure
        plot(data{k,6},data{k,7})
        xlabel('Time $\mathrm{[hh:mm:ss]}$')
        ylabel('Particle concentration $\left[\mathrm{cm
           ^{-3}}\right]$')
        k_name=num2str(k);
        title(['Measurement ',k_name]);
    end
end

%% Calculate mean value for each data set
for k=1:i
    data{k,8}=mean(data{k,5});
end

%% Export data-file for further processing
filename_mat=[savepath,'\',date,'.mat'];
save(filename_mat,'data');
```

A.2.4 Heatmap plots of CPC data

The following code was used to generate heatmap-like figures from CPC data evaluated with the Matlab code given in section A.2.3. The `.mat`-files from multiple measurements are gathered, the values are sorted and plotted.

```
%% Initialize LaTeX interpreter for Matlab
set(groot,'DefaultTextInterpreter','latex');
set(groot,'DefaultAxesTickLabelInterpreter','latex');
set(groot,'DefaultAxesFontName','latex');
set(groot,'DefaultLegendInterpreter','latex');
set(groot,'DefaultColorbarTickLabelInterpreter','latex');

%% Load .mat-files
prompt={'How many .mat-files do you wish to import?'};
dlg_title='Number of -mat-files';
options.Interpreter='tex';
options.Resize='on';
defAns={''};
a=inputdlg(prompt,dlg_title,[1 50],defAns,options);
num_mat=str2double(a{1,1});
filename=cell(num_mat,1);
data_load=cell(num_mat,1);
for k=1:num_mat
    prompt1={'Enter name';'and path of .mat-file you wish
       to load'};
    dlg_title1='Load .mat-files';
    options1.Interpreter='tex';
    options1.Resize='on';
    defAns1={'','path'};
    b=inputdlg(prompt1,dlg_title1,[1 50; 1 50],defAns1,
       options1);
    path{k,1}=b{2,1};
    filename{k,1}=[b{2,1},'\',b{1,1}];
end
for k=1:num_mat
```

```
    s_load=load(filename{k,1});
    c_load=struct2cell(s_load);
    data_load{k}=c_load{1,1};
end
data_comb=cat(1,data_load{1:num_mat,1});
ps=data_comb{1,12};

%% process data for plotting
data_map=[[data_comb{:,9}]',[data_comb{:,10}]',[data_comb
   {:,8}]']; %collect relevant data in one array
data_map_sort=sortrows(data_map,[1 2]); %sort array
   according to var1 and var2
l=length(data_map_sort);
first=find(data_map_sort,1,'first'); %find first entry of
   var1
first_val=data_map_sort(first); % find value of first entry
    of var1
last=find(data_map_sort==first_val,1,'last'); %find last
   entry of this value
data_map_sort_new=data_map_sort(first:last,3)'; %rearrange
   data in new array
var1=unique(data_map_sort(:,1)); %read out x- and y-values
var2=unique(data_map_sort(:,2));
%var1=[var1;0];
%var2=[var2;0];
data_map_sort=data_map_sort(last+1:end,:); %"shorten" array
    by values already entered in new array
n=size(data_comb,1);
for k=1:n
    if last<l %do the same thing again for remaining data
        first=find(data_map_sort,1,'first');
        first_val=data_map_sort(first);
        last=find(data_map_sort==first_val,1,'last');
```

```
        data_map_sort_new=[data_map_sort_new;data_map_sort(
            first:last,3)'];
        data_map_sort=data_map_sort(last+1:end,:);
    end
end
data_map_sort_new=data_map_sort_new';

%% create plot of particle concentration and the two
    variables
plot_comp=figure('Name','Figure'); %create figure
axes1=axes('Parent',plot_comp); %create axes object
imagesc(axes1,var1,var2,data_map_sort_new) %print surf to
    figure
%axes1.YDir='normal'; %set y-axis direction to 'normal'
axes1.XTick=var1; %define ticks on x-axis as values from
    var1
axes1.YTick=var2; %define ticks on y-axis as values from
    var2
c=colorbar; %create colorbar
c.Label.Interpreter = 'latex'; %define latex as interpreter
    for colorbar label
set(get(c,'label'),'string','particle concentration $\left
    [\mathrm{cm^{-3}}\right]$'); %enter colorbar label
xlabel(data_comb{1,14}); %give x label
ylabel(data_comb{1,15}); %give y label
title({['Influence of',' ',data_comb{1,14},' and '] [
    data_comb{1,15},' on particle concentration']}); %give
    caption
dates=[data_comb{:,13}];

for k=1:num_mat
    name=[path{k,1},'\',dates,'_particleconc_',num2str(ps),
        'nm']; %define name for saved figure file
    print('-painters',name,'-depsc');
```

```
    print('-painters',name,'-dpng','-r600'); %print figure
        as .png
end
```

A.3 Complementary figures to chapter 2

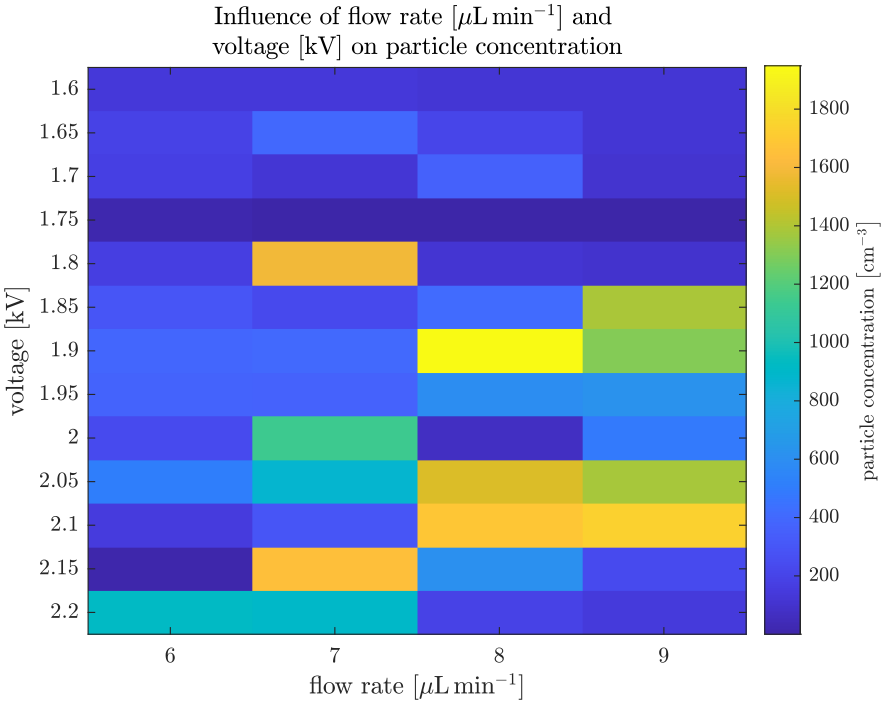

Figure A.1: Optimisation of EAG parameters for particles with a diameter of 20 nm. The particle concentration is plotted against the flow rate and the voltage.

A.4 Complementary figures to chapter 5

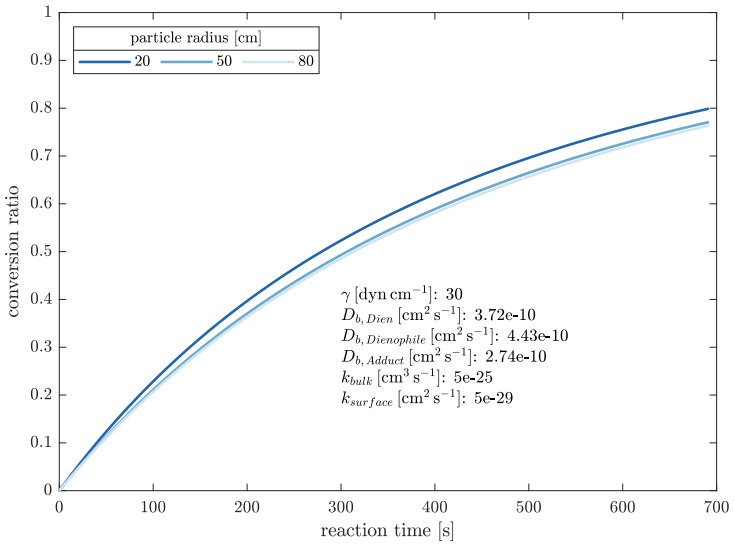

Figure A.2: Conversion ratios for particles with diameters from 20 nm to 80 nm. The inserted text displays the parameters used for the modelling run. γ denotes the surface tension, D_b the diffusion constants for the reactants and the Diels-Alder adduct and k the rate constants for the bulk and surface reaction.

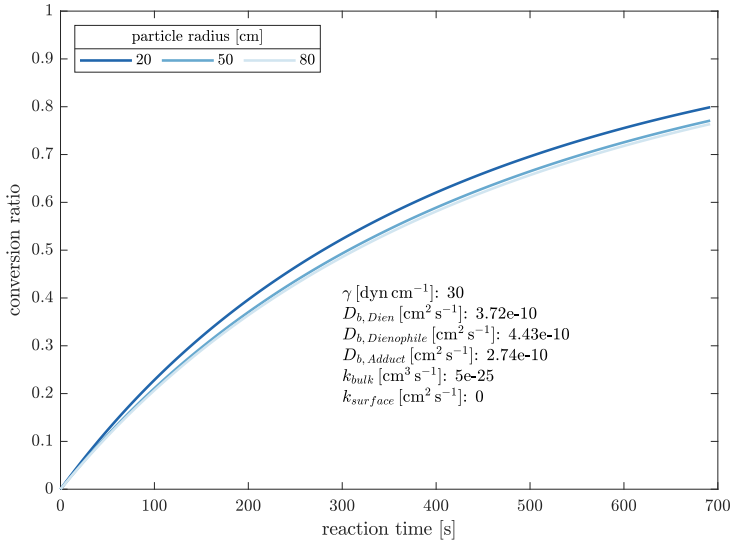

(a) Conversion ratio for different particle sizes.

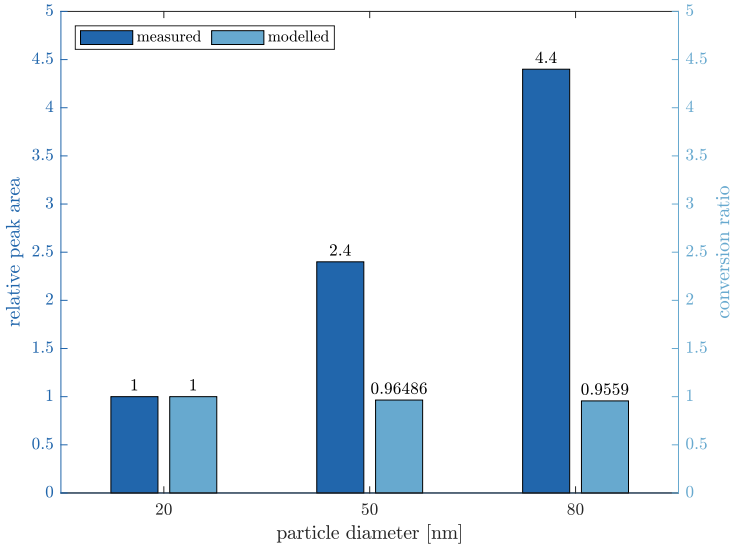

(b) Comparison of relative peak areas and conversion ratios.

Figure A.3: Comparison of relative peak areas and conversion ratios for the NanoChemistry model with $k_{surface} = 0$. (a) shows the conversion ratio as a function of time for three different particle sizes. The inserted text displays the surface tension γ, the diffusion constants D_b for the reactants and the product and the bulk and surface rate constants k. (b) shows the relative peak areas and conversion ratios.

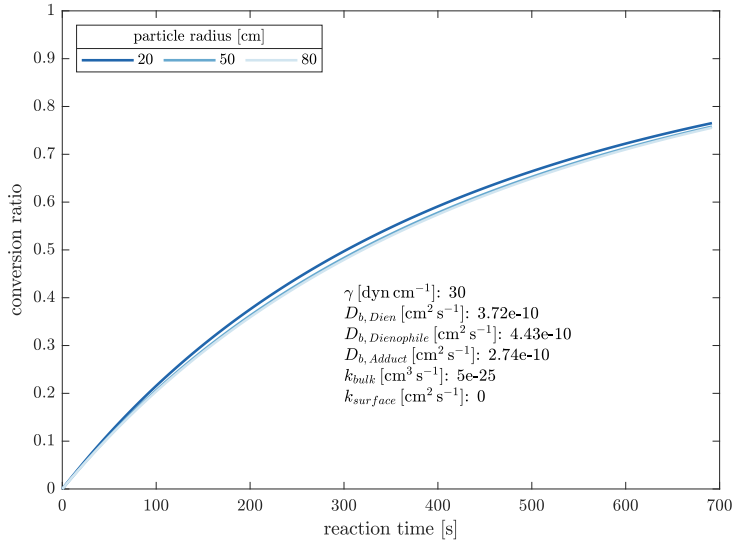

(a) Conversion ratio for different particle sizes.

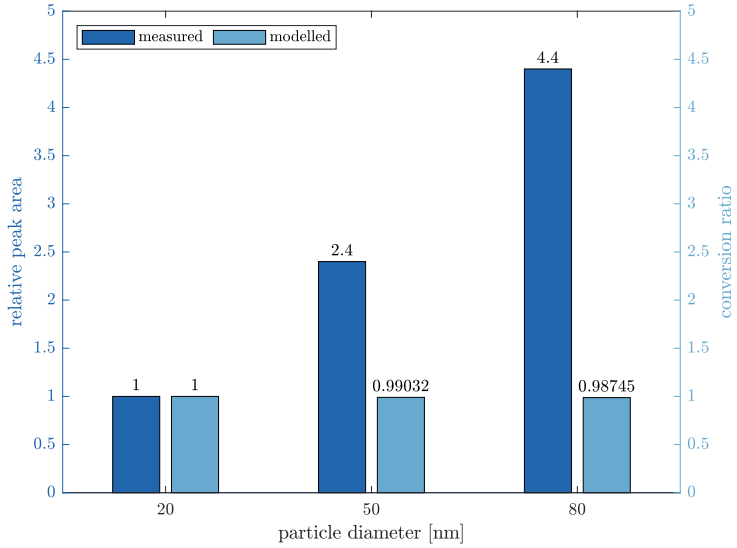

(b) Comparison of conversion ratios and relative peak areas.

Figure A.4: Comparison of relative peak areas and conversion ratios for the NanoChemistry model with $k_{surface} = 0$ and no diffusion between bulk and surface.(a) shows the conversion ratio as a function of time for three different particle sizes. The inserted text displays the surface tension γ, the diffusion constants D_b for the reactants and the product and the bulk and surface rate constants k. (b) shows the relative peak areas and conversion ratios for measured and modelled data.

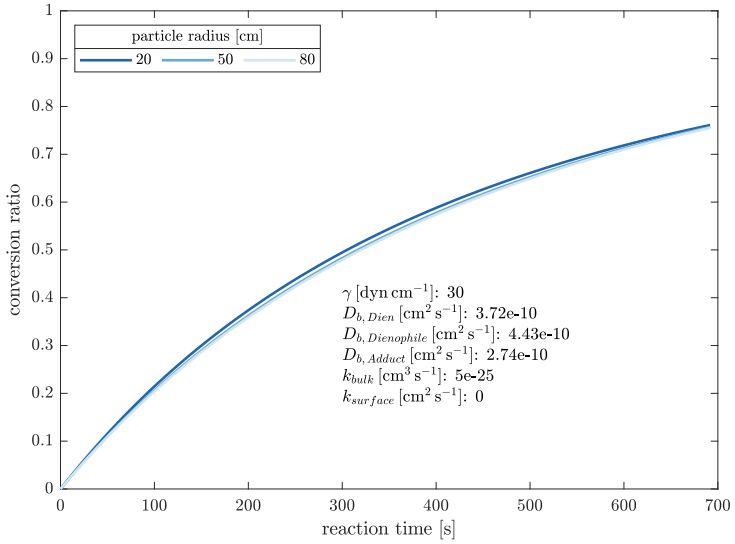

(a) Conversion ratio for different particle sizes.

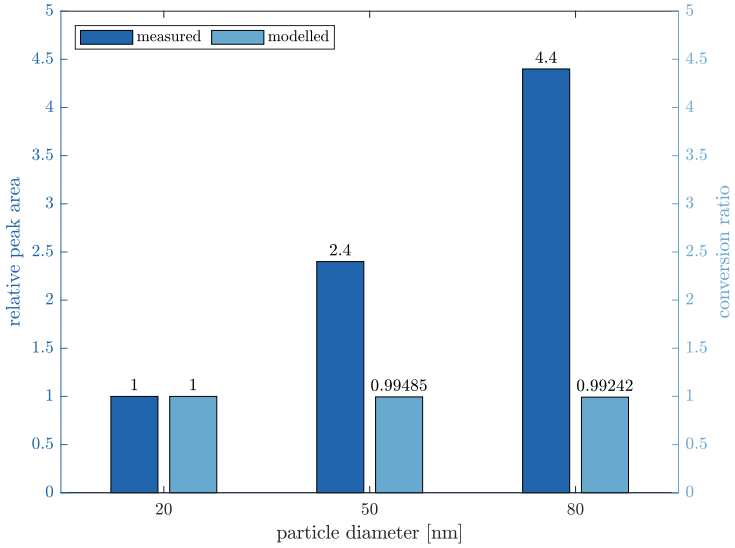

(b) Comparison of relative peak areas and conversion ratios.

Figure A.5: Comparison of relative peak areas and conversion ratios for the NanoChemistry model with $k_{surface} = 0$, surface layer thickness of 2 nm and no diffusion between bulk and surface.(a) shows the conversion ratio as a function of time for three different particle sizes. The inserted text displays the surface tension γ, the diffusion constants D_b for reactants ans product and the bulk and surface rate constants k. (b) shows the relative peak areas and conversion ratios for measured and modelled data.

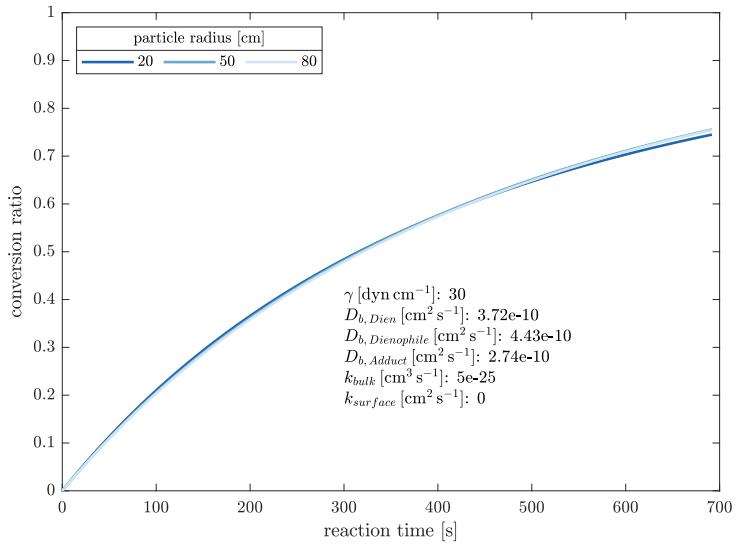

Figure A.6: Conversion ratios as a function of reaction time at a surface layer thickness of 5 nm. The inserted text displays the surface tension γ, the diffusion constants D_b for reactants and product and the bulk and surface rate constant k.

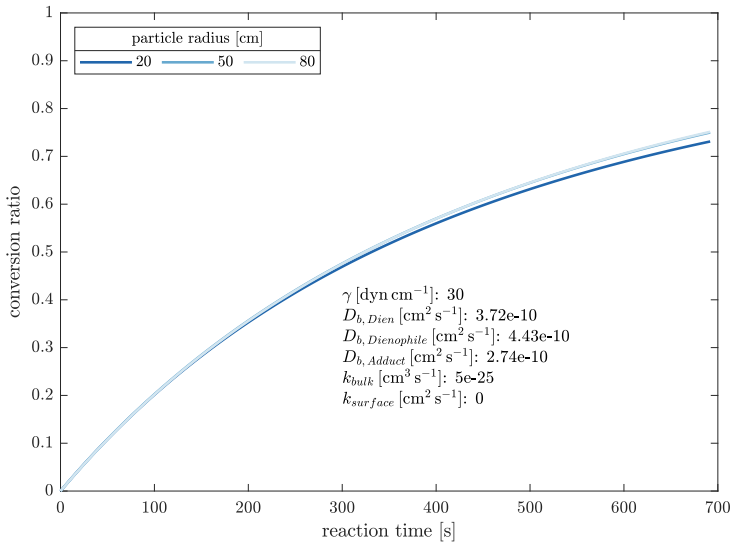

(a) Conversion ratio for different particle sizes.

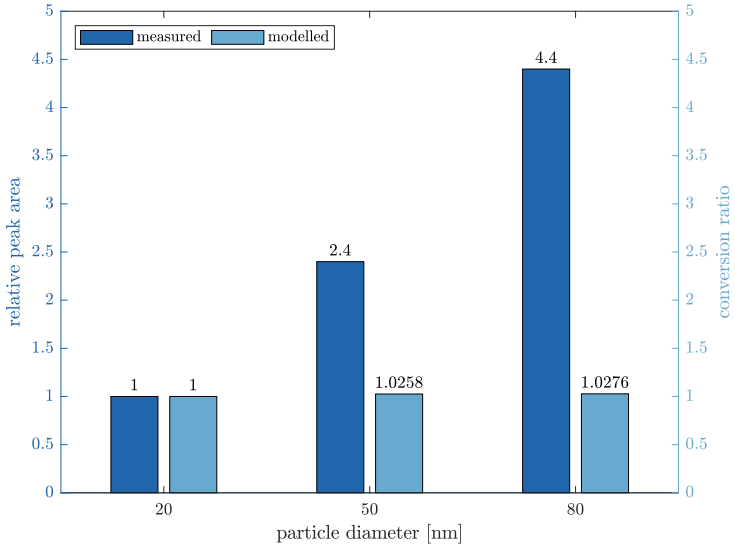

(b) Comparison of relative peak areas and conversion ratios.

Figure A.7: Comparison of relative peak areas and conversion ratios for the NanoChemistry model with $k_{surface} = 0$, surface layer thickness of 2 nm and no diffusion between bulk and surface. The activation volume has been increased to $-30 \times 10^{-6}\,\mathrm{m^3\,mol^{-1}}$. (a) shows the conversion ratio as a function of time for three different particle sizes. The inserted text display the surface tension γ, the diffusion constants D_b for the reactants and the product and the bulk and surface rate constants k. (b) shows the relative peak areas and conversion ratios for measured and modelled data.

List of Tables

List of Figures

Bibliography

Adams, P. J. 2002. Predicting global aerosol size distributions in general circulation models. *Journal of Geophysical Research: Atmospheres* 107 (D19). 10.1029/2001JD001010.

Adamson, A. W., and A. P. Gast. 1997. *Physical Chemistry of Surfaces.* 6. ed. A Wiley-Interscience publication. New York: Wiley. ISBN: 0471148733.

Andreae, M. O. 2013. Atmospheric Science. The Aerosol Nucleation Puzzle. *Science* 339 (6122): 911–912. 10.1126/science.1233798.

Asano, T., and W. J. Le Noble. 1978. Activation and Reaction Volumes in Solution. *Chemical Reviews* 78 (4): 407–489. 10.1021/cr60314a004.

Bain, R. M., C. J. Pulliam and G. R. Cooks. 2015. Accelerated Hantzsch electrospray synthesis with temporal control of reaction intermediates. *Chemical Science* 6 (1): 397–401. 10.1039/c4sc02436b.

Bain, R. M., C. J. Pulliam, F. Thery and G. R. Cooks. 2016. Accelerated Chemical Reactions and Organic Synthesis in Leidenfrost Droplets. *Angewandte Chemie International Edition in English* 55 (35): 10478–10482. 10.1002/anie.201605899.

Banerjee, S., E. Gnanamani, X. Yan and R. N. Zare. 2017. Can all bulk-phase reactions be accelerated in microdroplets? *The Analyst* 142 (9): 1399–1402. 10.1039/c6an02225a.

Baron, P. A., M. K. Mazumder, Y.-S. Cheng and T. M. Peters. 2011. Real-Time Techniques for Aerodynamic Size Measurement. In *Aerosol measurement: Principles, Techniques, and Applications,* 3. ed., edited by K. Willeke, P. A. Baron and P. Kulkarni, pp. 313–338. Aerosol measurement: Principles, Techniques, and Applications. Hoboken, N.J: Wiley. ISBN: 978-0-470-38741-2.

Becker, H. G. O. 2001. *Organikum: Organisch-chemisches Grundpraktikum.* 21., neu bearb. und erw. Aufl. Weinheim: Wiley-VCH. ISBN: 3-527-29985-8.

Benito-López, F., R. J. M. Egberink, D. N. Reinhoudt and W. Verboom. 2008. High pressure in organic chemistry on the way to miniaturization. *Tetrahedron* 64 (43): 10023–10040. 10.1016/j.tet.2008.07.108.

Blokhuis, E. M., and J. Kuipers. 2006. Thermodynamic expressions for the Tolman length. *Journal of Chemical Physics* 124 (7): 74701. 10.1063/1.2167642.

Böckmann, M. 2017. Chemie in Nanopartikeln: Untersuchungen zu druckabhängigen chemischen Reaktionen in Aerosoltropfen anhand von GC/MS- und HRMS-Messungen an organischen Modellsystemen. Institut für Anorganische und Analytische Chemie. Masterarbeit, Johannes Gutenberg-Universität Mainz.

Borukhova, S., A. D. Seeger, T. Noel, Q. Wang, M. Busch and V. Hessel. 2015. Pressure-Accelerated Azide-Alkyne Cycloaddition: Micro Capillary versus Autoclave Reactor Performance. *ChemSusChem* 8 (3): 504–512. 10.1002/cssc.201403034.

Brockmann, J. E. 2011. Aerosol Transport in Sampling Lines and Inlets. In *Aerosol measurement: Principles, Techniques, and Applications,* 3. ed., edited by K. Willeke, P. A. Baron and P. Kulkarni, pp. 69–105. Aerosol measurement: Principles, Techniques, and Applications. Hoboken, N.J: Wiley. ISBN: 978-0-470-38741-2.

Bruckner, R., and M. Harmata. 2010. *Organic Mechanisms.* 1. ed. Berlin and Heidelberg: Springer. ISBN: 978-3-642-03650-7.

Bruot, N., and F. Caupin. 2016. Curvature Dependence of the Liquid-Vapor Surface Tension beyond the Tolman Approximation. *Physical Review Letters* 116 (5): 1–5. 10.1103/PhysRevLett.116.056102.

Butt, H.-J., K. Graf and M. Kappl. 2003. *Physics and Chemistry of Interfaces.* 1. ed. Weinheim: Wiley-VCH Verlag GmbH & Co. KGaA. ISBN: 3-527-40413-9.

Cai, C., D. J. Stewart, J. P. Reid, Y.-H. Zhang, P. Ohm, C. S. Dutcher and S. L. Clegg. 2015. Organic Component Vapor Pressures and Hygroscopicities of Aqueous Aerosol Measured by Optical Tweezers. *The Journal of Physical Chemistry A* 119 (4): 704–718. 10.1021/jp510525r.

Cheng, Y., H. Su, T. Koop, E. Mikhailov and U. Pöschl. 2015. Size dependence of phase transitions in aerosol nanoparticles. *Nature Communications* 6 (1): 5923. 10.1038/ncomms6923.

Cheng, Y.-S. 2011. Condensation Particle Counters. In *Aerosol measurement: Principles, Techniques, and Applications,* 3. ed., edited by K. Willeke, P. A. Baron and P. Kulkarni, pp. 381–392. Aerosol measurement: Principles, Techniques, and Applications. Hoboken, N.J: Wiley. ISBN: 978-0-470-38741-2.

Clayden, J., N. Greeves and S. Warren. 2012. *Organic Chemistry.* 2. ed. Oxford: Oxford Univ. Press. ISBN: 9780199270293.

Curtius, J. 2006. Nucleation of atmospheric aerosol particles. *Comptes Rendus Physique* 7 (9-10): 1027–1045. 10.1016/j.crhy.2006.10.018.

Diels, O., and K. Alder. 1928. Synthesen in der hydroaromatischen Reihe: I. Mitteilung: Anlagerung von "Di-en"-kohlenwasserstoffen. *Justus Liebig's Annalen der Chemie* 460 (1): 98–122. 10.1002/jlac.19284600106.

Diels, O., and K. Alder. 1929a. Synthesen in der hydroaromatischen Reihe: III. Mitteilung: Synthese von Terpenen, Camphern, hydroaromatischen und heterocyclischen Systemen. *Justus Liebig's Annalen der Chemie* 470 (1): 62–103. 10.1002/jlac.19294700106.

Diels, O., and K. Alder. 1929b. Synthesen in der hydroaromatischen Reihe: IV. Mitteilung: Über die Anlagerung von Maleinsäure-anhydrid an arylierte Diene, Triene und Fulvene. *Berichte der Deutschen Chemischen Gesellschaft* 62 (8): 2081–2087. 10.1002/cber.19290620829.

Donahue, N. M., E. R. Trump, J. R. Pierce and I. Riipinen. 2011. Theoretical constraints on pure vapor-pressure driven condensation of organics to ultrafine particles. *Geophysical Research Letters* 38 (16). 10.1029/2011GL048115.

Dow, R. B., M. R. Fenske and H. E. Morgan. 1937. Effect of Pressure on Viscosity of Oils and Chlorinated Diphenyls. *Industrial & Engineering Chemistry* 29 (9): 1078–1080. 10.1021/ie50333a023.

Fang, X., Y. Li and X. Feng. 2017. Curvature effect on the surface topography evolution during oxidation at small scale. *Journal of Applied Physics* 121 (12): 125301. 10.1063/1.4978705.

Farkas, L. 1927. Keimbildungsgeschwindigkeit in übersättigten Dämpfen. *Zeitschrift für Physikalische Chemie* 125U (1): 236–242. 10.1515/zpch-1927-12513.

Farmer, D. K., and J. L. Jimenez. 2010. Real-time Atmospheric Chemistry Field Instrumentation. *Analytical Chemistry* 82 (19): 7879–7884. 10.1021/ac1010603.

Flagan, R. C. 2011. Electrical Mobility Methods for Submicrometer Particle Characterization. In *Aerosol measurement: Principles, Techniques, and Applications,* 3. ed., edited by K. Willeke, P. A. Baron and P. Kulkarni, pp. 339–364. Aerosol measurement: Principles, Techniques, and Applications. Hoboken, N.J: Wiley. ISBN: 978-0-470-38741-2.

Gennes, P.-G. de, F. Brochard-Wyart and D. Quéré. 2009. *Capillarity and Wetting Phenomena: Drops, Bubbles, Pearls, Waves.* New York, Berlin and Heidelberg: Springer. ISBN: 0387005927.

George, I. J., and J. P. D. Abbatt. 2010. Heterogeneous oxidation of atmospheric aerosol particles by gas-phase radicals. *Nature Chemistry* 2 (9): 713–722. 10.1038/nchem.806.

Gey, M. H. 2008. *Instrumentelle Analytik und Bioanalytik: Biosubstanzen, Trennmethoden, Strukturanalytik, Applikationen.* 2., überarb. und erw. Aufl. Berlin and Heidelberg: Springer. ISBN: 978-3-540-73804-6.

Giessen, A. E. van, and E. M. Blokhuis. 2009. Direct determination of the Tolman length from the bulk pressures of liquid drops via molecular dynamics simulations. *Journal of Chemical Physics* 131 (16): 164705. 10.1063/1.3253685.

Goldstein, A. H., and I. E. Galbally. 2007. Known and Unexplored Organic Constituents in the Earth's Atmosphere. *Environmental Science and Technology* 41 (5): 1514–1521. 10.1021/es072476p.

Gomes, A., E. Fernandes and J. L. F. C. Lima. 2005. Fluorescence probes used for detection of reactive oxygen species. *Journal of Biochemical and Biophysical Methods* 65 (2-3): 45–80. 10.1016/j.jbbm.2005.10.003.

Gordon, H., J. Kirkby, U. Baltensperger, F. Bianchi, M. Breitenlechner, J. Curtius, A. Dias et al. 2017. Causes and importance of new particle formation in the present-day and preindustrial atmospheres. *Journal of Geophysical Research: Atmospheres* 122 (16): 8739–8760. 10.1002/2017JD026844.

Griest, E. M., W. Webb and R. W. Schiessler. 1958. Effect of Pressure on Viscosity of Higher Hydrocarbons and Their Mixtures. *The Journal of Chemical Physics* 29 (4): 711–720. 10.1063/1.1744579.

Gross, J. H. 2013. *Massenspektrometrie: Ein Lehrbuch.* Berlin and Heidelberg: Springer. ISBN: 978-3-8274-2981-0.

Hallquist, M., J. C. Wenger, U. Baltensperger, Y. Rudich, D. Simpson, M. Claeys, J. Dommen et al. 2009. The formation, properties and impact of secondary organic aerosol: Current and emerging issues. *Atmospheric Chemistry and Physics* 9 (14): 5155–5236. 10.5194/acp-9-5155-2009.

Harris, D. C. 2014. *Lehrbuch der Quantitativen Analyse.* 8. Auflage. Berlin and Heidelberg: Springer Spektrum. ISBN: 978-3-642-37788-4.

Hesse, M., H. Meier and B. Zeeh. 2012. *Spektroskopische Methoden in der organischen Chemie.* 8., überarb. und erw. Aufl. In collaboration with S. Bienz, L. Bigler and T. Fox. Stuttgart: Thieme. ISBN: 978-3-13-576108-4.

Hinds, W. C. 1999. *Aerosol Technology: Properties, Behavior, and Measurement of Airborne Particles.* 2. ed. New York et al.: Wiley-Interscience. ISBN: 0-471-19410-7.

Hinds, W. C. 2011. Physical and Chemical Processes in Aerosol Systems. In *Aerosol measurement: Principles, Techniques, and Applications,* 3. ed., edited by K. Willeke, P. A. Baron and P. Kulkarni, pp. 31–40. Aerosol measurement: Principles, Techniques, and Applications. Hoboken, N.J: Wiley. ISBN: 978-0-470-38741-2.

Hoffmann, E. de, and V. Stroobant. 2011. *Mass Spectrometry: Principles and Applications.* 3. ed., reprinted. Chichester: Wiley. ISBN: 978-0-470-03310-4.

Hoffmann, T., R. Bandur, U. Marggraf and M. Linscheid. 1998. Molecular composition of organic aerosols formed in the α-pinene/O_3 reaction: Implications for new particle formation processes. *Journal of Geophysical Research: Atmospheres* 103 (D19): 25569–25578. 10.1029/98JD01816.

Hoffmann, T., R.-J. Huang and M. Kalberer. 2011. Atmospheric Analytical Chemistry. *Analytical Chemistry* 83 (12): 4649–4664. 10.1021/ac2010718.

Hoffmann, T., C. Zetzsch and M. J. Rossi. 2007. Chemie von Aerosolen. *Chemie in unserer Zeit* 41 (3): 232–246. 10.1002/ciuz.200700417.

Hou, I. C.-Y., Y. Hu, A. Narita and K. Müllen. 2018. Diels–Alder polymerization: a versatile synthetic method toward functional polyphenylenes, ladder polymers and graphene nanoribbons. *Polymer Journal* 50 (1): 3–20. 10.1038/pj.2017.69.

Hritz, A. D., T. M. Raymond and D. D. Dutcher. 2016. A method for the direct measurement of surface tension of collected atmospherically relevant aerosol particles using atomic force microscopy. *Atmospheric Chemistry and Physics* 16 (15): 9761–9769. 10.5194/acp-16-9761-2016.

Hu, Q., R. J. Noll, H. Li, A. Makarov, M. Hardman and G. R. Cooks. 2005. The Orbitrap: a new mass spectrometer. *Journal of Mass Spectrometry* 40 (4): 430–443. 10.1002/jms.856.

Intergovernmental Panel on Climate Change. 2013. *Climate Change 2013: The Physical Science Basis: Contribution of Working Group I to the Fifth Assessment Report of the Intergovernmental Panel on Climate Change.* Edited by T. F. Stocker, D. Qin, G.-K. Plattner, M. M. B. Tignor, S. K. Allen, J. Boschung, A. Nauels, Y. Xia, V. Bex and P. M. Midgley. Cambridge and New York: Cambridge Univ. Press. ISBN: 978-1-107-66182-0.

Intergovernmental Panel on Climate Change. 2014. *Climate Change 2014: Synthesis report: Contribution of Working Groups I,II and III to the Fifth Assessment Report of the Intergovernmental Panel on Climate Change.* Edited by Core Writing Team, R. K. Pachauri and L. A. Meyer. Geneva, Switzerland: IPCC. ISBN: 978-92-9169-143-2.

Intergovernmental Panel on Climate Change. 2021. *Climate Change 2021: The Physical Science Basis: Constributions from Working Group I to the Sixth Assessment Report of the Intergovernmental Panel On Climate Change.* Edited by V. Masson-Delmotte, P. Zhai, A. Pirani, S. L. Connors, C. Péan, S. Berger, N. Caud et al. Cambridge Univ. Press. Accessed 15 October 2021. https://www.ipcc.ch/report/ar6/wg1/#FullReport.

Jenner, G. 2002. High-pressure mechanistic delineation based on activation volumes. *Journal of Physical Organic Chemistry* 15 (1): 1–13. 10.1002/poc.458.

Jimenez, J. L., M. R. Canagaratna, N. M. Donahue, A. S. H. Prévôt, Q. Zhang, J. H. Kroll, P. F. DeCarlo et al. 2009. Evolution of Organic Aerosols in the Atmosphere. *Science* 326 (5959): 1525–1529. 10.1126/science.1180353.

John, W. 2011. Size Distribution Characteristics of Aerosols. In *Aerosol measurement: Principles, Techniques, and Applications,* 3. ed., edited by K. Willeke, P. A. Baron and P. Kulkarni, pp. 41–54. Aerosol measurement: Principles, Techniques, and Applications. Hoboken, N.J: Wiley. ISBN: 978-0-470-38741-2.

Johnston, M. V., and D. E. Kerecman. 2019. Molecular Characterization of Atmospheric Organic Aerosol by Mass Spectrometry. *Annual Review of Analytical Chemistry* 12 (1): 247–274. 10.1146/annurev-anchem-061516-045135.

Jurczak, J., and D. T. Gryko. 1997. Organic Synthesis at High Pressure. In *Chemistry Under Extreme and Non-Classical Conditions,* edited by R. van Eldik and C. D. Hubbard, pp. 163–188. New York: Wiley. ISBN: 978-0-471-16561-3.

Kesselmeier, J., and M. Staudt. 1999. Biogenic Volatile Organic Compounds (VOC): An Overview on Emission, Physiology and Ecology. *Journal of Atmospheric Chemistry* 33 (1): 23–88. 10.1023/A:1006127516791.

Kirkby, J., J. Duplissy, K. Sengupta, C. Frege, H. Gordon, C. Williamson, M. Heinritzi et al. 2016. Ion-induced nucleation of pure biogenic particles. *Nature* 533 (7604): 521–526. 10.1038/nature17953.

Klärner, F.-G., M. K. Diedrich and A. E. Wigger. 1997. Effect of Pressure on Organic Reactions. In *Chemistry Under Extreme and Non-Classical Conditions,* edited by R. van Eldik and C. D. Hubbard, pp. 103–161. New York: Wiley. ISBN: 978-0-471-16561-3.

Klärner, F.-G., and F. Wurche. 2000. The Effect of Pressure on Organic Reactions. *Journal für praktische Chemie* 342 (7): 609–636. 10.1002/1521-3897(200009)342:7<609::AID-PRAC609>3.0.CO;2-Z.

Kolb, C. E., and D. R. Worsnop. 2012. Chemistry and Composition of Atmospheric Aerosol Particles. *Annual Review of Physical Chemistry* 63:471–491. 10.1146/annurev-physchem-032511-143706.

Koop, T., J. Bookhold, M. Shiraiwa and U. Pöschl. 2011. Glass transition and phase state of organic compounds: dependency on molecular properties and implications for secondary organic aerosols in the atmosphere. *Physical chemistry chemical physics : PCCP* 13 (43): 19238–19255. 10.1039/c1cp22617g.

Kou, Xiaoshan, Weihai Ni, Chia-Kuang Tsung, Kong Chan, Hai-Qing Lin, Galen D. Stucky and Jianfang Wang. 2007. Growth of Gold Bipyramids with Improved Yield and Their Curvature-Directed Oxidation. *Small* 3 (12): 2103–2113. 10.1002/smll.200700379.

Kroll, J. H., C. Y. Lim, S. H. Kessler and K. R. Wilson. 2015. Heterogeneous Oxidation of Atmospheric Organic Aerosol: Kinetics of Changes to the Amount and Oxidation State of Particle-Phase Organic Carbon. *The Journal of Physical Chemistry A* 119 (44): 10767–10783. 10.1021/acs.jpca.5b06946.

Kroll, J. H., and J. H. Seinfeld. 2008. Chemistry of secondary organic aerosol: Formation and evolution of low-volatility organics in the atmosphere. *Atmospheric Environment* 42 (16): 3593–3624. 10.1016/j.atmosenv.2008.01.003.

Kückelmann, U., B. Warscheid and T. Hoffmann. 2000. On-Line Characterization of Organic Aerosols Formed from Biogenic Precursors Using Atmospheric Pressure Chemical Ionization Mass Spectrometry. *Analytical Chemistry* 72 (8): 1905–1912. 10.1021/ac991178a.

Kulkarni, P., and P. A. Baron. 2011. An Approach to Performing Aerosol Measurements. In *Aerosol measurement: Principles, Techniques, and Applications,* 3. ed., edited by K. Willeke, P. A. Baron and P. Kulkarni, pp. 55–65. Aerosol measurement: Principles, Techniques, and Applications. Hoboken, N.J: Wiley. ISBN: 978-0-470-38741-2.

Kulkarni, P., P. A. Baron and K. Willeke. 2011. Introduction to Aerosol Characterization. In *Aerosol measurement: Principles, Techniques, and Applications,* 3. ed., edited by K. Willeke, P. A. Baron and P. Kulkarni, pp. 3–13. Aerosol measurement: Principles, Techniques, and Applications. Hoboken, N.J: Wiley. ISBN: 978-0-470-38741-2.

Kulmala, M., T. Suni, K. E. J. Lehtinen, M. Dal Maso, M. Boy, A. Reissell, Ü. Rannik et al. 2004. A new feedback mechanism linking forests, aerosols, and climate. *Atmospheric Chemistry and Physics* 4 (2): 557–562. 10.5194/acp-4-557-2004.

Lala, D., J. F. Rabek and B. Ranby. 1980. The effect of 1,3-diphenylisobenzofuran on the photo-oxidative degradation of cis-1,4-polybutadiene. *European Polymer Journal* 16 (8): 735–744. 10.1016/0014-3057(80)90042-7.

Lanz, V. A., M. R. Alfarra, U. Baltensperger, B. Buchmann, C. Hueglin and A. S. H. Prévôt. 2007. Source apportionment of submicron organic aerosols at an urban site by factor analytical modelling of aerosol mass spectra. *Atmospheric Chemistry and Physics* 7 (6): 1503–1522. 10.5194/acp-7-1503-2007.

Li, Y., D. A. Day, H. Stark, J. L. Jimenez and M. Shiraiwa. 2020. Predictions of the glass transition temperature and viscosity of organic aerosols from volatility distributions. *Atmospheric Chemistry and Physics* 20 (13): 8103–8122. 10.5194/acp-20-8103-2020.

Lide, D. R., ed. 2005. *CRC Handbook of Chemistry and Physics.* 85th ed. Boca Raton: CRC Press. http://www.hbcpnetbase.com/.

Lopez-Hilfiker, F. D., C. Mohr, M. Ehn, F. Rubach, E. Kleist, J. Wildt, T. F. Mentel et al. 2014. A novel method for online analysis of gas and particle composition: description and evaluation of a Filter Inlet for Gases and AEROsols (FIGAERO). *Atmospheric Measurement Techniques* 7 (4): 983–1001. 10.5194/amt-7-983-2014.

Makarov, A. 2000. Electrostatic Axially Harmonic Orbital Trapping: A High-Performance Technique of Mass Analysis. *Analytical Chemistry* 72 (6): 1156–1162. 10.1021/ac991131p.

Makarov, A., E. Denisov, A. Kholomeev, W. Balschun, O. Lange, K. Strupat and S. Horning. 2006. Performance Evaluation of a Hybrid Linear Ion Trap/Orbitrap Mass Spectrometer. *Analytical Chemistry* 78 (7): 2113–2120. 10.1021/ac0518811.

McCabe, J. R., and C. A. Eckert. 1974. The Role of High-Pressure Kinetics in Studies of the Transition States of Diels-Alder Reactions. *Accounts of Chemical Research* 7 (8): 251–257. 10.1021/ar50080a003.

Müller, T., A. K. Badu-Tawiah and G. R. Cooks. 2012. Accelerated carbon-carbon bond-forming reactions in preparative electrospray. *Angewandte Chemie International Edition in English* 51 (47): 11832–11835. 10.1002/anie.201206632.

Petters, M., and S. Kasparoglu. 2020. Predicting the influence of particle size on the glass transition temperature and viscosity of secondary organic material. *Scientific reports* 10 (1): 15170. 10.1038/s41598-020-71490-0.

Pierce, J. R., I. Riipinen, M. Kulmala, M. Ehn, T. Petäjä, H. Junninen, D. R. Worsnop and N. M. Donahue. 2011. Quantification of the volatility of secondary organic compounds in ultrafine particles during nucleation events. *Atmospheric Chemistry and Physics* 11 (17): 9019–9036. 10.5194/acp-11-9019-2011.

Pöschl, U. 2005. Atmospheric Aerosols: Composition, Transformation, Climate and Health Effects. *Angewandte Chemie International Edition in English* 44 (46): 7520–7540. 10.1002/anie.200501122.

Prather, K. A., C. D. Hatch and V. H. Grassian. 2008. Analysis of Atmospheric Aerosols. *Annual Review of Analytical Chemistry* 1:485–514. 10.1146/annurev.anchem.1.031207.113030.

Pratt, K. A., and K. A. Prather. 2012a. Mass spectrometry of atmospheric aerosols – Recent developments and applications. Part I: Off-line mass spectrometry techniques. *Mass Spectrometry Reviews* 31 (1): 1–16. 10.1002/mas.20322.

Pratt, K. A., and K. A. Prather. 2012b. Mass spectrometry of atmospheric aerosols – Recent developments and applications. Part II: On-line mass spectrometry techniques. *Mass Spectrometry Reviews* 31 (1): 17–48. 10.1002/mas.20330.

Ramachandran, G., and D. W. Cooper. 2011. Size Distribution Data Analysis and Presentation. In *Aerosol measurement: Principles, Techniques, and Applications,* 3. ed., edited by K. Willeke, P. A. Baron and P. Kulkarni, pp. 479–506. Aerosol measurement: Principles, Techniques, and Applications. Hoboken, N.J: Wiley. ISBN: 978-0-470-38741-2.

Raynor, P. C., D. Leith, K. W. Lee and R. Mukund. 2011. Sampling and Analysis using Filters. In *Aerosol measurement: Principles, Techniques, and Applications,* 3. ed., edited by K. Willeke, P. A. Baron and P. Kulkarni, pp. 107–128. Aerosol measurement: Principles, Techniques, and Applications. Hoboken, N.J: Wiley. ISBN: 978-0-470-38741-2.

Reid, J. P., A. K. Bertram, D. O. Topping, A. Laskin, S. T. Martin, M. D. Petters, F. D. Pope and G. Rovelli. 2018. The viscosity of atmospherically relevant organic particles. *Nature Communications* 9 (1): 1–10. 10.1038/s41467-018-03027-z.

Rideout, D. C., and R. Breslow. 1980. Hydrophobic Acceleration of Diels-Alder Reactions. *Journal of the American Chemical Society* 102 (26): 7816–7817. 10.1021/ja00546a048.

Riipinen, I., J. R. Pierce, T. Yli-Juuti, T. Nieminen, S. Häkkinen, M. Ehn, H. Junninen et al. 2011. Organic condensation: a vital link connecting aerosol formation to cloud condensation nuclei (CCN) concentrations. *Atmospheric Chemistry and Physics* 11 (8): 3865–3878. 10.5194/acp-11-3865-2011.

Riipinen, I., T. Yli-Juuti, J. R. Pierce, T. Petäjä, D. R. Worsnop, M. Kulmala and N. M. Donahue. 2012. The contribution of organics to atmospheric nanoparticle growth. *Nature Geoscience* 5 (7): 453–458. 10.1038/ngeo1499.

Schmelzer, J. W. P., E. D. Zanotto and V. M. Fokin. 2005. Pressure dependence of viscosity. *The Journal of Chemical Physics* 122 (7): 07451101–07451111. 10.1063/1.1851510.

Schulz, H., V. Harder, A. Ibald-Mulli, A. Khandoga, W. Koenig, F. Krombach, R. Radykewicz, A. Stampfl, B. Thorand and A. Peters. 2005. Cardiovascular Effects of Fine and Ultrafine Particles. *Journal of Aerosol Medicine* 18 (1): 1–22. 10.1089/jam.2005.18.1.

Seinfeld, J. H., and S. N. Pandis. 2006. *Atmospheric Chemistry and Physics: From Air Pollution to Climate Change.* 2. ed. Hoboken, NJ: Wiley. ISBN: 978-0-471-72017-1.

Sellegri, K., and J. Boulon. 2016. Aerosol Nucleation in the Terrestrial Atmosphere. In *Atmospheric Aerosols: Life Cycles and Effects on Air Quality and Climate,* 1. ed., edited by C. Tomasi, A. A. Kokhanovsky and S. Fuzzi, pp. 87–114. Weinheim: Wiley-VCH. ISBN: 978-3-527-33643-2.

Shang, J., M. Passananti, Y. Dupart, R. Ciuraru, L. Tinel, S. Rossignol, S. Perrier, T. Zhu and C. George. 2016. SO_2 Uptake on Oleic Acid: A New Formation Pathway of Organosulfur Compounds in the Atmosphere. *Environmental Science and Technology Letters* 3 (2): 67–72. 10.1021/acs.estlett.6b00006.

Shiraiwa, M., Markus Ammann, Thomas Koop and Ulrich Pöschl. 2011. Gas uptake and chemical aging of semisolid organic aerosol particles. *Proceedings of the National Academy of Sciences of the United States of America* 108 (27): 11003–11008. 10.1073/pnas.1103045108.

Shiraiwa, M., C. Pfrang, T. Koop and U. Pöschl. 2012. Kinetic multi-layer model of gas-particle interactions in aerosols and clouds (KM-GAP): linking condensation, evaporation and chemical reactions of organics, oxidants and water. *Atmospheric Chemistry and Physics* 12 (5): 2777–2794. 10.5194/acp-12-2777-2012.

Shiraiwa, M., C. Pfrang and U. Pöschl. 2010. Kinetic multi-layer model of aerosol surface and bulk chemistry (KM-SUB): the influence of interfacial transport and bulk diffusion on the oxidation of oleic acid by ozone. *Atmospheric Chemistry and Physics* 10 (8): 3673–3691. 10.5194/acp-10-3673-2010.

Shrivastava, M., C. D. Cappa, J. Fan, A. H. Goldstein, A. B. Guenther, J. L. Jimenez, C. Kuang et al. 2017. Recent advances in understanding secondary organic aerosol: Implications for global climate forcing. *Reviews of Geophysics* 55 (2): 509–559. 10.1002/2016RG000540.

Skoog, D. A., D. M. West, F. J. Holler and S. R. Crouch. 2014. *Fundamentals of Analytical Chemistry.* 9. ed. Belmont, CA: Brooks/Cole, Cengage Learning. ISBN: 978-0-495-55828-6.

Sorensen, C. M., J. Gebhart, T. J. O'Hern and D. J. Rader. 2011. Optical Measurement Techniques: Fundamentals and Applications. In *Aerosol measurement: Principles, Techniques, and Applications,* 3. ed., edited by K. Willeke, P. A. Baron and P. Kulkarni, pp. 269–312. Aerosol measurement: Principles, Techniques, and Applications. Hoboken, N.J: Wiley. ISBN: 978-0-470-38741-2.

Tolman, R. C. 1949. The Effect of Droplet Size on Surface Tension. *Journal of Chemical Physics* 17 (3): 333–337. 10.1063/1.1747247.

Tomasi, C., and A. Lupi. 2016. Primary and Secondary Sources of Atmospheric Aerosols. In *Atmospheric Aerosols: Life Cycles and Effects on Air Quality and Climate,* 1. ed., edited by C. Tomasi, A. A. Kokhanovsky and S. Fuzzi, pp. 1–86. Weinheim: Wiley-VCH. ISBN: 978-3-527-33643-2.

TSI Incorporated. 2005. *Model 3076 Constant Output Atomizer: Instruction Manual.* TSI Incorporated, Shoreview, MN, USA.

TSI Incorporated. 2014. *Advanced Electrospray Aerosol Generator Model 3482: User's Manual.* TSI Incorporated, Shoreview, MN, USA.

TSI Incorporated. 2016. *Electrostatic Classifier Model 3082 Scanning Mobility Particle Sizer™ (SMPS™) Spectrometer Model 3939: Operation and Service Manual.* TSI Incorporated, Shoreview, MN, USA.

TSI Incorporated. 2019. *Water-Based Condensation Particle Counter Model 3789: Operational Manual.* TSI Incorporated, Shoreview, MN, USA.

Virtanen, A., J. Joutsensaari, T. Koop, J. Kannosto, P. Yli-Pirilä, J. Leskinen, J. M. Mäkelä et al. 2010. An amorphous solid state of biogenic secondary organic aerosol particles. *Nature* 467 (7317): 824–827. 10.1038/nature09455.

Virtanen, A., J. Kannosto, H. Kuuluvainen, A. Arffman, J. Joutsensaari, E. Saukko, L. Hao et al. 2011. Bounce behavior of freshly nucleated biogenic secondary organic aerosol particles. *Atmospheric Chemistry and Physics* 11 (16): 8759–8766. 10.5194/acp-11-8759-2011.

Volmer, M., and A. Weber. 1926. Keimbildung in übersättigten Gebilden. *Zeitschrift für Physikalische Chemie,* no. 119, 277–301. 10.1515/zpch-1926-11927.

Wang, Z. 2010. *Comprehensive Organic Name Reactions and Reagents.* Chichester: Wiley. ISBN: 0470638850.

Warscheid, B., and T. Hoffmann. 2001. Structural elucidation of monoterpene oxidation products by ion trap fragmentation using on-line atmospheric pressure chemical ionisation mass spectrometry in the negative ion mode. *Rapid Communications in Mass Spectrometry* 15 (23): 2259–2272. 10.1002/rcm.504.

Went, F. W. 1960. Blue Hazes in the Atmosphere. *Nature* 187 (4738): 641–643. 10.1038/187641a0.

Whitby, K. T. 1978. The Physical Characteristics of Sulfur Aerosols. *Atmospheric Environment* 12 (1-3): 135–159. 10.1016/0004-6981(78)90196-8.

Willeke, K., and K. T. Whitby. 1975. Atmospheric Aerosols: Size Distribution Interpretation. *Journal of the Air and Waste Management Association* 25 (5): 529–534. 10.1080/00022470.1975.10470110.

Wonham, J. 1967. Effect of Pressure on the Viscosity of Water. *Nature* 215 (5105): 1053–1054. 10.1038/2151053a0.

World Health Organization. 2006. Health risks of particulate matter from long-range transboundary air pollution. Edited by World Health Organization. World Health Organization. Accessed 15 July 2021. https://www.euro.who.int/___data/assets/pdf_file/0006/78657/E88189.pdf.

Wright, T. P., C. Song, S. Sears and M. D. Petters. 2016. Thermodynamic and kinetic behavior of glycerol aerosol. *Aerosol Science and Technology* 50 (12): 1385–1396. 10.1080/02786826.2016.1245405.

Zhang, Q., J. L. Jimenez, M. R. Canagaratna, J. D. Allan, H. Coe, I. M. Ulbrich, M. R. Alfarra et al. 2007. Ubiquity and dominance of oxygenated species in organic aerosols in anthropogenically-influenced Northern Hemisphere midlatitudes. *Geophysical Research Letters* 34 (13): 1–6. 10.1029/2007GL029979.

Zhang, X.-F., and X. Li. 2011. The photostability and fluorescence properties of diphenylisobenzofuran. *Journal of Luminescence* 131 (11): 2263–2266. 10.1016/j.jlumin.2011.05.048.

Zobrist, B., C. Marcolli, D. A. Pedernera and T. Koop. 2008. Do atmospheric aerosols form glasses? *Atmospheric Chemistry and Physics* 8 (17): 5221–5244. 10.5194/acp-8-5221-2008.

Zuth, C., A. L. Vogel, S. Ockenfeld, R. Huesmann and T. Hoffmann. 2018. Ultrahigh-Resolution Mass Spectrometry in Real Time: Atmospheric Pressure Chemical Ionization Orbitrap Mass Spectrometry of Atmospheric Organic Aerosol. *Analytical Chemistry* 90 (15): 8816–8823. 10.1021/acs.analchem.8b00671.

Curriculum vitae